

Microwave Imaging of High-Contrast Objects

Dissertation

zur Erlangung des akademischen Grades

**Doktoringenieur
(Dr.-Ing.)**

von Dipl.-Ing. Tobias Meyer

geb. am 6.10.1972 in Lauchhammer

genehmigt durch die Fakultät für Elektrotechnik und Informationstechnik

der Otto-von-Guericke Universität Magdeburg

Gutachter:

Prof. Dr.-Ing. H. Chaloupka

Prof. Dr. rer. nat. habil. P. Hauptmann

Dr. I. L. Morrow

Prof. Dr.-Ing. A. S. Omar

Promotionskolloquium am 10.2.05

Preface

This work was performed at the Chair of Microwave and Communication Engineering of the O.-v.-Guericke University of Magdeburg. I would like to thank Prof. Dr. A. Omar for drawing my attention to microwave engineering and the exciting field of inverse electromagnetic problems as well as giving me the possibility to carry out the research work and write this thesis with all the necessary support in every aspect.

Thanks to the reviewers Prof. Chaloupka, Prof. Hauptmann and Dr. Morrow for reviewing the somewhat lengthy thesis and their thoughtful comments.

I would like to thank Dr. A. Jöstingmeier for the numerous discussions leading to the major ideas presented in this work or solving one of the many little problems occurring during the work on a complex project like a microwave imaging system. The quality of the written thesis was also greatly enhanced by the suggestions of Dr. Jöstingmeier. I do thank Mr. Nick Spiliotis for the great contributions to the development of the software for the multi-port VNA and the help in taking measurements. I would like to thank all my colleagues at the Institute for Electronics, Signal Processing and Communications for their assistance.

Tobias Meyer

Abstract

This thesis describes a novel approach to microwave imaging. The proposed methods are based on the spectral representation of the object. Regularization schemes for the solution of electromagnetic inverse problems are addressed. An iterative algorithm for the solution of the nonlinear least-squares problem arising in iterative image reconstruction is developed. The application of this algorithm to one-dimensional and three-dimensional imaging of high-contrast lossy objects is examined. The properties of the imaging systems designed to implement the algorithms are verified by simulation and actual measurements. The algorithms proposed in this work are computationally more expensive but accuracy and stability are superior compared to other microwave imaging methods.

Zusammenfassung

Die vorliegende Dissertation beschreibt neuartige Verfahren zur Erzeugung tomografischer Bilder mittels Mikrowellen. Basis für diese Verfahren ist die spektrale Darstellung des Untersuchungsobjekts mittels orthogonaler Funktionen. Eine Methode zur regularisierten Lösung inverser elektromagnetischer Probleme wird vorgestellt und in die bekannten Standardverfahren eingeordnet. Das Untersuchungsobjekt wird in einem iterativen Verfahren aus den Messdaten berechnet. Ein speziell für diesen Anwendungsfall entwickelter Algorithmus zur effizienten Lösung des nicht-linearen Problems der kleinsten Fehlerquadrate wird vorgestellt. Der Nachweis der Funktionstüchtigkeit dieser Ansätze erfolgt mittels Simulations- und Messdaten von eindimensionalen Profilen und dreidimensionalen Untersuchungsobjekten mit starkem Kontrast. Ein komplettes und weitgehend automatisiertes Messsystem, welches nach den vorgeschlagenen Algorithmen arbeitet, wird detailliert beschrieben und die Testergebnisse werden vorgestellt. Das in dieser Arbeit entwickelte System erfordert im Vergleich zu anderen Verfahren einen höheren Rechenaufwand, kann aber Untersuchungsobjekte mit hohem Kontrast stabil und mit ausgezeichneter Abbildungsqualität rekonstruieren.

Contents

1	Introduction	7
1.1	Definition of Microwave Tomography	7
1.2	Electromagnetic Material Parameters	9
1.3	Motivation	11
1.4	Inverse Problems	13
1.5	Outline	15
2	State of the Art in Microwave Tomography and Imaging Methods	16
2.1	One-Dimensional Profile Inversion	16
2.2	Diffraction Tomography	19
2.3	Iterative Methods	23
2.4	Confocal Imaging	26
2.5	Conclusion	28
3	Regularization and Iterative Algorithm for Imaging of Strongly Scattering and Lossy Objects	29
3.1	Regularization	29
3.1.1	Iterative Regularization Methods	29
3.1.2	Regularization and Bandlimiting	32
3.1.3	Spectral Expansion of the Object Function	36
3.1.4	Formulation of the Smoothness Constraint	38
3.1.5	The Successively Relaxed Smoothness Constraint	40
3.2	Iterative Algorithm	42
3.2.1	Nonlinear Least-Squares	42
3.2.2	Hybrid Jacobian Approximation	44
3.2.3	Step Acceptance and Line Search	49
4	Reconstruction of Lossy One-Dimensional Permittivity Profiles	51
4.1	Imaging System Design	51
4.1.1	Measuring System	51
4.1.2	Design of Dielectrically Loaded Waveguide to Coax Transitions	53
4.1.3	Design of Dielectrically Loaded TRL Calibration Kits	55
4.2	Experimental Results	56
4.2.1	Noise Sensitivity	56
4.2.2	Feasibility of Tumor detection	61

4.2.3	Measuring Results	62
5	Three-Dimensional Microwave Resonator Tomography	66
5.1	Microwave Resonator Tomography System	66
5.1.1	System Concept	66
5.1.2	Resonator Design	67
5.1.3	Absorber Materials for Resonator Wall Coating	71
5.1.4	Automated Multi-Port S-Parameter Measurement System	76
5.1.5	Software Architecture	85
5.2	Imaging System Operation	87
5.2.1	System Calibration	87
5.2.2	Avoiding Undesired Constraints	88
5.2.3	Initial Guess	89
5.2.4	Imaging Process	89
5.3	Experimental Results	91
5.3.1	Sensitivity Distribution within the Cavity	91
5.3.2	Effect of measuring Frequency Range	91
5.3.3	Effect of cavity wall coating	93
5.3.4	FDTD model accuracy	93
5.3.5	Error functions	96
5.3.6	Imaging results	99
5.3.7	Measuring Results	102
6	Summary and Conclusion	104
A	Proof of the Tikhonov Reconstruction Formula	106
B	Calculation of the Gradient, Jacobian and Hessian for Nonlinear Least-Squares	108
C	Derivatives of a Series Expansion	110

List of Figures

1.1	Active microwave imaging system	8
1.2	Well-posed direct problem	14
1.3	Ill-posed inverse problem	14
2.1	One-dimensional profile inversion problem	17
2.2	Diffraction tomography measuring schemes: receiver line (left), circular receiver array (right)	20
2.3	Confocal microwave imaging system	27
3.1	Unregularized solution of a layered media problem.	30
3.2	Magnitude of input reflection (measured, simulated, start and reconstructed) for the layered media problem in figure 3.1.	30
3.3	TSVD and Tikhonov regularization image reconstruction example	33
3.4	Reconstructed objects from data with 80 dB SNR	35
3.5	Permittivity functions and corresponding magnitude of reflection	39
3.6	Number of required FDTD solver runs using the full finite difference Jacobian or the hybrid Jacobian approximation	48
4.1	Measuring set-up for the one-dimensional layered media reconstruction	52
4.2	Model and photo of the dielectrically loaded waveguide to coax transition	54
4.3	Simulated and measured input match for a dielectrically loaded waveguide to coax transition	54
4.4	Effect of the input data SNR on the reconstructed objects	58
4.5	Effect of input data noise level on calculated expansion coefficients	59
4.6	RMS permittivity error for different numbers of expansion coefficients and weighting functions	60
4.7	Weighting functions for expansion coefficients	60
4.8	Reconstruction results for different numbers of iterations	61
4.9	Images (real and imaginary part of the permittivity) of a tumor phantom embedded in fat tissue	62
4.10	Reconstruction of acrylic / air object	63
4.11	Reconstruction of an fat / air / PVC object	64
4.12	Comparison of simulated and measured reflection of a three layer object	65
5.1	Microwave Resonator Tomography System	67

5.2	Probe-coupled 3D imaging resonator and loop-coupled 2D imaging resonator prototypes	68
5.3	Distribution of field energy off-resonance (a) and at resonance (b)	69
5.4	S_{11} of a cavity with no wall coating (a) and with walls coated with a lossy dielectric (b)	70
5.5	Magnitude of the electric field distribution in a cavity with no wall coating (a) and with walls coated with a lossy dielectric (b)	70
5.6	Measured real and imaginary part of permittivity as function of added percentage of carbon modification.	73
5.7	Comparison of measured real and imaginary part of permittivity and 1st order Debye model.	75
5.8	Switch matrix layout	77
5.9	On- and off-state transmission of a switch (left), input match of a switch and accumulated input match of a switch with SMA termination at output (right)	78
5.10	Input match as seen by the DUT	79
5.11	S_{11} of a directional coupler measured with port combinations 1-2 and 1-3 before (left) and after (right) reference impedance transformation	80
5.12	Measured coupling of a 6 dB coupler before and after correction for imperfect terminations	82
5.13	Measured insertion loss of a 6 dB coupler before and after correction for imperfect terminations	83
5.14	Measured isolation of a 6 dB coupler before and after correction for imperfect terminations	84
5.15	Isolation of a coupler measured with the multi-port test set, a high precision load and a standard SMA load	84
5.16	Software architecture of the microwave resonator tomography imaging system	86
5.17	Comparison of measured and calculated reflection at port 4 and transmission between ports 1 and 4 of the unloaded cavity	87
5.18	Sensitivity distribution in the imaging resonator	92
5.19	Effect of measurement frequency range on 3D tomography	94
5.20	Permittivity error for different measuring frequency ranges and coefficient weighting filters	95
5.21	Effect of the material used for wall coating	95
5.22	Error functions of the nonlinear least squares problem	97
5.23	Residual error as a function of iteration	98
5.24	Imaging results of cross-sections of objects homogenous in the third dimension	99
5.25	3D image of a silicone rubber block	101
5.26	Imaging from measuring data	103

Constants

ε_0	permittivity of free space	8.854×10^{-12}	$\frac{\text{As}}{\text{Vm}}$
μ_0	permeability of free space	$4\pi \times 10^{-7}$	$\frac{\text{Vs}}{\text{Am}}$
c_0	speed of light in vacuum	$\frac{1}{\sqrt{\varepsilon_0\mu_0}}$	

Symbols

ε_r	relative permittivity		
μ_r	relative permeability		
σ	conductivity		$\frac{\text{A}}{\text{Vm}}$
E	electric field		$\frac{\text{V}}{\text{m}}$
H	magnetic field		$\frac{\text{A}}{\text{m}}$
D	electric flux density		$\frac{\text{As}}{\text{m}^2}$
B	magnetic flux density		$\frac{\text{Vs}}{\text{m}^2}$
P	electric polarization		$\frac{\text{As}}{\text{m}^2}$
M	magnetic polarization		$\frac{\text{A}}{\text{m}}$
Z	impedance		$\frac{\text{V}}{\text{A}}$
P	power		W
W_e	electric energy		Ws
W_m	magnetic energy		Ws
k_0	free space wavenumber		$\frac{\text{rad}}{\text{m}}$
ω	angular frequency		$\frac{\text{rad}}{\text{s}}$
$\tan \delta$	loss tangent, dissipation factor		
Q	quality factor		
Γ	reflection coefficient		
n	normal vector		
V	volume		m^3
S	surface		m^2
r	position vector		
n	index of refraction		
G	Green's function		
I	identity matrix		
F	residual function		
J	Jacobian matrix		

Chapter 1

Introduction

1.1 Definition of Microwave Tomography

Microwave imaging aims on the reconstruction of the material properties of an object by measuring the scattering of an electromagnetic signal it is illuminated with. The parameters to be imaged can be all properties that have an influence on the propagation of microwaves in the object. This can be dielectric constant, dielectric loss, conductivity, permeability and magnetic loss. The use of microwaves for the purpose of imaging allows nondestructive and non-contacting evaluation of materials and biological tissues. Possible applications are material testing, biomedical applications, environmental measurements and remote sensing.

Microwave imaging systems are usually active systems which means that the illumination signal is generated by the measuring system. Passive systems only receiving radiation from the object to be imaged are not widely used as there is only weak radiation in the microwave frequency range from most objects. An exception is passive millimeter-wave imaging that uses very short wave microwave radiation [1]. This part of the spectrum is neighboring the infrared region and works similar to infrared cameras. The frequencies used for active microwave imaging are ranging from below 1 GHz to 40 GHz, where most applications work in the range from 2 GHz to 8 GHz. This range is expected to give a good tradeoff between resolution and penetration. The aim for most microwave imaging systems is to image the distribution of the material parameters through the object, with emphasis on the non-accessible inner parts. This requires longer wavelengths due to their lower attenuation. Millimeter-wave imaging methods obtain very good resolution but lack tomographic abilities.

A typical active microwave imaging system is shown in figure 1.1. The transmitter generates a microwave signal and radiates it to generate the illuminating field. The illuminating field is scattered by the object. The scattered field is measured by the receiver. Multiple transmitters and receivers can be used or single transmitter or receiver configurations can illuminate the object and sample the scattered fields at multiple positions.

The illuminating field can be monochromatic or swept frequency when measuring in frequency domain. Narrow pulses are used in time domain measuring schemes

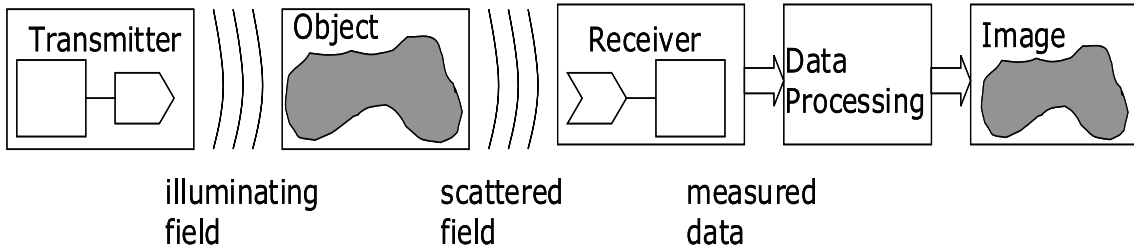


Figure 1.1: Active microwave imaging system

to achieve a large signal bandwidth which results in high resolution. Frequency domain measurements have the advantage that the measuring accuracy is usually better compared to time domain methods. A typical Vector Network Analyzer (VNA) used for frequency domain measurements has a dynamic range of 80 dB compared to only 40 dB for a standard Time Domain Reflectometer (TDR) [2],[3]. As measuring accuracy is a key element to good image quality most microwave imaging methods rely on frequency domain measurements. The measured data are then processed to form the image which is the distribution of the electromagnetic material parameters as a function of position in space.

The inner material parameter distribution of highly conductive objects is generally not accessible to microwave imaging. This is because of the strong attenuation of microwave signals in conductive media. The penetration depth is therefore very small and the measuring data contains no information about the sections not penetrated. There is another branch of microwave imaging which solves the problem of determining the shape and location of a non-penetrable, highly conducting object. This inverse obstacle problem [4] is not considered in this work.

The application of microwave imaging methods to three-dimensional objects is also often referred to as microwave tomography. This comes from the most used methods for three-dimensional imaging today computed X-ray tomography (CT) and magnetic resonance tomography (MRT). Because of the success of these, all methods which allow to visualize the inside of an object are entitled tomography. Tomography is a Greek word for ‘representing an object by slices’. CT and MRT actually obtain slices of the object and form a three-dimensional model by combining them. In microwave imaging the image acquisition is not carried out in terms of slices. The whole object must be imaged as a three-dimensional distribution because microwaves do not propagate like pencil beams as X-rays and therefore there is strong interaction in all dimensions which makes it impossible to separate the object into slices which can be imaged independently of each other. Although the term tomography is therefore incorrect in a strict sense it is still used for most microwave imaging methods allowing to acquire three-dimensional images by convention.

1.2 Electromagnetic Material Parameters

When using microwaves for imaging an object the distribution of the electromagnetic material parameters is reconstructed and used for the image formation. These are the permittivity ε , the permeability μ and the conductivity σ . The permittivity of a medium is defined by the total displacement current when an external field is applied. The total displacement current in the frequency domain consists of the vacuum displacement current

$$\mathbf{D}_0 = \varepsilon_0 \mathbf{E} \quad (1.1)$$

and the polarization current

$$\mathbf{P} = \varepsilon_0 \chi_e \mathbf{E}, \quad (1.2)$$

where the electric susceptibility χ_e is a dimensionless proportionality factor that accounts for the polarization current in multiples of the free-space displacement current for the same electric field strength. The polarization current can be caused by electronic polarization, ionic polarization and orientational polarization or any combination of these [5]. The total displacement current in a medium then becomes

$$\mathbf{D} = \varepsilon_0 \mathbf{E} + \mathbf{P} = \varepsilon_0(1 + \chi_e) \mathbf{E} = \varepsilon_0 \varepsilon_r \mathbf{E}, \quad (1.3)$$

where the relative permittivity ε_r is introduced to avoid accounting for the polarization separately. The relative permittivity of the medium is also called its relative dielectric constant. When dielectric loss is present in the medium the permittivity becomes a complex quantity with a negative imaginary part representing the dielectric loss [6].

$$\varepsilon = \varepsilon_0(\varepsilon_r' - j\varepsilon_r'') \quad (1.4)$$

Another quantity often used to describe dielectric loss is the dielectric loss tangent

$$\tan \delta_D = \frac{\varepsilon_r''}{\varepsilon_r'}. \quad (1.5)$$

The dielectric quality factor is defined by ratio of the average electric energy stored in a volume filled with the dielectric and the dissipated power due to dielectric loss in the same volume.

$$Q_D = \frac{2\omega \frac{dW_e}{dV}}{\frac{dP_{LD}}{dV}} = 2\omega \frac{\frac{1}{4}\varepsilon' E_0^2}{\frac{1}{2}\omega \varepsilon'' E_0^2} = \frac{1}{\tan \delta_D} \quad (1.6)$$

Here E_0 is the electric field magnitude. When the material is conductive the conductivity contributes to the losses also as can be seen from the magnetic field curl equation.

$$\nabla \times \mathbf{H} = j\omega \varepsilon_0(\varepsilon_r' - j\varepsilon_r'') \mathbf{E} + \sigma \mathbf{E} \quad (1.7)$$

For the case of both dielectric and conduction losses the loss tangent is given by

$$\tan \delta = \frac{\varepsilon_r'' + \frac{\sigma}{\omega \varepsilon_0}}{\varepsilon_r'}. \quad (1.8)$$

The effects of conduction loss and dielectric loss are indistinguishable at a single frequency and one can always be absorbed into the other. This leads to the concept of dielectric conductivity σ_D .

$$\sigma_D = \omega \varepsilon_0 \varepsilon_r'' \quad (1.9)$$

The magnetic polarization can be taken into account in a similar way. Using analogy between \mathbf{B} and \mathbf{D} the total magnetic flux density is given by

$$\mathbf{B} = \mu_0(\mathbf{H} + \mathbf{M}), \quad (1.10)$$

where $\mathbf{M} = \chi_m \mathbf{H}$ is the magnetic polarization, $\mu_0 \mathbf{M}$ is the magnetic moment per unit volume and χ_m is the magnetic susceptibility. This gives

$$\mathbf{B} = \mu_0 \mathbf{H} + \mu_0 \chi_m \mathbf{H} = \mu_0(1 + \chi_m) \mathbf{H} = \mu_0 \mu_r \mathbf{H}, \quad (1.11)$$

where the relative permeability

$$\mu_r = \mu_r' - j\mu_r'' \quad (1.12)$$

has been introduced. As in the electric case the relative permeability will become complex with negative imaginary part whenever the magnetic polarization is connected with damping forces causing losses.

As the inverse problem of calculating the image from the measuring data is very difficult to solve, such a high number of parameters would lead to increased ambiguity. Therefore a restriction to two important cases is usually made. The first case is the determination of the complex permittivity under the assumption of free space permeability $\mu = \mu_0$ and vanishing conductivity $\sigma = 0$. The assumption of free space permeability can be done with good accuracy as virtually all materials accessible with microwave imaging methods are either diamagnetic or paramagnetic and exhibit a relative permeability very close to unity. The second important case is the imaging of the real part of the permittivity $\varepsilon = \varepsilon_0 \varepsilon_r'$ and the conductivity $\sigma \neq 0$ with vanishing dielectric losses $\varepsilon_r'' = 0$ and free space permeability $\mu = \mu_0$. This means that a suitable model for the losses which can either be dielectric or resistive must be selected prior to the imaging process itself. Each of these material properties can be functions of three base vectors describing a three-dimensional space. As the electromagnetic properties of the object are imaged and the properties of the material surrounding the object are usually known, the shape of the object can also be determined.

The value of the relative permittivity is generally changing with frequency due to the different polarization mechanisms. For multi-frequency and time-domain microwave imaging methods this frequency dependence must be taken into account. A constant permittivity over the measuring frequency band is often assumed which can be done for many materials with good accuracy in the microwave frequency range. If the permittivity changes with frequency are non-negligible a suitable model fitting the expected frequency behavior must be selected which requires a-priori information. When using frequency domain solvers arbitrary permittivity frequency dependence can be modelled as this requires only multiplication with the value at the

current frequency according to equation (1.3). For the solution of a direct scattering problem in the time domain the electric flux density is given by the convolution of the impulse response of the permittivity $\varepsilon_r(\tau)$ and the electric field [7].

$$\mathbf{D}(t) = \varepsilon_0 \int_{\tau=0}^t \varepsilon_r(\tau) \mathbf{E}(t - \tau) d\tau \quad (1.13)$$

The repeated evaluation of this convolution integral can be a very time consuming task and therefore only a few models that allow easy evaluation of (1.13) are used. For an microwave imaging system employing time domain solvers this means that one is limited to certain dispersion characteristics that can be modelled. In addition this model must be selected a priori.

It is always assumed that the materials to be imaged are linear. The relations between electric field and total displacement as given by equations (1.3) and (1.11) can be expressed by multiplication with a constant independent of the electric or magnetic field amplitudes. Most materials can be modelled as being linear. Examples for exceptions are ferroelectric and ferrimagnetic materials. A third assumption to be made is that the materials are isotropic. From this follows that the displacement is directed along the field and the permittivity and permeability can be described by a scalar in contrast to a tensor formulation required for anisotropic media. This excludes anisotropic media such as ferrites which again is acceptable.

1.3 Motivation

Microwave imaging methods have attracted much attention since the first proposals for such systems in the late 1970's [8], [9]. Imaging methods using microwave signals are considered to have a high potential for providing a useful addition to established methods for medical imaging and nondestructive testing. The propagation of microwave signals in non-conducting materials allows to resolve two major problems associated with the currently used imaging methods. CT scans have the disadvantage that the absorption of X-Rays is similar for a large number of tissues. As the primary measuring data in a CT scan is the absorption of X-Rays along line integrals through the object, the resulting images of tissues having similar absorption have very little contrast. This low contrast is the reason that approximately 20 % of breast cancers are missed in X-ray mammography screening [10]. The advantage of using microwave radiation is that there are many soft tissues that show similar absorption of X-rays but show great contrast in the interaction with microwaves. By using microwave methods a high contrast is to be expected for images of such tissues problematic for X-ray imaging.

Microwave imaging systems work without possibly harmful ionizing radiation which is another major drawback of CT imaging. The danger of ionizing radiation has also been recognized by the public and led to a low acceptance of screenings using X-rays. Although the effects of electromagnetic radiation are also discussed because of the fast growing use of wireless communications, microwave imaging is safe. The microwave power level can be chosen very low and must only be sufficient

to allow for field measurements above the noise floor of the measuring system. As accurate measuring systems are readily available in form of automatic vector network analyzers (VNA) which are capable of performing accurate scattering parameter measurements at power levels measured in milliwatts the imaging process will not even lead to measurable heating of the imaged tissue. An exception to this is only the thermoacoustic CT [11] that uses high energy pulses from a radar transmitter for breast cancer detection.

MRT imaging offers high soft tissue contrast and is capable of delivering high-contrast and high-resolution images perfectly suited for many medical imaging applications. MRT images are generated based on physical parameters as relaxation times which are not tumor specific. This makes it for example difficult to distinguish between benign and malignant breast lesions based on MRT images [12]. This classification could be done using microwave radiation as malignant tissues are characterized by a much higher water content and the dielectric constant and the loss tangent are both much increased [10].

The major contribution to the cost of a microwave imaging system will be the VNA or the TDR instrument. The cost of a microwave imaging system would therefore be lower compared to CT systems and only a fraction of a very expensive (\$5,000,000) MRT system. This is another reason why microwave imaging systems would be perfectly suited for mass screening. It could provide a safe and low-cost imaging system.

Ultrasonic imaging is very well suited for many biomedical applications as it is non-ionizing and also lower cost compared to MRT. It has the disadvantage that the imaging results acquired are not reproducible in all cases and an experienced physician is needed to collect and evaluate the data [13]. Also the acoustic reflective data collected is sometimes not well correlated to the tissue imaged. There are attempts to improve ultrasonic imaging in order to gain quantitative information but the current state of the art systems do not yield this kind of information yet.

Microwave imaging methods also have the potential to provide quantitative information of the dielectric properties of the object. This quantitative information makes it possible to identify materials and tissues. If a known tissue is imaged the quantitative information can be used to determine its condition, which is mainly determined by its water content. This gives further possibilities in medical diagnostics [10] and non-destructive testing as well as in environmental applications [14], [15].

Despite of the possible advantages of microwave imaging no practically usable systems for three-dimensional microwave imaging are available today. There are several difficulties that have not been resolved yet. The propagation of microwave signals is very complex and is not as easy to model as the beam propagation of an X-ray along a straight line. The algorithm for obtaining the image from the measuring data is therefore more complicated. While fairly simple filtered backprojection algorithms based on the radon transform [16] can be applied on CT measuring data no such algorithms exist for microwave imaging systems. Microwave imaging methods can be derived by applying simple models and linearization algorithms comparable to those used in CT. Unfortunately these fail in practice as these models are not accurate enough. Most models are valid for the case of weakly scattering and low-loss

objects only. These limitations could be avoided by using full wave analysis instead of employing linearized models. The solution of three-dimensional scattering problems is possible today due to the increase in available computing power during the last two decades. While the solution of direct scattering problems has been possible at an acceptable computational cost for several years, microwave imaging using iterative schemes requires the repeated solution of the scattering problem which did lead to unacceptable computing time in the past. Only recently efficient finite difference time domain (FDTD) software in conjunction with high-performance low-cost computers is available that allows the application of iterative schemes. Due to these advances iterative schemes applying full wave analysis can be used and achieve acceptable computing time. Iterative schemes using simple models in the solution of the direct problems are still computationally much cheaper but must accept strong limitations in their applicability due to the limited validity of the underlying models.

1.4 Inverse Problems

Many of the difficulties in solving microwave imaging problems arise because retrieving the object that cause the measured fields is an electromagnetic inverse problem. The problem of finding the object corresponding to a set of measured scattering parameters or field strengths can be formulated as follows: Consider two Euclidian spaces \mathcal{X} and \mathcal{Y} . The mapping of elements of \mathcal{X} into elements of \mathcal{Y} is performed by an operator A . The subset in \mathcal{X} which contains possible arguments to the operator is its domain $\mathcal{D}(A)$. The subset in \mathcal{Y} which contains the mappings of the elements of the domain is the range of the operator $\mathcal{R}(A)$. If f is an element of \mathcal{X} and g is its mapping into \mathcal{Y} then the direct problem can be written as

$$Af = g. \tag{1.14}$$

This mapping is shown in figure 1.2 and is a well-posed problem under the following conditions.

1. The mapping depends continuously on the data.
2. The mapping is unique.
3. There exists a mapping for arbitrary input data.

These conditions were formulated in [17] and are widely used for the definition of well-posedness and ill-posedness [18], [19] and [20]. In an electromagnetic direct scattering problem the operator A describes the creation of scattered fields and corresponding measured field samples or scattering parameters by the object. It is called the direct one because it is directed along a cause-effect line, while the decision which operator is direct and which is inverse seems arbitrary from the mathematical point of view. The task in microwave imaging is now to find the object f that caused the measured set of field samples g which is clearly directed opposite the cause-effect line.

$$A^{-1}g = f. \tag{1.15}$$

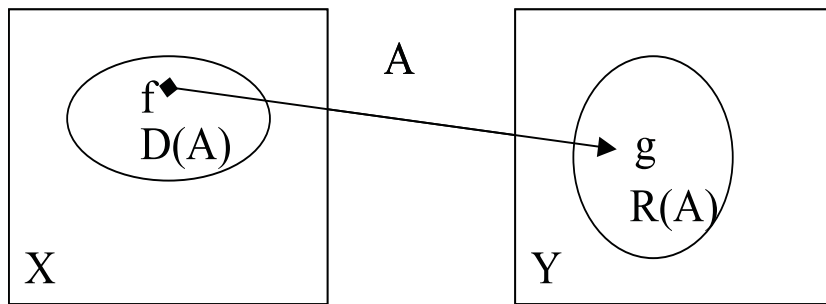


Figure 1.2: Well-posed direct problem

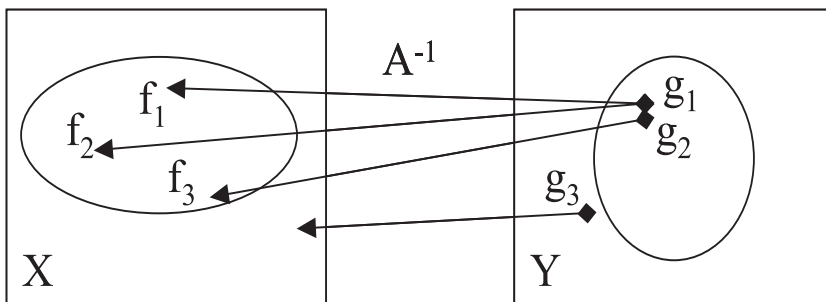


Figure 1.3: Ill-posed inverse problem

The solution of (1.15) involves finding the inverse operator A^{-1} . This inverse operator is usually not known and even if it was known its application to the set of measured samples would hardly give the object f . This is because the inverse operator does not fulfil the above conditions for well-posedness. The first problem is that the objects found by using the inverse operator do not depend continuously on the data. This undesired property of the inverse operator is shown in figure 1.3. Small measurement errors which are unavoidable in any practical set-up will cause large deviations in the object found. If an object f_1 created the field g_1 and this field is measured adding a small error resulting in an image g_2 , the solution of the inverse problem with that measured field as input data will lead to the entirely different object f_3 . The second problem is connected to non-uniqueness. As there are many objects creating the same fields the solution found is only one of the possible even with perfectly noiseless input data as the solutions f_1 and f_2 in figure 1.3 for the image g_1 . There might also be measured fields which do not have a solution at all as g_3 in figure 1.3 because they are outside the range of the operator due to the measurement noise.

The only way to cure ill-posedness is the use of additional information to minimize the number of possible solutions of (1.15). This is known as regularization and covered in detail in section 3.1. The additional information needed must be incorporated into the imaging algorithm and must therefore be known a-priori.

1.5 Outline

This work deals with the imaging of objects for medical imaging and nondestructive testing purposes. After a review of the current state of the art a novel object representation suitable for three-dimensional microwave imaging will be introduced. Based on that object representation a novel regularization scheme and a suitable iterative algorithm will be developed. The following chapters show the application of these concepts to one-dimensional and fully three-dimensional microwave imaging problems. The performance of the new algorithms is assessed by simulation and measurements. The design of suitable devices and systems needed for these imaging applications is described. These include dielectrically loaded waveguide to coax adaptors, calibration kits, multi-port resonators for three-dimensional microwave imaging and a multi-port vector network analyzer with novel optimized two-tier error correction.

Chapter 2

State of the Art in Microwave Tomography and Imaging Methods

2.1 One-Dimensional Profile Inversion

In one-dimensional profile reconstruction methods it is assumed that the material properties vary along the direction of the propagation only. An illuminating wave is created by the imaging system and because of the transverse homogeneity a reflected wave will be created by the object travelling in the opposed direction. This profile inversion is the first electromagnetic inverse problem investigated and is the basis for many concepts also found in algorithms for two- and three-dimensional imaging. Such a profile reconstruction problem is shown in figure 2.1. The input reflection coefficient Γ_{in} is measured at the starting point of the region of unknown permittivity $x = 0$ over some frequency band. The material parameters are considered to vary along x only and to be constant in the transverse plane.

The relation between the reflection coefficient and the permittivity profile is given by the nonlinear Ricatti differential equation [20].

$$\frac{d\Gamma(x)}{dx} = 2j\sqrt{\varepsilon_r(x)}k_0\Gamma(x) + (1 - \Gamma(x)^2) \frac{1}{4\varepsilon_r(x)} \frac{d\varepsilon_r(x)}{dx} \quad (2.1)$$

There is no known analytic solution to this equation, but it can be linearized by dropping the quadratic term in the reflection coefficient Γ .

$$\frac{d\Gamma(x)}{dx} = 2j\sqrt{\varepsilon_r(x)}k_0\Gamma(x) + \frac{1}{4\varepsilon_r(x)} \frac{d\varepsilon_r(x)}{dx} \quad (2.2)$$

The solution of this linearized differential equation is

$$\Gamma_{in}(k_0) = - \int_{x=0}^{\infty} \frac{1}{4\varepsilon_r(x)} \frac{d\varepsilon_r(x)}{dx} e^{-2j\sqrt{\varepsilon_r(x)}k_0x} dx. \quad (2.3)$$

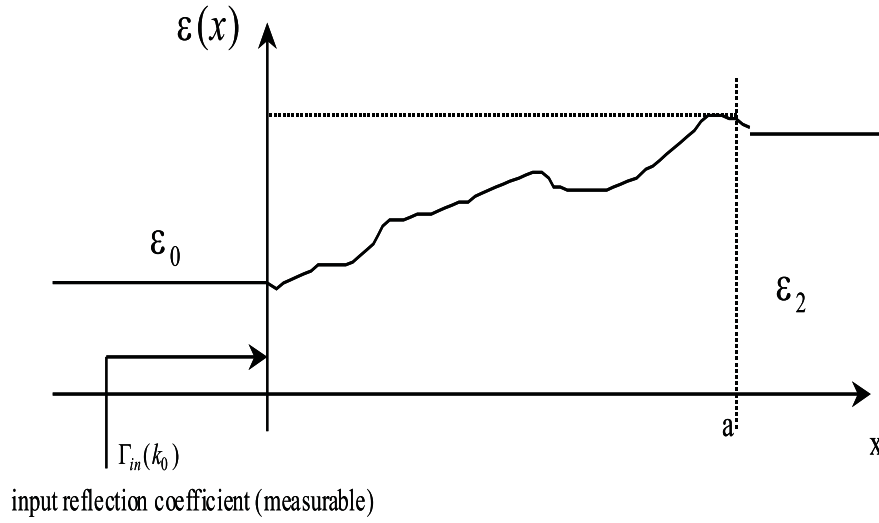


Figure 2.1: One-dimensional profile inversion problem

Here $\Gamma_{in}(k_0)$ is the measured input reflection coefficient as a function of wavenumber. Using a variable substitution introducing a virtual time variable t

$$t = 2 \int_{x'=0}^x \sqrt{\varepsilon_r(x')} dx' \quad (2.4)$$

and

$$dt = 2\sqrt{\varepsilon_r(x)} dx, \quad (2.5)$$

equation (2.3) can be interpreted as a Fourier transform of the permittivity profile from the virtual time domain to the wavenumber domain. It can be inverted to obtain the permittivity profile in terms of the measured reflection coefficient as a function of frequency [21].

$$-\frac{1}{8\varepsilon_r(x)\sqrt{\varepsilon_r(x)}} \frac{d\varepsilon_r(x)}{dx} = \int_{-\infty}^{\infty} \Gamma_{in}(k_0) e^{jk_0 t} dk_0 = \tilde{\Gamma}(t) \quad (2.6)$$

Here $\tilde{\Gamma}(t)$ is the inverse Fourier transform of the measured reflection coefficient. Multiplication of (2.6) with (2.5) and integrating yields

$$-\frac{1}{4} \ln \varepsilon_r(x) = \int_0^t \tilde{\Gamma}(t) dt. \quad (2.7)$$

Using the boundary condition at $x = 0$ to calculate the integration constant to $\varepsilon_r(0)$ this finally gives the looked for permittivity profile in terms of the inverse Fourier transform of the measured data and the permittivity value at the surface.

$$\varepsilon_r(x) = \varepsilon_r(0) e^{-4 \int_0^t \tilde{\Gamma}(t) dt} \quad (2.8)$$

Equation (2.8) allows the inversion of measured data for the permittivity profile. This inversion is unique and avoids the problem usually connected with the solution

of inverse problems. Unfortunately it has been obtained by dropping the nonlinear term which is only possible conserving accuracy when the reflection coefficient is small ($\Gamma^2 \ll 1$), which is just the application of the theory of small reflections [6]. This is only valid for weak scattering and virtually lossless objects as this is also based on the assumption that the incident wave is not attenuated as it propagates through the profile section. The permittivity profile is reconstructed in terms of the value at $x = 0$. If this is unknown it can be determined using the method described in [22]. The approach outlined above is used in [23] for permittivity profiles and in [24] for permittivity or pure conductivity profiles. The results of these works are only exact near the surface of the object to image. The case of profiles having both permittivity and conductivity variation which is encountered most often in practice is not treated. Later in [25] and [26] the method was improved and simplified by developing a microwave network technique to solve the inverse profile problem. Good accuracy for pure permittivity profiles is obtained for analytic profile inversions and numerical simulations, but no measuring examples of materials are given. The application for the reconstruction of pure weakly conductive media has been presented in [27]. The accuracy is again declining with rising penetration depth even for very weak conducting cases and simulated noiseless input data.

The accuracy of the profile reconstruction has been improved by introducing a nonlinear renormalization of the reflection coefficient which extends the applicability of the method to stronger scatterers [28]. This renormalization approach first renormalizes the measured reflection coefficient using a nonlinear renormalization function in order to minimize the error introduced by the linearization. The renormalization originally proposed in [29] is

$$\hat{\Gamma} = \operatorname{arctanh}\Gamma = \Gamma + \frac{\Gamma^3}{3} + \frac{\Gamma^5}{5} \dots, \quad (2.9)$$

where Γ is the reflection data measured and $\hat{\Gamma}$ is the renormalized reflection data. When this renormalized reflection data is used in (2.2), the derivative under the condition $|\Gamma| < 1$ which is always true for permittivity profiles gives

$$\frac{d\hat{\Gamma}}{dx} = \frac{1}{1 - \Gamma^2} \frac{d\Gamma}{dx}. \quad (2.10)$$

The series expansion of equation (2.9) and the derivative in equation (2.10) can now be inserted into the linearized Ricatti equation (2.2) which yields

$$\frac{d\Gamma}{dx} = 2j\sqrt{\varepsilon_r(x)}k_0 \left(\Gamma + \frac{\Gamma^3}{3} + \frac{\Gamma^5}{5} \dots \right) (1 - \Gamma^2) + (1 - \Gamma^2) \frac{1}{4\varepsilon_r(x)} \frac{d\varepsilon_r(x)}{dx} \quad (2.11)$$

The second term on the right hand side of (2.1) has been restored exactly using the nonlinear renormalization (2.9) in (2.2). The first error term is proportionate to Γ^3 as can be seen from the series expansion. Compared to dropping a term quadratic in Γ as in the simple linearization this leads to a much smaller error. The advantage is evident when the above method is applied to profiles having a stronger contrast and the assumption $\Gamma^2 \ll 1$ is not accurate. The nonlinear renormalization approach has

been further improved in [30] by using linear combinations of two renormalization functions. The improved method is also applicable to other coordinate systems [31] but still fails when applied to lossy objects.

Time domain methods for the one-dimensional profile reconstruction have also been studied [24], but the performance is always inferior to frequency domain techniques.

The solution of (2.1) is a simple integration along the profile from the starting plane where the reflection coefficient is measured to the end of the profile. This can computationally be treated effectively as the direct problem solution does not require full-wave analysis but only the integration of the nonlinear Riccati differential equation along the object. This fact allows fast treatment of this problem using iterative schemes. However, the straightforward application of a nonlinear optimization routine to calculate the function $\varepsilon_r(x)$ by matching the measured reflection data $\Gamma_{in}(k_0)$ will fail due to the nature of this inverse problem as will be discussed in section 3.1. The use of iterative methods for the one-dimensional profile inversion is proposed in [32], where stability is achieved by linearizing (2.1) around a permittivity profile known a-priori. Good accuracy is demonstrated for numerical examples. The drawback of this approach is the large amount of a-priori knowledge about the object required, as accuracy and stability entirely depend on a good initial guess.

2.2 Diffraction Tomography

Diffraction tomography was the first method proposed to use microwave scattering data for obtaining cross-sectional images of three-dimensional objects [33], [9]. It is based on the idea of adopting the same principles successful in the computed X-ray tomography (CT) which are the radon transform [16] and the Fourier slice theorem [34] for a system using microwave radiation instead of X-rays. By applying approximations which are mainly the Born or the Rytov approximations [35] an algorithm can be developed which replaces the Fourier slice theorem. The result is the Fourier diffraction theorem [36] which is taking into account the different propagation of microwaves in the object which is characterized by scattering effects. A typical diffraction tomography set-up is shown in figure 2.2. The object is illuminated using a plane wave and the scattered field is recorded at M receiver positions along a line behind the object. This measurement is repeated using L illumination angles Θ_l . A circular antenna array is used in the circular setup to synthesize a plane wave in the object domain. This avoids the need for mechanical rotation while the imaging algorithm remains unchanged.

Algorithms for diffraction tomography depend on the solution of the wave equation. The wave equation must be linearized and inverted in order to reconstruct the object. The approximations needed for the linearization limit the applicability of the diffraction tomography. All of these assume that the scattering is weak and the signal is not attenuated considerably as it propagates through the object. The most used approximation is the Born approximation. The object is illuminated with a

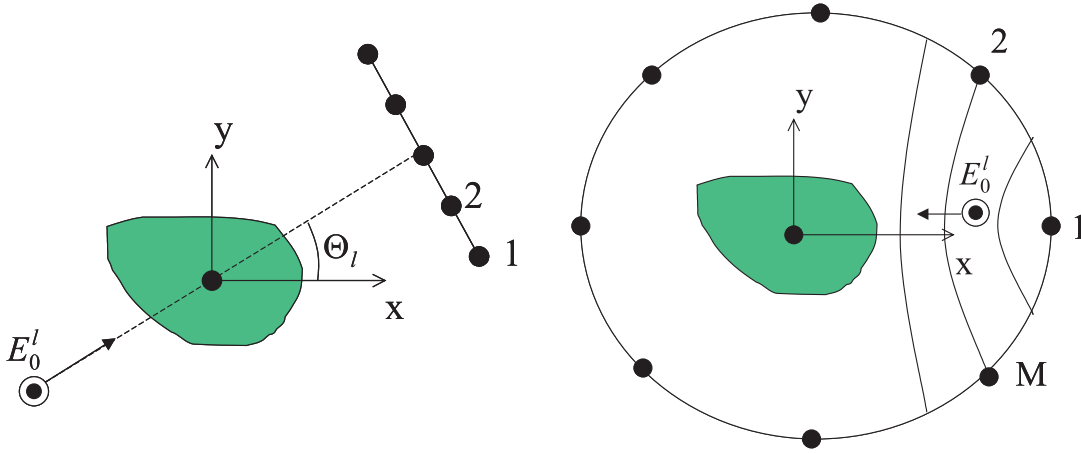


Figure 2.2: Diffraction tomography measuring schemes: receiver line (left), circular receiver array (right)

source field $\mathbf{E}_0(\mathbf{r})$ that fulfils the homogenous Helmholtz equation.

$$\nabla^2 \mathbf{E}_0(\mathbf{r}) + k_0^2 \mathbf{E}_0(\mathbf{r}) = 0 \quad (2.12)$$

Here $k_0 = \frac{2\pi}{\lambda}$ is the free space wavenumber. Free space is considered to be the background medium. The total field \mathbf{E}_t is the superposition of the incident field \mathbf{E}_0 and the scattered field \mathbf{E}_s .

$$\mathbf{E}_t(\mathbf{r}) = \mathbf{E}_0(\mathbf{r}) + \mathbf{E}_s(\mathbf{r}) \quad (2.13)$$

This total field is a solution of the wave equation in inhomogeneous media.

$$(\nabla^2 + k(\mathbf{r})^2) \mathbf{E}_t(\mathbf{r}) = 0, \quad (2.14)$$

where $k(\mathbf{r}) = k_0 n(\mathbf{r})$ is the local wavenumber and $n = \sqrt{\varepsilon_r}$ is the index of refraction of the object. The background as well as the object are considered to be virtually lossless. The index of refraction is therefore a real quantity. Inserting (2.13) in (2.14) and comparing with (2.12) shows that the scattered field is the solution of the inhomogeneous Helmholtz equation.

$$(\nabla^2 + k_0^2) \mathbf{E}_s(\mathbf{r}) = -O(\mathbf{r}) \mathbf{E}_t(\mathbf{r}) \quad (2.15)$$

Here $O = k_0^2 (n(\mathbf{r})^2 - 1)$ is the object function. The concept of object function is based on the idea of replacing the object by its equivalent free-space current. Equivalent free-space currents were originally used to calculate the effect of electromagnetic radiation on biological tissues [37]. The source term of (2.15) is the change in wavenumber caused by the object with respect to the background medium, which reflects the fact that the scattered field is caused by the object. Equation (2.15) can be solved for the scattered field using Green's function.

$$G(\mathbf{r}, \mathbf{r}_0) = \frac{e^{-jk_0 R}}{4\pi R}, \quad (2.16)$$

where $R = |\mathbf{r} - \mathbf{r}_0|$ is the distance from the source point \mathbf{r}_0 to the observation point \mathbf{r} . The scattered field caused by the object may now be expressed as the integration over all source points.

$$\mathbf{E}_s(\mathbf{r}) = \int G(\mathbf{r} - \mathbf{r}_0)O(\mathbf{r})\mathbf{E}_t(\mathbf{r}_0)d\mathbf{r}_0 \quad (2.17)$$

The calculation of the scattered field using scalar Green's functions is possible because the receiver array is located in the same plane as the cross section imaged and the object is assumed to be homogenous in the third dimension. The scattered fields caused by the object have a component in the direction of the incident field only and all fields can be expressed by scalars. Equation (2.17) can generally not be solved for the object function as the scattered field contributes to the total field on the right hand side of (2.17). The Born approximation replaces the total field as given in equation (2.13) by

$$\mathbf{E}_t(\mathbf{r}) \approx \mathbf{E}_0(\mathbf{r}). \quad (2.18)$$

This is similar to the theory of small reflections used for linearizing the nonlinear Riccati type equation in the previous section. Approximating the total field by the incident one allows the calculation of the scattered field in terms of the known illuminating field which is the first order Born approximation for the scattered field.

$$\mathbf{E}_s(\mathbf{r}) = \int G(\mathbf{r} - \mathbf{r}_0)O(\mathbf{r})\mathbf{E}_0(\mathbf{r}_0)d\mathbf{r}_0 \quad (2.19)$$

Equation (2.19) is a linearized version of (2.17) and is the basis for the derivation of the Fourier slice theorem which is the inversion of the linearized integral equation for the object. The Fourier slice theorem relates the Fourier transform of the measured data along a line to the two-dimensional spatial Fourier transform of the object along a circular arc [36]. Plane wave illumination is required in order to apply the Fourier diffraction theorem. The fields along the receiver lines must be measured using several illumination angles in order to acquire enough information to retrieve the spatial Fourier transform of the object accurately enough. The Fourier slice theorem is only valid when $\mathbf{E}_s(\mathbf{r}_0) \ll \mathbf{E}_0(\mathbf{r}_0)$, a condition implying that the scattering is weak. The total field at each point in the object must basically be equal to the incident wave used for illumination with no object present. This limits the range of objects to very weak scattering ones which additionally have to be virtually lossless. This prohibits the application of systems based on the diffraction tomography approach to any objects of practical interest.

This was pointed out in [36] as early as 1984. This paper also compares the accuracy of image reconstruction using the Born and the Rytov approximation. Both yield the same results when applied to very weak scattering objects. In addition to the weak scattering requirement the object must also be small in size when the Born approximation is applied which further limits the applicability. The Rytov approximation does not have this additional restriction as only the relative change of phase over one wavelength should be small. This only limits to weak scattering objects but is independent of object size. A comparative study shows that imaging

using diffraction tomography fails for refractive indices larger than $n \geq 1.1$. This study was carried out on simple homogenous cylinders and the reconstruction failed regardless of what approximation was used.

The devastating effect of losses on the results of diffraction tomography is assessed in [38]. In this paper cylinders with a relative permittivity of 1.01 with respect to the background are imaged using Born approximation diffraction tomography. The loss tangent of the homogenous cylinders is varied. While the image of this very low contrast object is acceptable for the lossless case the reconstruction fails for small loss tangents as 4%.

The use of multi-frequency data in combination with the Born approximation is proposed in [39]. Good results are achieved for simple geometries and weakly scattering low-loss objects. The authors conclude that an extension to the case of stronger scatterers is only possible by adopting nonlinear models. Also the need for accurate measurements and the requirement for accurate measuring system calibration is emphasized.

An experimental set-up for applying diffraction tomography to humans is presented in [40]. It uses a novel cylindrical antenna array for illuminating and receiving simultaneously. Although the basic imaging algorithm remains unchanged it avoids the problem of mechanically rotating the object or antenna array which is needed to collect the multi-view data. The system achieves a good spatial resolution at a quite low operating frequency of 2.45 GHz due to the use of distilled water as background medium. Because of the high permittivity of distilled water ($\epsilon_r = 77 - j9$) the wavelength is only approximately one ninth of the free-space wavelength. Although the system is capable of forming images of a human arm in vivo, the images are severely distorted. Reasons for this are again the weak scattering, low-loss assumptions.

Another prototype system for three-dimensional imaging of biological tissues is described in [41]. The system is capable of imaging phantoms that are close to human tissues in their complex permittivity. Replacing air by distilled water as a background medium is keeping the dielectric contrast low (10%) because the permittivity of the tissues is assumed to be in the same range. The images obtained are distorted due to the Born approximation approach and because of difficulties to obtain accurate measurements with the experimental set-up.

Another application of microwave imaging is temperature imaging of biological tissues as suggested in [42]. Assuming a known homogenous tissue its permittivity will depend on the temperature. The behavior of biological tissues is determined by the water content mainly. However, the change in permittivity over temperature is only $\frac{\Delta\epsilon'/\epsilon'(20^\circ C)}{\Delta T} = -3.9876 \cdot 10^{-3} K^{-1}$ for water. It is questionable if a biological tissue will be homogenous enough to measure such a small permittivity variation and trace it back to a temperature distribution. Consequently only simulations are given, where quite good accuracy is achieved as this really is a weak scattering problem. An useful aspect of this work is that the temperature dependence of the permittivity can be neglected for other microwave imaging applications.

As no algorithms for diffraction tomography which can be derived without using approximations are available, diffraction tomography is not considered to be a method which can be applied to problems of practical interest.

2.3 Iterative Methods

Several iterative approaches to three-dimensional microwave imaging have been proposed. All are based on the solution of the wave equation using Green's function for the solution for the scattered field (2.17) as it was shown in the previous section. The experimental set-up is the same as for diffraction tomography in figure 2.2. The object is illuminated using a number of L illumination angles equally spaced $\Theta_l = \frac{2\pi(l-1)}{L}$, with $l = 1 \dots L$. The M receivers are arranged along a line or circularly around the object under test. Contrary to diffraction tomography plane wave illumination is not necessary as the Fourier diffraction theorem is not applied. Only one element is radiating at a time. The scattered fields $\mathbf{E}_s^l(\mathbf{s}_{lm})$ at the observation point \mathbf{s}_{lm} can be calculated from the measured total fields at the receivers $\mathbf{E}_t^l(\mathbf{s}_{lm})$ and the known incident field $\mathbf{E}_0^l(\mathbf{s}_{lm})$ where l is the illumination angle and $m = 1 \dots M$ is the receiver location.

$$\mathbf{E}_s^l(\mathbf{s}_{lm}) = \mathbf{E}_t^l(\mathbf{s}_{lm}) - \mathbf{E}_0^l(\mathbf{s}_{lm}) \quad (2.20)$$

The direct problem is given by two coupled equations. The first is describing the coupling between total fields and incident fields. It holds for the object domain as well as the observation points but is evaluated over the object domain only.

$$\mathbf{E}_t^l(\mathbf{r}) = \mathbf{E}_0^l(\mathbf{r}) + \int \int_S G(\mathbf{r} - \mathbf{r}_0) O(\mathbf{r}_0) \mathbf{E}_t^l(\mathbf{r}_0) d\mathbf{r}_0 \quad (2.21)$$

The scattered fields are given by the observation equation which is evaluated at the observation points.

$$\mathbf{E}_s^l(\mathbf{s}_{lm}) = \int \int_S G(\mathbf{s}_{lm} - \mathbf{r}_0) O(\mathbf{r}_0) \mathbf{E}_t^l(\mathbf{r}_0) d\mathbf{r}_0 \quad (2.22)$$

For the representation of the object the contrast function

$$c(\mathbf{r}) = \begin{cases} \varepsilon_r(\mathbf{r}) - 1 & \text{if } r \in S \\ 0 & \text{if } r \ni S \end{cases} \quad (2.23)$$

is used. The background medium is again assumed to be free space. The object function $O(\mathbf{r}) = k_0^2 c(\mathbf{r})$ is the same as for diffraction tomography. The discrete equivalents of equations (2.21) and (2.22) are formed by dividing the object domain in N usually rectangular unit cells in which the material parameters are constant. The object function must be zero outside the object domain. The fields in the unit cells are also assumed to be constant. Equation (2.21) can then be written in matrix notation.

$$e_t^l = e_0^l + G^D O e_t^l \quad (2.24)$$

e_t^l , e_0^l are N element vectors containing the total and incident fields at the N cells the object is located at. These can be represented by scalars because the object cross section to image and the receivers are in the same plane. The scattered field caused by the object has a component in the same direction as the incident one under this condition. G^D is an $N \times N$ matrix containing the integrated Green's functions with

both source and observation points in the object domain and O is the $N \times N$ diagonal matrix containing the values of the object function in the cells $O_{ii} = o_i$ when o is an N element vector containing the values of the object function in the unit cells. The observation equation (2.22) reads in matrix notation

$$e_s^l = G^M O e_t^l o. \quad (2.25)$$

Here G^M is an $M \times N$ matrix containing the integrated Green's function with source points in the object domain and observation points at the measuring receiver locations. e_s^l is an M element vector containing the scattered field at the receiver locations. Rearranging (2.24) yields

$$e_t^l = (I - G^D O)^{-1} e_0^l, \quad (2.26)$$

where I is the $N \times N$ identity matrix. This gives the total field in terms of the unknown object function, the Green's functions and the known illuminating field. The solution of the direct problem is obtained by using the total fields from (2.26) to compute the scattered ones at the receivers using (2.25).

$$e_s^l = G^M O (I - G^D O)^{-1} e_0^l \quad (2.27)$$

The process of solving the direct problem and finding the scattered fields for a given object can be written shortly as

$$e_s = A(O) \quad (2.28)$$

where all L views have been included and A is a nonlinear vector function given by equation (2.27). A cost function containing the distance between the result of (2.28) and the measured scattered fields e_s^{meas} is defined. The solution of the inverse problem is searched by minimizing that cost function.

$$\min \Phi = \|e_s^{meas} - A(o)\| \quad (2.29)$$

This approach is common to most of the iterative schemes found in the literature. Only the iterative method used for the resulting nonlinear least-squares problem, the method for solving for the scattered field or the regularization methods are varied. The step in the object function ΔO at each iteration using Gauss-Newton is given by

$$\Delta O = (J^T J)^{-1} J^T (e_s^{meas} - A(O)), \quad (2.30)$$

where J is the Jacobian of A at the current object iterate and J^T is its conjugate transpose matrix. The condition number of $J^T J$ is very large and therefore the calculate step ΔO from the current object iterate to the next is very sensitive to errors in the measured data. Therefore the Levenberg-Marquardt method is preferred over the Gauss-Newton method for iterative imaging purposes. It solves for the step

$$\Delta O_\mu = (J^T J + \mu I)^{-1} J^T (e_s^{meas} - A(O)) \quad (2.31)$$

instead of using (2.30). The regularization parameter μ is a real positive number that weights the identity matrix that is added to the ill-conditioned $J^T J$ in order to improve the condition number and cure noise sensitivity. The iterative scheme as outlined above is used in most of the iterative imaging methods suggested [43], [44], [45] and [46].

It is equivalent to the second-order Born or distorted Born method [47]. These methods solve the linearized inverse problem first to obtain an object estimate. This is equivalent to first-order diffraction tomography (2.19). Then the direct scattering problem is solved to approximate the total field not by the rough estimate of being equal to the incident one, but as the total field in presence of the current object iterate. With this new and better estimate of the total field the next iteration is started until the residual error is reduced to the desired limit. By iteratively solving the linearized inverse problem (diffraction tomography) and the direct scattering problem the range of allowable contrasts can be increased by a factor of ten [48].

The difficulties to find a good choice for the regularization parameter are assessed in [46]. Because a regularization parameter chosen to small might lead to instability while a too large one will smooth the result and reduce resolution the proper selection of the parameter is crucial for the performance of the Levenberg-Marquardt method. Several strategies for the choice of the parameter are suggested while none of them works satisfactory for a sufficiently wide range of initial guesses and noise levels in the measuring data.

In [49] the simulated annealing technique and a Levenberg-Marquardt algorithm are used to reconstruct a simple 2D model of the human arm consisting of only 25 cells. The simulated annealing method is a stochastic optimization method introducing slightly modified estimates at each iteration. By doing so it can avoid getting trapped in local minima like deterministic optimization methods. Because this reminds of the physical annealing of an hot solid to an monocrystal of minimum energy the method is called simulated annealing. For iterative microwave imaging simulated annealing is found to require a very large number of iterations (25.000), while the Levenberg-Marquardt algorithm might not converge at all, especially when the initial guess is not close to the actual object. The divergence problem occurs for noiseless data. Therefore serious convergence problem for noisy measuring data are anticipated. The high number of iterations required makes the simulated annealing method computationally expensive.

The noise sensitivity of Levenberg-Marquardt and modified gradient iterative methods is investigated in [45]. In this work the data is collected at several frequencies in order to gain more information for the image reconstruction. For noiseless data both methods gave satisfactory images with some distortion and quite low resolution. The Levenberg-Marquardt method diverged completely for noisy input data, while the modified gradient method was able to retrieve a noisy image. All images obtained do not indicate that any of the iterative methods proposed may be suitable for practical applications.

A different approach for the regularization is suggested in [50]. The weak membrane model [51] and a non-negativity constraint are used as a weighted contributions to the cost function. The weak membrane model is approximating a two-

dimensional function by continuous sections when the tension of the membrane is weak while at the same time allowing steps by cutting the membrane when the tension on it is too large. The result looks like if a weak membrane was spanned over the original function giving the method its name.

The results obtained using this approach are of much better quality than the ones with the Levenberg-Marquardt method for scatterers consisting of several homogeneous regions. This is expected as the weak membrane model is an image processing technique originally developed to detect edges by separating homogeneous regions. Depending on the model parameters the result will be homogeneous regions, but gradually changes are not imaged adequately. The algorithm is therefore tailor made for a specific problem. This is not considered to be a useful approach as algorithms only working for specific objects will not contribute to an improvement of microwave imaging techniques. The tasks of image acquisition and image processing should be clearly separated until algorithms for certain technical or medical tasks are developed. When working towards a technology to implement microwave imaging based systems for specific applications using image processing algorithms will further enhance the image quality, target recognition etc. as is done for CT and MRT images today.

The problem of general applicability has also been recognized by the community of researchers working in the field. As a result common data sets were provided to test algorithms using the same real measuring data known as the Ipswich data set [52]. This has led to some improved diffraction tomography methods still failing for stronger contrasts [53] and also iterative imaging methods where the basic approach outlined above is used [54].

The limitations encountered with the iterative procedures described above are due to the nature of the inverse problems. As the direct problem can be solved without approximations the divergence and noise sensitivity are completely due to ill-posedness. This can be cured by improved iteration schemes and by collecting more independent and exact measuring data.

2.4 Confocal Imaging

The difficulties encountered with the algorithms outlined in the above two sections are due to the complex propagation of microwaves in inhomogeneous bodies. There are methods aiming on avoiding these complex propagation by focussing the signal to a point in the object. By doing this a local scanning effect can be achieved. The term confocal is used because the illuminating signal is focussed to a point in the object domain and the scattered signals generated at that point are focussed to the measurement receiver location also. This approach is also referred to as double focussing [55]. This is similar to a ray optics approach where a single object domain point located at the focal point of a lens system is scanned. In microwave confocal systems the scanning is achieved in the lateral plane by using highly directive antennas, microwave lens systems or by forming a synthetic aperture. Several physical set-ups can be used depending on how the focussing is achieved.

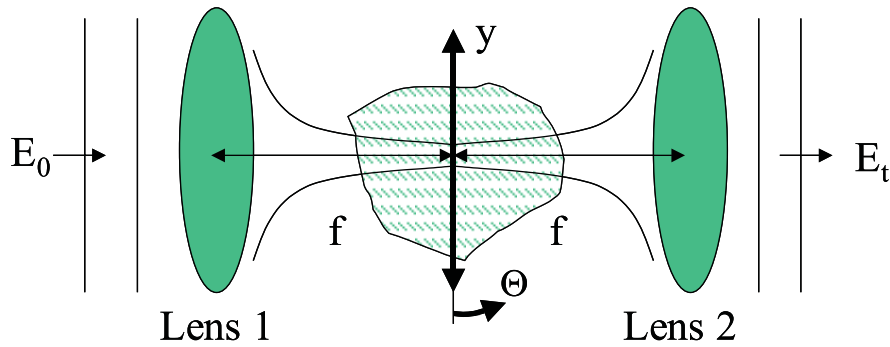


Figure 2.3: Confocal microwave imaging system

The one closest to confocal microscopy is the lens system as in [55]. Two lenses are located two focal lengths apart from each other while one is focussing the incident field E_0 radiated by a primary antenna. The second lens is collecting and refocussing the fields to the receiving primary antenna. The authors claim that they can achieve a narrow channel the signal is propagating along and by scanning the object in the transverse plane and recording the fields for each position a projection of the object can be obtained. As in the CT parallel beam protocol this is repeated for a number of illumination angles. The Fourier slice theorem can be applied to the data as line propagation is assumed. Obviously, this is only a valid assumption for the weak scattering case. While microwave radiation can be focussed in a single point in the absence of an object the focussing is not achieved when strongly scattering objects are placed in the search domain. The application examples show the limitations of this approach. The method is shown to work properly on styrofoam cylinders ($\epsilon_r = 1.05$) only. In the presence of strong scatterers it is expected that the field is scattered and multiple reflections occur destroying the focussing effect. This also explains why confocal imaging is successful in optics but fails for microwave applications. The beam propagation model is valid in the optical case but not for microwave propagation in the strong scattering case.

The same measuring set-up and parallel beam protocol for the image calculation are also used in [56]. A method for the estimation of the point spread function (PSF) of a confocal microwave imaging system is suggested based on measurements of a reference object. While the accuracy of the image is improved by deconvoluting the measured data with the estimate of the PSF the weak scattering limitations of confocal systems are not addressed in this work. The examples given are for very weak conductivity contrast.

The other imaging method using a localized focussing effect is adopting principles originally developed for ground penetrating radar (GPR) [57]. Ultrawideband signals are irradiated by single antennas that are scanned over the search domain and a synthetic aperture is formed from the measurements at the different locations [10]. The lateral spatial resolution is given by the radiation pattern of the physical or synthetic aperture used for lateral scanning. The depth resolution is determined

by the pulse width used for illumination. This requires ultrawideband antennas which should additionally be highly directive if a lateral scanning effect in the single measurements is to be achieved. These are high demands on the antenna system that are not fully met by current designs.

The focussed imaging approaches work satisfactory when applied to single scatterers in homogenous or weakly heterogenous backgrounds [58]. Besides the GPR this is promising for the detection of scatterers in weakly scattering background as breast tumor detection. Most confocal systems suggested are targeting this application [10], [58], [59] and [60]. In more complex situations when several strong scatterers causing multiple reflections the detection is not reliable any more and even the rough location of the strong scattering object becomes difficult. The clutter created by inhomogeneous backgrounds is also causing severe problems. Confocal methods are not aiming on quantitative information about the permittivity of an object. The focus in these methods is on detection and classification of scattering objects which is sufficient for mine or tumor detection problems.

2.5 Conclusion

None of the microwave imaging methods mentioned above is capable of stable quantitative imaging of strongly scattering and lossy objects. The common reason for this are unrealistic linear models and difficulties caused by the nature of inverse problems.

From the previous considerations can be concluded that a successful microwave imaging system will incorporate the following features:

1. Use of multi-frequency information.
2. Use of many transmitter and receiver positions.
3. Exact solution of the direct problem and usage of an iterative scheme.
4. Use of efficient regularization schemes to achieve stable convergence.
5. Measuring set-up allowing highly accurate vectorial measurements.

Chapter 3

Regularization and Iterative Algorithm for Imaging of Strongly Scattering and Lossy Objects

3.1 Regularization

3.1.1 Iterative Regularization Methods

As mentioned in section 1.4 microwave imaging is an inverse problem. It is exhibiting the properties of ill-posed problems as non-uniqueness, noise sensitivity caused by ill-conditioning of the corresponding linear systems and instability of iterative algorithms applied to it.

Figures 3.1 and 3.2 give an idea of that behavior of inverse electromagnetic problems. It is the problem of reconstructing a layered media from the reflection coefficient. The object consists of two layers, one consists of acrylic the other of air, each 1.5 cm long. The scattering matrix of this two layer object has been measured using a Vector Network Analyser (VNA). The measuring accuracy is good as can be seen by the good agreement between measured and simulated input reflection in figure 3.2. Although the start value for the permittivity profile is already very close to the actual one the solution found is entirely different. This is surprising as one would expect quick convergence to the actual solution if the initial guess is so close to the solution. But the ill-posedness of this problem causes a different behavior. The scattering parameters of the reconstructed object do match the measured ones very well (figure 3.2). However, the solution obtained is not acceptable because the reconstructed permittivity profile is entirely different compared to the actual one. It is characterized by large oscillations, the relative permittivity is even smaller than one or even negative. Thus a regularization must be applied in order to avoid such solutions.

The task is to reconstruct the object described by a number of n parameters from measurements of scattered fields or scattering parameters where the illumination signal is known. The number of measured field samples m is in most cases much larger than the number of parameters describing the object n . The obtained task is

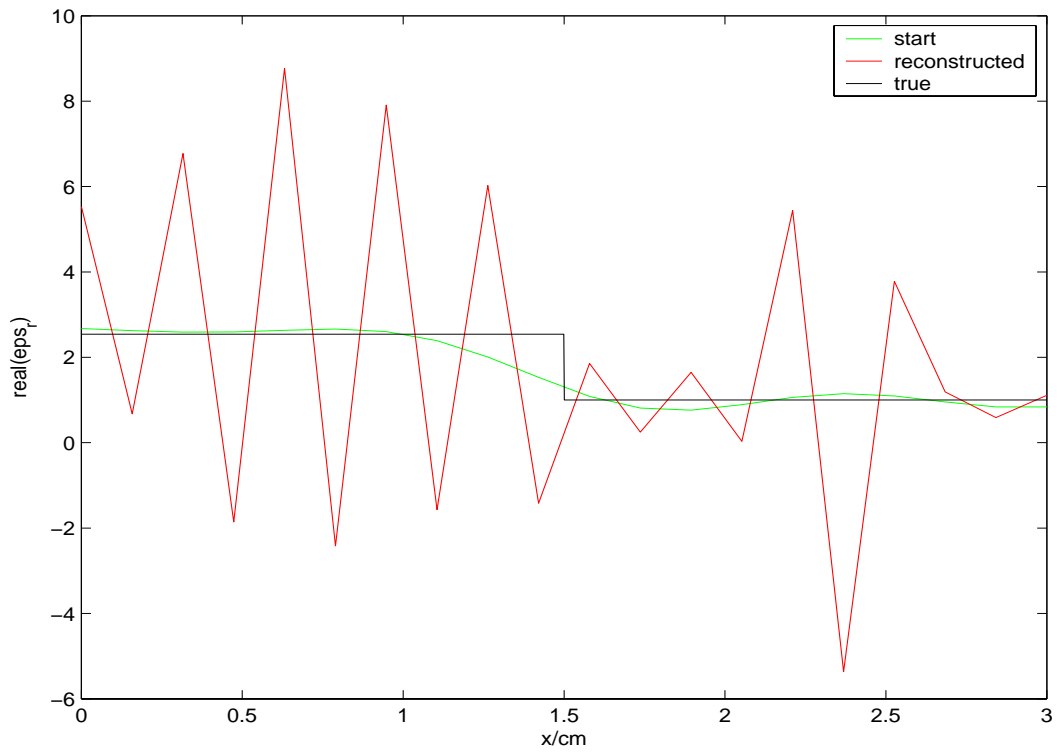


Figure 3.1: Unregularized solution of a layered media problem.

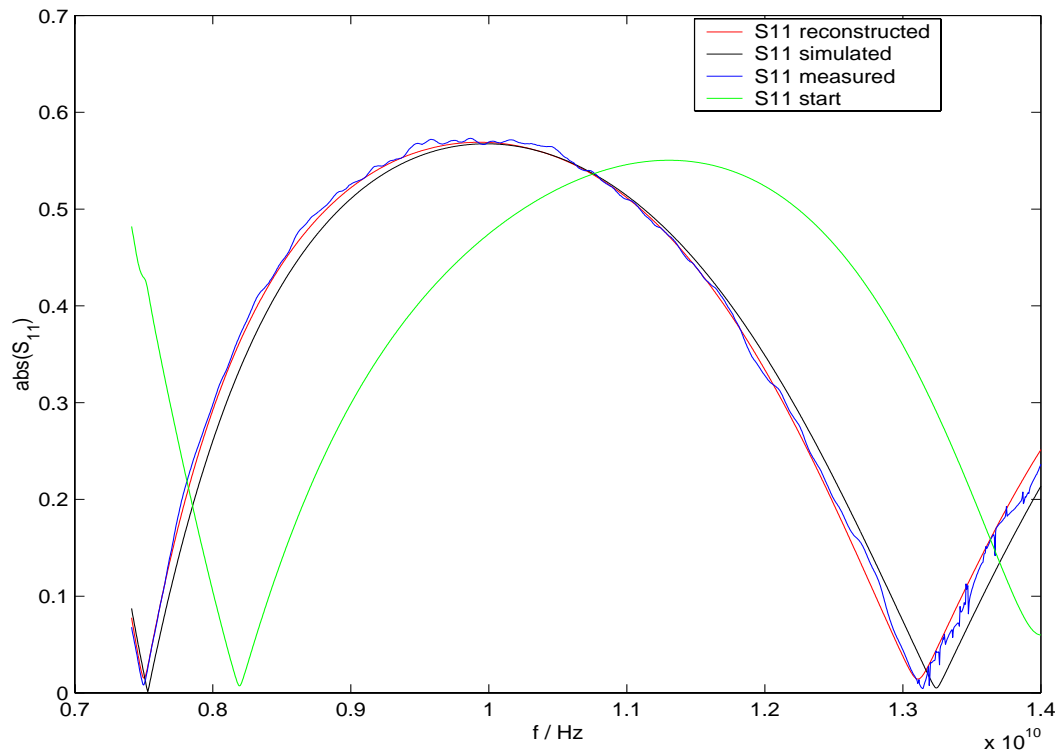


Figure 3.2: Magnitude of input reflection (measured, simulated, start and reconstructed) for the layered media problem in figure 3.1.

therefore the solution of a nonlinear least-squares problem. Using operator notation as introduced in section 1.4 this can be written as

$$\min_{f \in X} \|Af - g\|. \quad (3.1)$$

Because the solution of this problem corresponds to an inverse problem it is ill-posed. To obtain a solution of (3.1) despite of the difficulties mentioned above a regularization is applied. A regularization can be introduced by formulating additional constraints on possible solutions of (3.1). To achieve this, a suitable subset $\Omega \subset X$ is defined and it is required that all physically acceptable solutions of (3.1) fall within that subset. The resulting problem is

$$\min_{f \in \Omega \subset X} \|Af - g\|. \quad (3.2)$$

Because this constrained problem is very difficult to treat and no sufficiently verified algorithms are available, it must be reformulated to the structure of an unconstrained one. This is usually achieved by the method of penalty functions [61]. The problem can be shown to be equivalent to minimizing a new cost functional

$$\min_{f \in X} \Phi = \|Af - g\| + \mu h, \quad (3.3)$$

where μ is the positive regularization parameter and h is the stabilizing penalty function. The penalty function forms a linear combination with the unconstrained functional weighted by the regularization parameter and assures the unconstrained problem to converge to a solution in Ω by making outside solutions very expensive. Several penalty functions have been suggested and tested for applicability in inverse scattering problems [18]. All have in common that a priori information is used to confine the range of mathematically possible solutions to the subset of physically acceptable ones. The most used constraints are Tikhonov penalty function

$$h = \|f\| \quad (3.4)$$

where h simply represents the energy of the object and the solution of the unconstrained minimization will lead to the object with minimum energy minimizing the functional (3.3) to the desired limit. The justification for this is that physically acceptable solutions should have a limited energy. The Phillips penalty function, which is also referred to as second order Sobolev term, is defined by

$$h = \|f''\| \quad (3.5)$$

and requires that the object should be reasonably smooth. This is also a physically very reasonable choice and appears to be particularly useful for inverse scattering problems as many solutions obtained by solving the unregularized problem (3.1) are characterized by large oscillations of the object as seen in the example above.

Other regularization methods use a linear combination of the object energy and the 1st derivative to obtain a smooth object with low energy [18]. Recently the weak

membrane model [51] has been successfully adapted to inverse scattering problems in [50]. It uses a more complex membrane model to achieve a smooth object and at the same time allows for sharp boundaries at object interfaces. However, none of these regularization methods is applicable to a wide range of inverse electromagnetic problems.

3.1.2 Regularization and Bandlimiting

If the mapping operator was known it could be attempted to solve an inverse problem by inverting the direct one. For all practical cases the direct problem is given by

$$Af + \delta = g^* \quad (3.6)$$

where δ is the noise and g^* is the noisy measuring data. The resulting equation for the object f^* found from noisy data is

$$f^* = A^{-1}g^*. \quad (3.7)$$

The maximum acceptable error in the reconstructed object is e_{max} . For an inverse problem (3.7) will generally not give the desired solution $\|f^* - f\| < e_{max}$ due to the ill conditioning of A . The bad condition will cause strong noise amplification. The reasons for this can be identified using singular value decomposition (SVD) of A [62]. When A is a mapping of n object parameters to m data points it is an $m \times n$ matrix.

$$A = USV^T \quad (3.8)$$

Here $S = \text{diag}(s_i)$ is an $m \times n$ diagonal matrix containing the singular values of A on the diagonal and with zero elements elsewhere. The columns of the square $m \times m$ matrix U are the orthogonal left singular vectors and the columns of the $n \times n$ square matrix V the right ones. The inverse of A is then given by

$$A^{-1} = V \text{diag}(s_i^{-1}) U^T, \quad (3.9)$$

where $\text{diag}(s_i^{-1})$ is a $n \times m$ left diagonal matrix. This can be applied to equation (3.7). Using (3.6) for the measuring data yields

$$f^* = f + V \text{diag}(s_i^{-1}) U^T \delta. \quad (3.10)$$

Obviously, the small singular values are the source for the noise amplification as can be seen from (3.10). To eliminate this undesired behavior suitable weights on the singular values must be introduced. These should fulfill the condition

$$\lim_{s \rightarrow 0} w s^{-1} = 0 \quad (3.11)$$

An intuitive choice would be to set a threshold.

$$w_\alpha(s^2) = \begin{cases} 1 & \text{if } s^2 > \alpha \\ 0 & \text{if } s^2 \leq \alpha \end{cases} \quad (3.12)$$

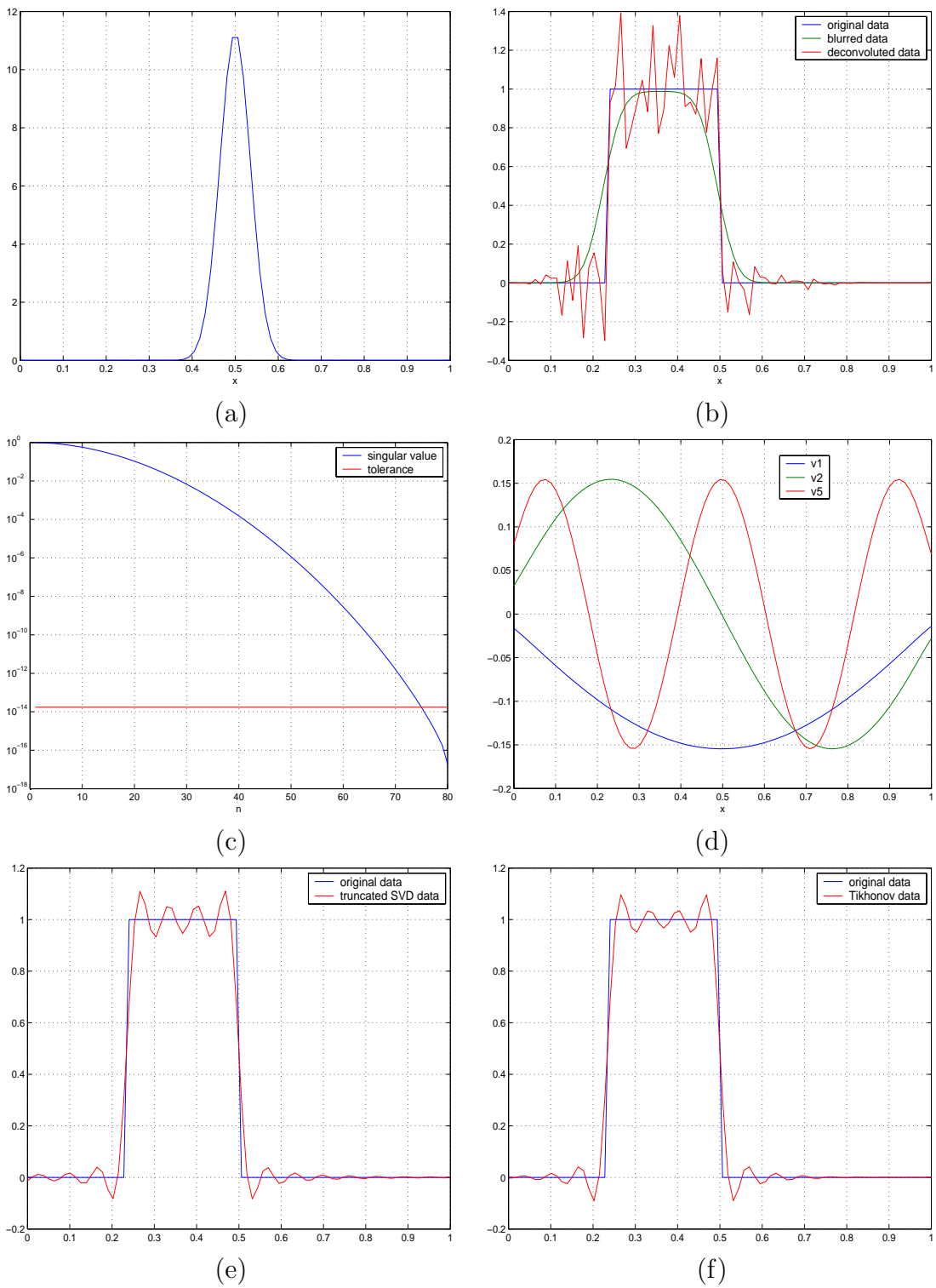


Figure 3.3: Image reconstruction example: The point spread function of the system (a). The original object(blue), the input collected by the system (green) and the unregularized reconstructed data(red)(b). The singular values of the system (c). Plots of the right singular vectors over the space variable (d). Reconstructed image using TSVD regularization (e). Reconstructed image using Tikhonov regularization (f).

The object reconstruction is then performed by

$$f_\alpha^* = V \text{diag}(w_\alpha(s^2)s_i^{-1})U^T g^* \quad (3.13)$$

This algorithm is known as the truncated SVD (TSVD) regularization. Its properties are assessed on the following example. An imaging system has the Gaussian sampling function $a(x - x')$ depicted in figure 3.3(a). This kind of sampling function is often observed in optical systems but is also a realistic choice for microwave imaging systems. This sampling function is called the point spread function (PSF) of the system. The object function f to image is the stepped pulse function shown by the blue line in figure 3.3(b). This object is sampled at $N=80$ discrete points by the system resulting in the matrix representation of the mapping operator A . The sampling process is basically a convolution of the object with the point spread function.

$$g^*(x) = \int_{x'=0}^1 a(x - x')f(x')dx' + \delta, \quad 0 < x < 1 \quad (3.14)$$

This convolution type sampling gives the blurred image shown by the green line in figure 3.3(b). For this example the noise level is just the limited accuracy of the floating point representation, so the data is virtually noiseless. Still the result obtained by applying (3.7) on the data is not satisfactory as depicted by the red line in figure 3.3(b). Despite the noiseless input data the reconstructed object is highly distorted. The reason for this can be seen from the plot of the singular values of A in figure 3.3(c). As A is a real valued matrix it has positive monotonically decreasing singular values. The rank of the discrete PSF is only 74 given the calculation tolerance. Consequently using (3.7) will cause great noise amplification even for virtually noiseless input data.

By applying the TSVD filter the inverse values of those small singular values are set to zero which avoids multiplying the noise with very large numbers in (3.10). The introduction of this weighting can be shown to be equivalent to bandlimiting the reconstructed object when observing the singular vectors of A . Three of the singular vectors are plotted in figure 3.3(d). The singular vector v_1 corresponds to the largest singular value of A . It is slowly varying in space and corresponds to the lowest part of the spectrum of A . The second and 5th order singular vectors have increasing spatial frequency. The singular vectors corresponding to the very small singular values are consequently oscillating with very high frequency. The TSVD filter cancels those highly oscillatory singular vectors. The TSVD regularization is therefore equivalent to bandlimiting the reconstructed object. This effect is shown in figure 3.3(e). The distortion of the unregularized solution can be removed but the edges of the pulse show Gibbs phenomenon due to the limited band. The result obtained by a regularized reconstruction will depend on the regularization parameter α . If it is too small noise amplification might occur, if it is too large the solution found will be smoothed due to the strong low-pass filtering.

The TSVD filter requires the SVD decomposition of A which is not necessary when applying the Tikhonov regularization. It uses the weight function

$$w_\alpha(s^2) = \frac{s^2}{s^2 + \alpha}. \quad (3.15)$$

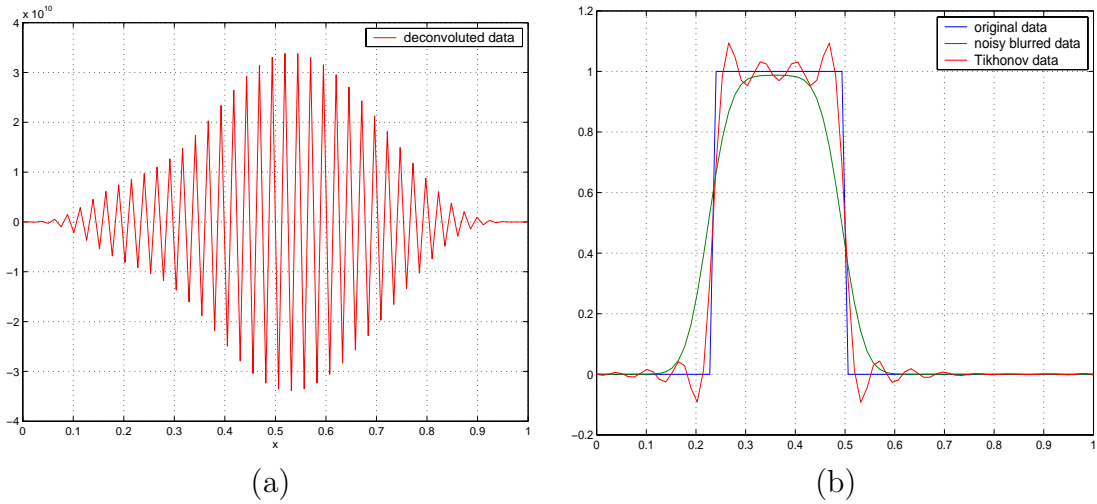


Figure 3.4: Reconstructed objects from data with 80 dB SNR: unregularized reconstruction(a), Tikhonov reconstruction(b).

This satisfies (3.11) also and has the additional advantage that that the SVD does not need to be computed explicitly. The object can instead be reconstructed using

$$f^* = (A^T A + \alpha I)^{-1} A^T g^*. \quad (3.16)$$

Additionally the results achieved using Tikhonov regularization are frequently superior to those obtained using TSVD. The proof of the equivalence of (3.16) and (3.13) is given in appendix A.

In the presence of noise the importance of a suitable regularization increases as in practical cases the distortion of the unregularized solution caused by noise amplification often is several orders of magnitude larger than the object itself. This effect is shown in figure 3.4. The same object as in the previous example is imaged using the same system but noise has been added to the measuring data. Although the signal to noise ratio is better than 80 dB which is more than one can expect for practical imaging applications the reconstruction of the object fails. The behavior of inverse problems in microwave imaging and optical imaging is similar. Again the object found by unregularized reconstruction is corrupted by strong oscillations as in the microwave profile reconstruction example in figure 3.1. The Tikhonov regularization with $\alpha = 1 \times 10^{-5}$ avoids the noise amplification and the result obtained in figure 3.4(b) is essentially identical to the previous noiseless case.

As equation (3.14) is basically a convolution of the object in the space domain the frequency domain equivalent can be used to show the necessity of bandlimiting the reconstruction. The equivalent of (3.7) reads

$$f^* = \mathcal{F}^{-1} \left\{ \frac{\mathcal{F}(g^*)}{\mathcal{F}(a)} \right\}. \quad (3.17)$$

The Fourier transform of the system PSF is the transfer function $\mathcal{F}(a)$. The reconstructed object is not defined from (3.17) if the transfer function is zero for any

frequency point. For small values the noise in the measuring data will be amplified as discussed above.

3.1.3 Spectral Expansion of the Object Function

In microwave imaging applications the direct mapping operator is generally not known. Additionally it is not space invariant as required to apply an inverse solution as on the previous optical example. Iterative algorithms involving the solution of the linearized direct problem or the solution of the nonlinear direct problem are used. As outlined in section 2.3 all iterative approaches to inverse electromagnetic scattering developed so far represent the object by a number of discrete samples. These samples are the material parameters of usually rectangular unit cells. The material properties of these homogenous blocks are then optimized in the iterative algorithm. There exists no relation between one sample to the neighboring ones in the unconstraint problem. This relation is established by adding constraints on the smoothness which means one tries to find an object which has minimum change from one sample to the next and still matches the measured data to the desired accuracy. Obviously this is not the most efficient way to formulate the regularization. Also the solution found will strongly depend on the choice of the regularization parameter while the optimum choice for it is not known in advance and can at best be estimated [63]. As the value of the regularization parameter can vary over several decades, it has been found empirically in most known examples by carrying out experimental reconstructions and selecting the result most reasonable. This is called the interactive method and is still used for many problems [18]. To overcome these drawbacks a new regularization scheme based on the spectral expansion of the object is proposed here. The permittivity distribution is expanded into a complete set of orthogonal functions. The permittivity is used here as it is the mostly imaged electromagnetic parameter but the same approach can be used for conductivity and permeability also.

$$\varepsilon(x, y, z) = \sum_{n=0}^N d_n f_n(x, y, z) \quad (3.18)$$

Completeness must be given in order to be able to expand arbitrary objects into the set. Orthogonality is favorable because a finite series will always represent the object with the best possible accuracy and coefficients will remain unchanged while increasing the number of expansion functions. The orthogonality condition is given in (3.19) where $N(i)$ is the norm of the function f_i .

$$(f_i f_j) = \int_V f_i \cdot f_j dV = \begin{cases} 0 & \text{for } i \neq j \\ N(i) & \text{for } i = j \end{cases} \quad (3.19)$$

For the expansion cosine or sine functions as well as orthogonal polynomials can be used. For the purpose of solving the inverse electromagnetic scattering problems the expansion into a set of cosine functions (3.20) is most favorable for the following reasons. The expansion of a unknown three-dimensional object in cartesian coordinates

in terms of a cosine-series reads:

$$\varepsilon_r(x, y, z) = \sum_{n=0}^N \sum_{m=0}^M \sum_{l=0}^L d_{nml} \cos(k_{xn}x) \cos(k_{ym}y) \cos(k_{zl}z), \quad (3.20)$$

where $k_{xn} = \frac{n\pi}{a}$, $k_{ym} = \frac{m\pi}{b}$ and $k_{zl} = \frac{l\pi}{c}$ are the spatial frequencies along the x, y and z direction. The object is now represented by the expansion coefficients d_{nml} which are the parameters for the optimization. The reason to favor cosine over sine functions is simply that in the above expansion only the coefficient with zero spatial frequency in all directions d_{000} will carry information about the average permittivity in the object while all others are free of contributions to the mean value. In the sine case all coefficients having an odd index will contribute to the mean value. As will be shown it is favorable to separate the average material parameters from the higher coefficients. The benefit of harmonic functions over other orthogonal sets of polynomials is the special relation to the measured data. This can be shown on the example of a one-dimensional layered media problem. The expansion of a layered media along z which is homogenous along the transverse plane is

$$\varepsilon_r(z) = \sum_{n=0}^N d_n \cos\left(\frac{n\pi z}{c}\right) \quad (3.21)$$

The layered media is lossless so only the real part of the relative permittivity is considered. By solving the Riccati differential equation for the reflection coefficient and linearizing by dropping the quadratic term as in section 2.1 one obtains equation (2.3) which is repeated here for convenience.

$$\Gamma_{in}(k_0) = -\frac{1}{4} \int_{z=0}^c \frac{1}{\varepsilon_r(z)} \frac{d(\varepsilon_r(z))}{dz} e^{-2jk_0\sqrt{\varepsilon_r(z)}z} dz \quad (3.22)$$

This is a Fourier transform of the permittivity profile into the frequency domain. Although this has been obtained by neglecting the quadratic term in the reflection coefficient, from this result it can be seen that for a harmonic variation in permittivity a reflection coefficient over frequency function is obtained which resembles the spectrum of a pulse modulated carrier. This is a sinc function where the center frequency is proportional to the carrier frequency which is the spatial frequency of the permittivity change. This function has a region of maximum magnitude when the average propagation constant throughout the object is

$$\bar{\beta} = \frac{n\pi}{2c} \quad (3.23)$$

This allows to assign a certain frequency range to each expansion coefficient d_n in (3.21) where it will have its strongest effect on the scattering data. Therefore it is now possible to relate each parameter describing the object to a certain subset in the measured data set. This is not possible in the standard iterative approaches using discrete blocks. This beneficial effect of the spectral expansion is shown in figure 3.5. The magnitude of the reflection for profiles created by a homogenous background

and the expansion coefficients d_2 , d_4 and d_8 were calculated using numerical solution of the Riccati equation. The region of maximum magnitude of the reflection data is shifting to higher frequencies for increasing order of expansion coefficient. This frequency range is later used in the iterative algorithm to optimize exactly the corresponding expansion coefficient.

3.1.4 Formulation of the Smoothness Constraint

A further benefit of the spectral object representation introduced in the previous section is that it also allows easy formulation of smoothness. No additional stabilizing functions of the type (3.5) are required to limit the search domain to reasonably smooth objects. This can now be done by limiting the number of expansion terms. The second derivative of the expansion (3.21) with respect to z is derived in appendix C.

$$\frac{d^2 \varepsilon_r(z)}{dz^2} = C_1 + \sum_{n=1}^N (C_2 - d_n k_n^2) \cos(k_n z). \quad (3.24)$$

Here C_1 and C_2 are two constants determined by the values of the first derivative of the permittivity function at the borders of the interval at $z = 0$ and $z = c$. According to equation (3.24) the maximum of the second derivative in the expansion region along z is depending quadratically on the spatial frequencies of the terms used for the expansion. This allows to require smoothness by limiting the number of expansion coefficients N . By doing this the occurring spatial frequencies k_n can be limited $k_n < k_N$. All objects with finite expansion coefficients have a smoothness quadratically dependent on the number of functions used for the expansion. This number is now the number of dimensions of the spectral object representation. The subset defined by the regularization in (3.2) is therefore

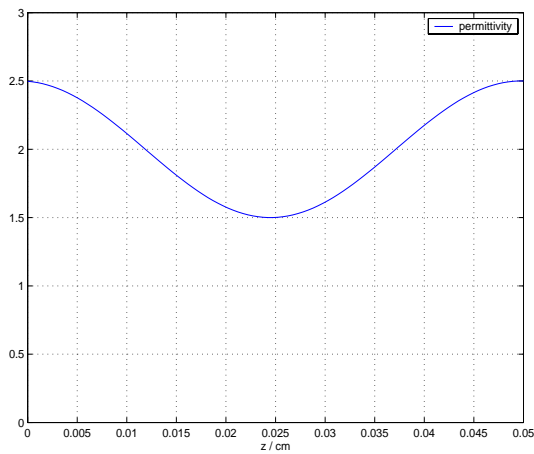
$$\Omega^N = \mathcal{R}^N \quad (3.25)$$

All objects in this N -dimensional domain are sufficiently smooth and the problem reduces to a nonlinear least squares problem.

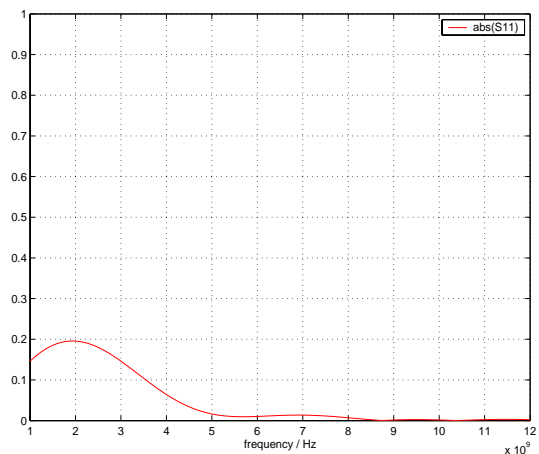
$$\min_{\tilde{f} \in \Omega^N} \|\tilde{A}\tilde{f} - g\|, \quad (3.26)$$

where Ω is defined by equation (3.25) and \tilde{f} is the spectral object representation. Note that the operator A has been replaced by a new operator \tilde{A} which maps the spectral object representation to the measuring space. Equation (3.26) gives the remarkable result that by transforming the object using (3.20) a constrained optimization problem can be formulated without explicitly formulating a subset as in (3.2) or using regularization parameters and penalizing functions as in (3.3). There is no bound on the expansion coefficient d_n or d_{nml} in the three-dimensional case which can be proven rigorously.

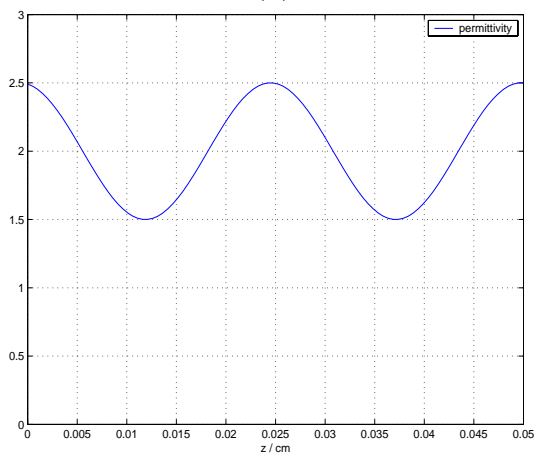
The spectral object representation by a limited number of expansion terms shows similarities to the TSVD and Tikhonov regularization. Limiting the dimension of the object space is equivalent to cancelling the highly oscillatory singular vectors



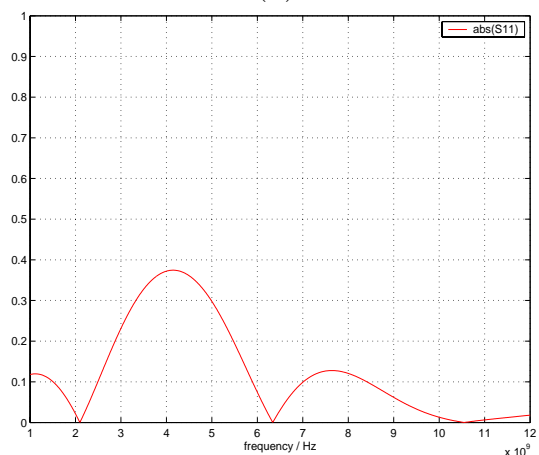
(a)



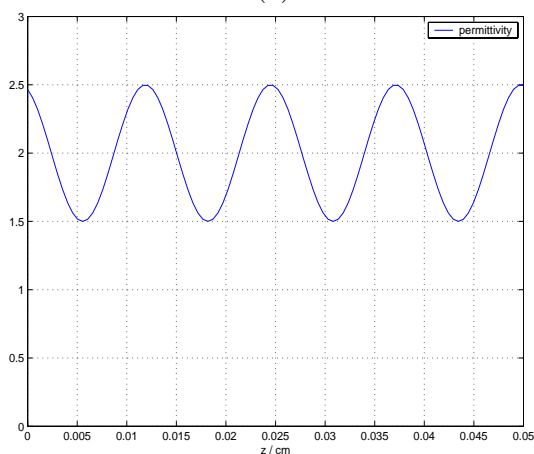
(b)



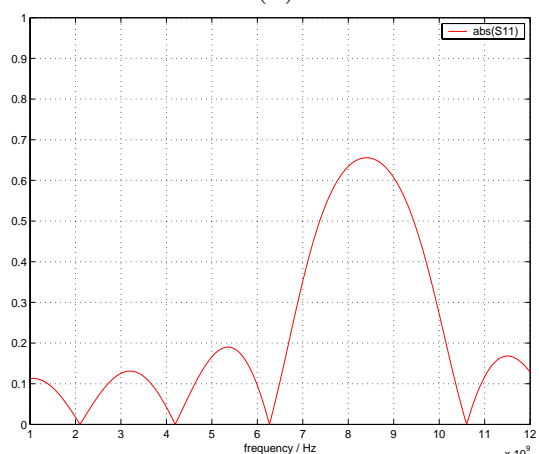
(c)



(d)



(e)



(f)

Figure 3.5: Permittivity functions and corresponding magnitude of reflection: permittivity profile with $d_2 = 0.5$ (a), permittivity profile with $d_4 = 0.5$ (c), permittivity profile with $d_8 = 0.5$ (e), and the corresponding magnitudes of the input reflection coefficient as function of frequency (b),(d),(f)

by weighting their corresponding singular values in (3.13). Although the effect is equivalent the regularization using spectral expansion is suitable for iterative methods when the mapping operator A and its SVD are not known.

The measuring frequency band can now be related to the object reconstruction prior to the start of the iterative algorithm. A maximum number of expansion coefficients can be selected due to the known measuring frequency band. Only those expansion terms that have their frequencies of maximum effect in the measuring band according to (3.23) are included in the regularized solution. Ill-conditioning by exceeding the system bandwidth in (3.17) can so be avoided as can also be verified by numerical simulation. In microwave imaging iterative schemes this is not possible with any other known method as the system transfer function is not known. Consequently it is also not known in advance for what number of cells the reconstruction will get ill-posed. It has been observed that the ill-conditioning is getting worse with the number of cells used in the reconstruction [63], but no explicit rules can be given to select it in advance. Being able to estimate the resolution achievable is the major advantage of the proposed regularization over microwave imaging schemes using the discrete cell approach.

3.1.5 The Successively Relaxed Smoothness Constraint

As the ill-posedness of the microwave image reconstruction is now cured the convergence of the iterative process to the desired solution is addressed. Experimental work shows that the smoothness constraint described in the previous section leads to a problem which is not ill-posed as an unconstrained discrete problem but still does not reliably converge to the desired solution. The regularization avoids solutions showing large oscillations but does not cure a problem connected to many nonlinear problems: non-uniqueness.

The observation that at low frequencies rather the averaged permittivity throughout the object is measured while details are detected at higher measuring frequencies leads to the method of the successively relaxed smoothness constraint. This is a subspace method which solves for the best solution in a given resolution while using a measuring frequency band which corresponds to the expansion coefficients currently determined. By applying condition (3.23) which gives a useful relation between each expansion coefficient and its frequency range of maximum effect this observation can be incorporated into the iterative imaging algorithm.

The algorithm first solves for a very smooth object which fits the data in the low frequency range. Smoothness of the object is obtained by represented it by a small number of expansion functions. When this object is found the smoothness constraint is relaxed and a new object which is not as smooth and fitting the data over a wider frequency band is searched. That means that the dimension of the image space is also increasing while the object space is increasing its dimension. When starting from an initial guess sufficiently close the current object will always be very close to the actual one in the given resolution. This process is started with $N = 1$ which means that only a guess for the average permittivity is needed. An initial guess good enough can always be found in practical applications as will be

shown in chapters 4 and 5. This consideration suggests to leave the simultaneous equations nonlinear least squares problem and to reformulate to

$$\min_{\tilde{f}_n \in \Omega^N} \|\tilde{A}\tilde{f}_n - g_n\| \text{ for } N = 1, 2 \dots N^{max}. \quad (3.27)$$

The solution $\tilde{f}_n \in \Omega^N$ found for a number of N expansion terms is the start guess for the new problem in the object space Ω^{N+1} , where the new expansion coefficient is always initialized to zero. The number of m scattering parameters that form the data set $g_n \in R^m$ is much larger than the number of optimization parameters n . The maximum achievable resolution is limited by the number of expansion coefficients determinable N^{max} . This number depends on the measuring frequency range and on the measuring accuracy. These dependencies are examined by numerical experiments in chapter 4.

This regularization scheme puts special requirements on the iterative algorithm used to implement it. A suitable iterative method is developed in the next section.

3.2 Iterative Algorithm

3.2.1 Nonlinear Least-Squares

In an inverse electromagnetic problem one deals with the problem of fitting m data points which represent measured field samples or scattering parameters with the exact or approximate solution of the direct problem which are the simulated field samples or scattering parameters. The direct problem is the mapping of the n parameters describing the unknown object to the measurement space. These parameters are the expansion coefficients of the permittivity distribution according to (3.20). Usually the number of measured quantities is much larger than the number of parameters describing the unknown object which leads to the nonlinear least-squares problem:

$$F : \mathbb{R}^n \rightarrow \mathbb{R}^m, \quad m > n \quad (3.28)$$

$$\min_{x \in \mathbb{R}^n} \frac{1}{2} F^T(x) F(x) = \frac{1}{2} \sum_{i=1}^m (f_i(x))^2,$$

where the residual function F is nonlinear and f_i is the i th component of F . $F^T(x)$ is the conjugate transpose vector of $F(x)$. This can be considered to be a special case of the unconstrained minimization problem

$$f : \mathbb{R}^n \rightarrow \mathbb{R} \quad (3.29)$$

$$\text{find } x_* \in \mathbb{R}^n \text{ for } f(x_*) < f(x) \text{ for every } x \in \mathbb{R}^n$$

Both problems are closely related when f is defined as

$$f(x) = \frac{1}{2} F^T(x) F(x) = \frac{1}{2} \sum_{i=1}^m (f_i(x))^2. \quad (3.30)$$

However, the iterative algorithm should take into account the special structure of (3.28) and not use one of the standard algorithms for unconstrained minimization [64]. The corresponding unconstrained minimization problem (3.29) is used for the development of a strategy for global convergence. The definition of global convergence is in accordance to [64] and [65] and means the convergence to a local minimizer from an arbitrary starting point. Methods for constrained minimization [66] need not to be reviewed as the problem has been reformulated to an unconstrained one in section 3.1.

The standard Newton method for unconstrained minimization reads

$$x_{k+1} = x_k - \frac{\nabla f(x_k)}{\nabla^2 f(x_k)}. \quad (3.31)$$

Here x_k is the current iterate, x_{k+1} is the next iterate, $\nabla f(x_k)$ is the gradient

$$\nabla f(x) = \left[\frac{\partial f(x)}{\partial x_1} \cdots \frac{\partial f(x)}{\partial x_n} \right]^T \quad (3.32)$$

of the cost function f and $\nabla^2 f(x_k)$ is its Hessian. The elements of the Hessian are by definition

$$\nabla^2 f(x)_{ij} = \frac{\partial^2 f(x)}{\partial x_i \partial x_j}. \quad (3.33)$$

Using the cost function according to (3.30) yields the gradient

$$\nabla f(x) = J^T(x)F(x) \quad (3.34)$$

where $J(x)$ is the Jacobian at the current point.

$$J(x)_{ij} = \frac{\partial f_i(x)}{\partial x_j} \quad (3.35)$$

The Hessian of f is

$$\nabla^2 f(x) = J(x)^T J(x) + S(x) \quad (3.36)$$

with

$$S(x) = \sum_{i=1}^m f_i(x) \nabla^2 f_i(x). \quad (3.37)$$

The derivation of these expressions for the gradient and the Hessian are given in appendix B. Using (3.34), (3.36) and (3.37) in the Newton method for unconstrained minimization yields

$$x_{k+1} = x_k - (J(x_k)^T J(x_k) + S(x_k))^{-1} J(x_k)^T F(x_k) \quad (3.38)$$

This is the method most efficient for the considered problem when $J(x)$ and $S(x)$ are available as it will converge quadratically to a minimizer of (3.28). By definition of quadratic convergence the sequence of iterates will satisfy for constant C

$$\|x_{k+1} - x_*\| \leq C \|x_k - x_*\|^2, \quad C > 0. \quad (3.39)$$

In many practical problems $J(x)$ is available but $S(x)$ is not. Additionally it is very expensive to approximate $S(x)$ by finite differences. For these reasons (3.38) is not frequently used to solve nonlinear least-squares problems in practice. A more practical algorithm is obtained by using a linear model of $F(x)$ around the current point.

$$M_k(x) = F(x_k) + J(x_k)(x - x_k) \quad (3.40)$$

This model can be minimized using its linear least-squares solution.

$$x_{k+1} = x_k - (J(x_k)^T J(x_k))^{-1} J(x_k)^T F(x_k). \quad (3.41)$$

This method selected for the solution of (3.28) is the Gauss-Newton method. If $F(x)$ is linear it will give the minimizer x_* in the first iteration. For nonlinear problems (3.41) is applied subsequently to determine the next iterate. Equations (3.38) and (3.41) are only different in the term $S(x)$. If it is negligible compared to $J(x_k)^T J(x_k)$ the Gauss-Newton method will converge quadratically as the Newton method. If $S(x)$ is large it might not converge. The Gauss-Newton method should

therefore only be applied to zero-residual or small-residual problems. In case the residual function f_i are small $S(x)$ will also be small and can be neglected without threatening convergence.

For microwave imaging problems using noiseless data quadratic convergence is assured as it is theoretically a zero residual problem. When using measured data the problem will transform to a small residual problem due to the measurement errors. As these residuals are expected to be small for reasonably accurate measurements and direct problem solutions the Gauss-Newton method will converge quadratically or at least linearly [64].

A drawback of the Gauss-Newton algorithm is that the step is not well-defined if $J(x_k)$ does not have full column rank. The resulting linear problem for the step s

$$J^T J_s = J^T F \quad (3.42)$$

is badly conditioned in that case and would lead to errors in the calculation of the step s . This case should not occur as the physical set up and the frequency range assignment have been made to achieve a well-conditioned system. This can be verified by simulation also. When the measurement frequency range is chosen properly, $J(x_k)$ is well-conditioned for the whole iterative process. When it is too small, the condition is getting worse when higher order expansion coefficients are included into the optimization process. The condition of the Jacobian is a measure for how strong the measured data depends on the parameters. When parameters are included into the optimization which do not have any effect on the measured data the condition of the Jacobian will get worse.

The Levenberg-Marquardt method [65] does not have the drawback of being as sensitive to the condition of $J(x_k)$. This is achieved by adding a weighted unity matrix to the Jacobian prior to its inversion. Due to that approach it shows slower convergence in most cases [67]. As all computational effort is negligible compared to function evaluations, a low total number of function evaluations is the main goal in the development of the iterative algorithm. It is therefore preferred to use the fast Gauss-Newton Method and assure a well conditioned system by properly designing the measurement system and parameters. Search algorithms like Nelder-Mead algorithm [65] with the benefit of not requiring derivatives are not applicable because of the high number of parameters describing the object. This would lead to a search requiring a very high number of function evaluations. The same applies to genetic algorithms which would require a very large population for the problem considered here [68].

3.2.2 Hybrid Jacobian Approximation

Some modifications to the standard algorithms are necessary for the solution of the inverse problem. The first is that the nonlinear function F is not known analytically and its numerical evaluation is computationally very expensive. The Gauss-Newton algorithm requires the calculation of the Jacobian

$$J(x) \in \mathbb{R}^{m \times n} \quad (3.43)$$

at every iteration step. An evaluation of the Jacobian using the finite difference method takes one calculation of the direct problem per parameter with finite differences.

$$J(x)_{ij} = \frac{\partial f_i(x)}{\partial x_j} \approx \frac{f_i(x + he_j) - f_i(x)}{h} \quad (3.44)$$

Here h is the step width and e_j is the j th column of the identity matrix. This requires a total of n direct problem solutions. The advantage of using a finite difference time domain (FDTD) solver for the solution of the direct problem is here that it yields all m functions, which are the scattering parameters at different frequencies in one direct problem solution. The direct problem solution can require more than one FDTD solver run as each solver run gives one column of the scattering matrix [69]. Frequency domain solvers would need one run for each frequency point. The more exact central difference approximation

$$J(x)_{ij} = \frac{\partial f_i(x)}{\partial x_j} \approx \frac{f_i(x + he_j) - f_i(x - he_j)}{2h} \quad (3.45)$$

cannot be used as it will consume twice as much calculation time and is therefore too expensive to obtain. The largest error contribution in the calculation of the Jacobian is the error of the evaluation of the direct problem. As exact solutions of full 3D structures are computationally very expensive, a compromise between speed and accuracy of the direct problem solution must be made. The error introduced by the finite difference approximation can therefore be neglected compared to the one introduced by the solution of the direct problem itself. No improvement justifying the additional computational expense is expected from using (3.45).

Also the special needs of the iterative imaging of the object using the spectral expansion and the regularization must be met. From the regularization follows that not all parameters are included in the optimization at the beginning. They are included in the order of their corresponding frequency of maximum effect on the scattering parameters. At the same time, the number of functions included in the minimization functional is increased. This means that the size of the Jacobian is constantly increasing during the iteration process. The known methods for the optimization of computationally expensive functionals are for simultaneous nonlinear equations only. In contrast to that the dimensions of the object space n and the image space m are constantly increasing for the problem considered here.

These special requirements for the minimization problem lead to the following strategy: As the Gauss-Newton method gives fast local convergence a method based on it should be applied to achieve convergence in a small number of iteration steps. These methods require the Jacobian $J(x_k)$ at the current object x_k . The calculation of the Jacobian needs one solution of the direct problem per optimization parameter for the finite difference approximation (3.44) which is unacceptable. When the number of parameters and equations remains unchanged between two iteration steps, Broyden's method [70] can be used. This method is based on trying to minimize the change to an already known Jacobian J or its Broyden approximation \tilde{J} and still satisfying the secant equation of the current iteration step. The current step in the

parameters is denoted

$$s_k = x_{k+1} - x_k, \quad (3.46)$$

where x_{k+1} is the new object and x_k is the starting object in the current iteration step. The difference in the corresponding images is the yield

$$y_k = F(x_{k+1}) - F(x_k). \quad (3.47)$$

The Jacobian approximation \tilde{J} for the next step must fulfil

$$\tilde{J}_{k+1}s_k = y_k, \quad (3.48)$$

which is the secant equation for the current iteration step k . The looked for Jacobian approximation for the next step is not uniquely defined by the secant equation. The additional condition used in a Broyden update is that the difference between the current Jacobian or its approximation to the next should be minimized. \tilde{J}_{k+1} can then be uniquely determined using this condition. The idea of trying to minimize the change between two subsequent Jacobian approximations is based on the fact that some initial Jacobian has been obtained for the first iteration and as much of it as possible should be preserved for the next iterations. When a number of subsequent iterations is carried out, the Broyden approximation of the Jacobian may become inaccurate and the convergence will slow down. In this case it must be reset to good approximation at the current point. For this purpose the finite difference approximation can be used. Because there is new information in the direction of the current step s_k only, it is required that \tilde{J}_{k+1} and \tilde{J}_k agree for all vectors t orthogonal to the current step s_k . For all these vectors

$$t^T s_k = 0 \quad (3.49)$$

holds. The difference between the two subsequent Jacobian approximations fulfils

$$\left(\tilde{J}_{k+1} - \tilde{J}_k\right) t = 0 \quad (3.50)$$

for all those vectors t . This implies that $(\tilde{J}_{k+1} - \tilde{J}_k)$ is a rank one matrix. Every column of $(\tilde{J}_{k+1} - \tilde{J}_k)$ can be expressed as a multiple of a common vector u . The difference between the two Jacobians is then given by

$$\tilde{J}_{k+1} - \tilde{J}_k = uv^T. \quad (3.51)$$

Using (3.51) in (3.50) yields

$$uv^T t = 0. \quad (3.52)$$

This requires $t^T v = 0$ and can only hold for $v = s_k$ or an multiple of it by definition of t in equation (3.49). The difference between the Jacobians can now be written as

$$\tilde{J}_{k+1} - \tilde{J}_k = us_k^T, \quad (3.53)$$

where u is still unknown. Subtracting $\tilde{J}_k s_k$ from the secant equation (3.48) yields

$$\left(\tilde{J}_{k+1} - \tilde{J}_k\right) s_k = y_k - \tilde{J}_k s_k \quad (3.54)$$

By combining this with (3.53) the unknown vector u can be determined.

$$u = \frac{y_k - \tilde{J}_k s_k}{s_k^T s_k} \quad (3.55)$$

Substituting u in (3.53) gives the result for the minimum change update to the current Jacobian fulfilling the secant equation.

$$\tilde{J}_{k+1} = \tilde{J}_k + \frac{y_k - \tilde{J}_k s_k}{s_k^T s_k} s_k^T \quad (3.56)$$

This method can be used to update the Jacobian for a set of simultaneous equations where the number of parameters as well as the number of equations remains unchanged between iteration steps. For the regularization applied here this is not true. Therefore a different method must be used. The number of parameters n is increased by one at each iteration step, while the number of equations m is kept constant for a small number of subsequent iterations. We can now use the updated Jacobian approximation $\tilde{J}_{k+1} \in \mathbb{R}^{m \times n}$ from (3.56) and the finite difference approximation for the Jacobian column of the new optimization parameter x_{n+1}

$$\bar{J}_{k+1} = \frac{F(x + h e_{n+1}) - F(x)}{h}, \quad \bar{J}_{k+1} \in \mathbb{R}^{m \times 1} \quad (3.57)$$

to form a hybrid Jacobian approximation for the next iteration step. Here e_{n+1} is the $n + 1$ th column of the identity matrix. The dimension of the parameter vector x is increased from n to $n + 1$ when using (3.57). This requires to provide an initial guess for this parameter. In this algorithm implementation the new parameters are set to zero.

$$\hat{J}_{k+1} = [\tilde{J}_{k+1} \bar{J}_{k+1}], \quad \hat{J}_{k+1} \in \mathbb{R}^{m \times n+1}. \quad (3.58)$$

That hybrid Jacobian approximation does only require one solution of the direct problem. The effect of that method on the number of function evaluations is shown in figure 3.6. Here it has been assumed that the hybrid Jacobian approximation is reset once for every ten optimization parameters and that two subsequent iterations are carried out with the same settings. The substantial savings in function evaluations are crucial in order to obtain a solution in acceptable time.

In all iterative schemes using Broyden updates the Jacobian is reset to an analytical or finite difference approximation when the improvement between iterates gets to small. In our algorithm this is done after a number of iterations using (3.58). At this point the number of equations m is increased and the full Jacobian is approximated using (3.44). As this is recommended anyway in order to avoid inexact Jacobian approximations [64] no function evaluations are unnecessarily carried out. The convergence of this method is quadratical for the full finite difference iterations as these are Gauss-Newton iterations using a Jacobian on a very small residual problem, which have the same convergence as the Newton method. For the iterations using the hybrid Broyden approximation at least superlinear convergence as for the standard Broyden approximation is expected. The convergence of the algorithm using (3.58) cannot be shown rigorously due to its hybrid structure.

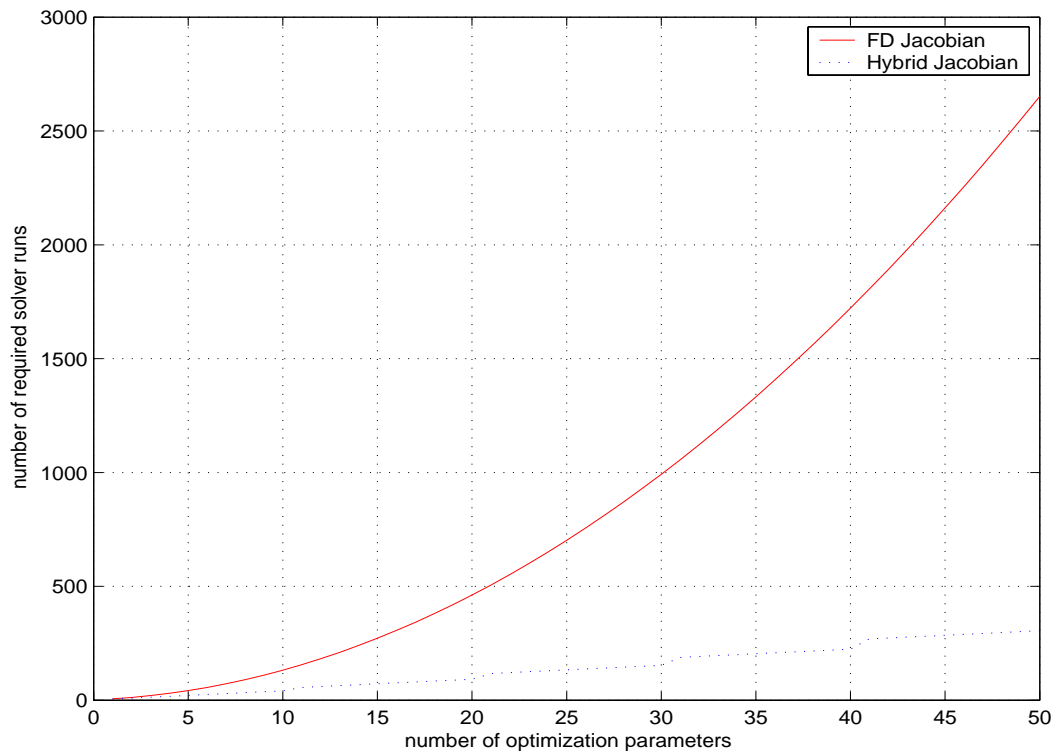


Figure 3.6: Number of required FDTD solver runs using the full finite difference Jacobian or the hybrid Jacobian approximation

3.2.3 Step Acceptance and Line Search

The Gauss-Newton algorithm above will give fast convergence with a minimum number of function evaluations if the current iterate is close to the minimizer but is not guaranteed to converge from arbitrary starting points. To obtain a globally convergent version of the Gauss-Newton algorithm, the outer iteration is combined with a line search. The step in the object is multiplied with a suitable factor λ . This gives the damped Gauss-Newton method which is globally convergent.

$$x_{k+1} = x_k - \lambda_k \left(J(x_k)^T J(x_k) \right)^{-1} J(x_k)^T F(x_k). \quad (3.59)$$

As the full step according to (3.41) will always be tried first this strategy is also referred to as backtracking. The corresponding unconstrained minimization problem (3.29) is used to derive the algorithm. After the calculation of the full Gauss-Newton step s according to (3.42) the function value at the new iterate $x_{k+1} = x_k + s$ is evaluated. The decision whether to accept the step s is based on the Armijo rule [64]. It is used here in the form

$$f(x_k + \lambda s) < f(x_k) + \alpha \lambda \nabla f(x_k)^T s. \quad (3.60)$$

It requires that the average decrease in function value is at least a portion α of the initial function decrease in the descent direction at x_k . This rule effectively avoids taking too large steps. If the initial rate of decrease at the current iterate is large and a step is taken in this direction resulting in a minor decrease of function value the step was too large. For the test of the full Gauss-Newton step λ is set to unity. The value of α is chosen quite small to accept all steps which lead to an acceptable decrease in function value. When the current step is not acceptable the information gained by evaluating the function at x_{k+1} can be used to calculate a good choice for the step length factor λ . The function to minimize is given by (3.30). This function is modelled in one dimension by a line through x_k in the search direction $p_k = s$ given by (3.42).

$$\hat{f}(\lambda) = f(x_k + \lambda p_k) \quad (3.61)$$

The value of this function in λ at $\lambda = 0$ is known as this is the function value at the current point.

$$\hat{f}(\lambda = 0) = f(x_k) \quad (3.62)$$

The slope of the function is

$$\hat{f}'(\lambda = 0) = \nabla f(x_k) p_k \quad (3.63)$$

which is also known as the gradient of the function can be calculated from the Jacobian at the current iteration and the function values $\nabla f(x_k) = F(x_k)^T J(x_k)$. The third piece of information is the value of the function at the full step, as this is the function value for the full Gauss-Newton step which has already been evaluated in order to decide whether a line search is necessary or not.

$$\hat{f}(\lambda = 1) = f(x_k + p_k) \quad (3.64)$$

From these three pieces of information it is possible to set up a quadratic model $m = a\lambda^2 + b\lambda + c$ for (3.61). The coefficients of this model are calculated from (3.62), (3.63) and (3.64). This gives

$$m = (f(x_k + p_k) - \nabla f(x_k)p_k - f(x_k)) \lambda^2 + \nabla f(x_k)p_k \lambda + f(x_k) \quad (3.65)$$

The minimum of that function is at

$$\lambda_{min} = \frac{-\nabla f(x_k)p_k}{2(f(x_k + p_k) - \nabla f(x_k)p_k - f(x_k))}. \quad (3.66)$$

From the information about the function the minimum is expected to be at this point for λ . This must be verified again by a function evaluation for the new value of $x_{k+1} = x_k + \lambda_{min}p_k$. If $f(x_{k+1})$ is sufficiently decreased according to (3.60) the new iterate is accepted and the next iteration will start. If that step is again unsatisfactory many strategies for global convergence of Newton type methods use this point to establish a cubic model of the function f and select a new λ to minimize that model. Because of the very high cost of function evaluations this is omitted here. The iteration is stopped because it is very unlikely that the calculated direction is leading to a successful step if it cannot be modelled by a quadratic model. Therefore the next iteration incorporating new parameters for the optimization is started. This approach is very successful when tested computationally and avoids wasting function evaluations on the line search which will at most lead to very small improvements of the iterate.

The object representation by its material parameters and the measurement data are both complex quantities. These are transformed to real valued ones by treating real and imaginary parts as separate quantities which doubles the number of parameters and equations. The representation in the real/imaginary part format is favored over the magnitude/phase format because the problem is scaled much better. The scattering parameter representation is very well suited as $0 \leq |S| \leq 1$. Scaling problems can so completely be avoided.

The regularization scheme and the iterative algorithm developed in this chapter provide a very efficient and easy to use method for solving inverse electromagnetic problems. The regularization allows the estimation of the achievable resolution prior to the imaging process and avoids the uncertainties of selecting a suitable regularization parameter. The regularized problem can be formulated as a simple unconstrained nonlinear least-squares problem without penalty functions and regularization parameters. Additionally the object parameters can be related to certain subsets of the data which gives better convergence to the solution regardless of non-uniqueness. The iterative algorithm is aimed on minimizing the number of very expensive function evaluations. The performance of these concepts is assessed on one-dimensional and three-dimensional imaging problems in the following.

Chapter 4

Reconstruction of Lossy One-Dimensional Permittivity Profiles

4.1 Imaging System Design

4.1.1 Measuring System

The application of the regularization and iterative algorithm to the one-dimensional layered media problem is straightforward from the numerical point of view. The looked for material parameters are expanded according to equation (3.21). The simulation examples and measurements are solved either for the complex permittivity $\varepsilon'_r - j\varepsilon''_r$ or ε'_r and the conductivity σ . The regularization and iterative scheme employed are as described in the previous chapter. The direct problem is solved using integration of the Ricatti equation (2.1) along the object. However, the imaging system requires a special measuring set-up which is shown in figure 4.1.

The inhomogeneous material under test (MUT) to image is placed in a waveguide section. The MUT is assumed to be homogenous in the transverse plane. The scattering parameters of the waveguide section of known length loaded with the MUT are measured using a vector network analyzer. Standard rectangular waveguide operating in the fundamental TE_{10} mode [6] is used for the measurements. Ultra-wideband measurements are possible using coaxial lines. Especially 7 mm airlines are well suited for the task [71] with the drawbacks of being fragile and requiring samples fitting the transverse dimensions of the coaxial line exactly. Special coaxial to waveguide transitions are needed for the waveguide measurements. This is because it is necessary to acquire low frequency information about the object. As shown in figure 3.5 the lower order expansion coefficients will have the greatest impact on the measured scattering parameters in the low frequency range. This low frequency range information can not be measured using standard set-ups due to the different cutoff frequencies in the measuring system and in the object loaded

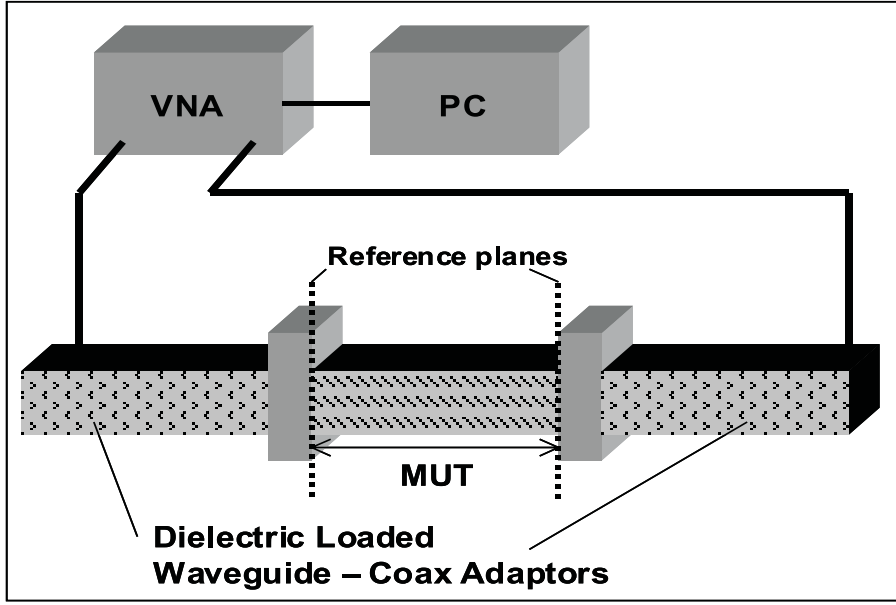


Figure 4.1: Measuring set-up for the one-dimensional layered media reconstruction

section. The propagation constant in air filled rectangular waveguide is

$$\beta = \sqrt{k_0^2 - k_c^2}. \quad (4.1)$$

The cutoff wavenumber of the dominant TE_{10} mode is $k_c = \frac{\pi}{a}$ for an waveguide with dimensions *width* = a , *height* = b , $a > b$. The average propagation constant in the dielectrically loaded waveguide section is

$$\bar{\beta} = \sqrt{\bar{\epsilon}_r k_0^2 - k_c^2} \quad (4.2)$$

where $\bar{\epsilon}_r$ is the average relative permittivity in the object under test. Because of the material with $\epsilon > \epsilon_0$ the wavenumber k'_c at which the fundamental TE_{10} mode starts propagating is lower in the section loaded with the object.

$$k'_c = \frac{kc}{\sqrt{\bar{\epsilon}_r}} \quad (4.3)$$

The average effective permittivity $\bar{\epsilon}_r$ is defined by the equality

$$\sqrt{\bar{\epsilon}_r k_0^2 - k_c^2} = \frac{1}{L} \int_{z=0}^L \sqrt{\epsilon_r(z) k_0^2 - k_c^2} dz. \quad (4.4)$$

The inequality between average effective permittivity and the average permittivity can be shown using (4.4).

$$\bar{\epsilon}_r = \frac{1}{k_0^2} \left(\left(\frac{1}{L} \int_{z=0}^L \sqrt{\epsilon_r(z) k_0^2 - k_c^2} dz \right)^2 + k_c^2 \right) \neq \frac{1}{L} \int_{z=0}^L \epsilon_r(z) dz \quad (4.5)$$

To obtain a stable solution of the inverse problem low frequency measurements of the object are required. The different cutoff frequencies do not allow low frequency measurements. For the measurement of high average permittivity objects dielectrically loaded waveguide to coaxial transitions are needed. Using such transitions the propagation constant in the feeding lines can be adjusted to be approximately the same as in the object. Experimental work shows that only objects having an average relative permittivity up to $\epsilon_r < 2$ can be reliably imaged using standard air filled transitions. Waveguide to coaxial transitions having lower cutoff are designed for measuring objects with higher permittivity. The use of dielectrically loaded waveguide to coax transitions has the additional benefit of achieving a matching effect. By this the sensitivity of high permittivity object measurements can be improved as the high surface reflection is lowered.

4.1.2 Design of Dielectrically Loaded Waveguide to Coax Transitions

As dielectrically loaded waveguide to coaxial transitions are not available as standard components a set of such transitions was designed and manufactured. The fill permittivities used are ranging from $\epsilon_r = 2$ to $\epsilon_r = 15$. The main design goal is to achieve a good input match over the whole waveguide band. As the waveguide to coaxial transitions are absorbed into the error boxes in the calibration procedure an input match of -15 dB is considered to be sufficient. This will assure that a sufficiently large portion of the signal is actually transmitted to the object and enable good accuracy measurements using a calibrated VNA. The waveguide band is shifted downwards according to (4.3). For a WR 90 standard rectangular waveguide the band given by the monomode condition is 6.56 GHz to 13.11 GHz. Using adaptors having a relative permittivity of $\epsilon_r = 4$ measurements in WR 90 waveguide can now be carried out in the frequency range from 3.28 GHz to 6.56 GHz.

The absolute bandwidth is decreasing with higher filling permittivity. High permittivity objects must be measured using several adaptors and combining the measurements in order to achieve high resolution images. The design chosen for the adaptors is given in figure 4.2. The adaptors use a tapered ridge to achieve the desired bandwidth. The center conductor of a female SMA connector holds a metallic disc which also enables large bandwidth. The whole inner space is filled with low-loss dielectrics having the desired permittivity [72]. By optimizing this design a very good input match can be achieved when simulating the adaptors. The measured reflection of the device is not as good as shown in figure 4.3. Here the results for an adaptor filled with a low loss dielectric having a permittivity of $\epsilon_r = 3.82$ are shown. Manufacturing tolerances and dielectric loss not considered in the design are identified as the sources for the deviations. This can be verified by remeasuring the geometry of the manufactured components and adapting the measures for the simulation which leads to a very good agreement between measurement and simulation.

Although the measured performance of the adaptors is not as good as expected from simulations it is still sufficient to allow for accurate measurements as the errors

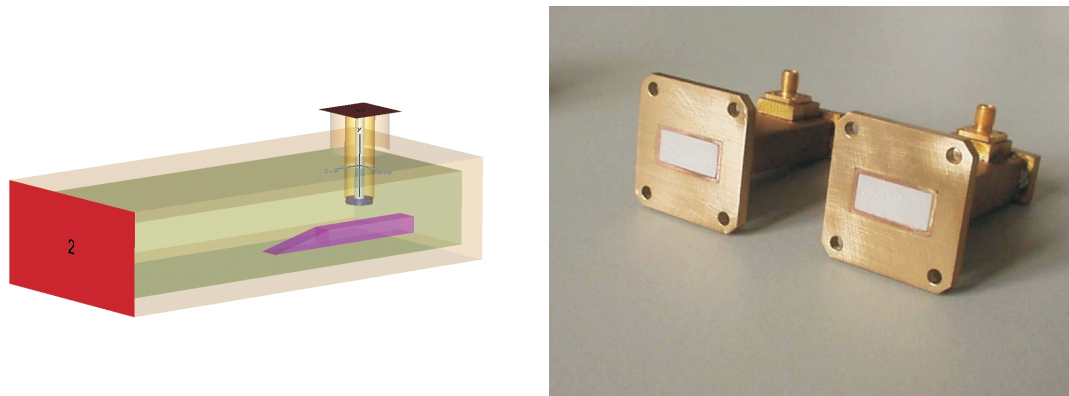


Figure 4.2: Model and photo of the dielectrically loaded waveguide to coax transition

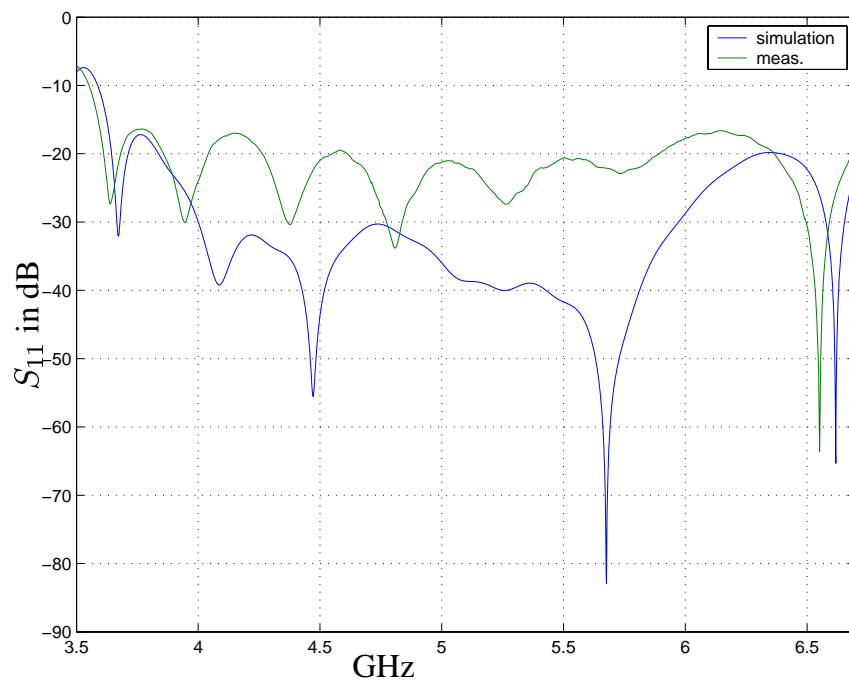


Figure 4.3: Simulated and measured input match for a dielectrically loaded waveguide to coax transition

introduced by the adaptors can be removed using error correction [73]. The concept of dielectrically loaded waveguide components can also be used for the evaluation of homogenous materials over wide frequency bands. Only one material sample needs to be machined to fit exactly the transverse waveguide dimensions and can then be measured using waveguides having the same dimensions but different fill permittivities.

4.1.3 Design of Dielectrically Loaded TRL Calibration Kits

When measuring the scattering matrix of a loaded waveguide section using the dielectrically loaded transitions the VNA must be calibrated accordingly. The impedance of the filled waveguide is the system reference impedance in this case. For a two-port calibration the Trough-Open-Short-Match (TOSM) calibration or the Through-Reflect-Line (TRL) calibration methods are widely used. While both methods are in principle applicable for full two-port error correction the TRL method has the considerable advantage of not requiring a match. This is important here as a dielectrically loaded match would need a high aspect ratio wedge or pyramid consisting of absorber. Additionally the negative shape of that absorber must be machined in the low loss dielectric which is extremely difficult to manufacture. The TRL method is therefore favored for the calibration in dielectrically loaded waveguide. It only requires a highly reflective device where a standard waveguide flush short can be used. The through connection is simply the connection of the waveguide to coax transitions face to face and the line standard consists of two homogeneously filled sections of transmission line.

The minimum requirement for the line standards is to fulfil the phase condition $30^\circ < \varphi < 150^\circ$. It is important to obey this condition in order to avoid that the measurements of the line standard are linearly dependent on the ones of the through standard. In that case the resulting linear system for the error terms would be badly conditioned and unnecessary errors in the calculation of the error terms will occur. If only one line standard was used this phase condition would still be fulfilled for a standard waveguide band. However, two standards are used to achieve the maximum accuracy possible.

The optimum phase for the line standard is $\varphi = 90^\circ$ which will give the most accurate calibration. The optimum calibration kit therefore has a minimum deviation θ from 90° . The through standard is a line of length L_0 , although its length is chosen to be zero whenever possible. This leads to conditions

$$\beta_1 L_1 - \beta_1 L_0 = \frac{\pi}{2} - \theta \quad (4.6)$$

$$\beta_2 L_1 - \beta_2 L_0 = \frac{\pi}{2} + \theta \quad (4.7)$$

$$\beta_2 L_2 - \beta_2 L_0 = \frac{\pi}{2} - \theta \quad (4.8)$$

$$\beta_3 L_2 - \beta_3 L_0 = \frac{\pi}{2} + \theta \quad (4.9)$$

where L_1 and L_2 are the lengths of the line standards and β_1 and β_3 are the propagation constants at the lower and upper waveguide band limit. The propagation

waveguide	line 1	line 2	f start	f cross	f stop	Θ
WR90	12.3 mm	8.4 mm	8.2 GHz	9.8 GHz	12.5 GHz	17.1°
WR62	8.5 mm	5.8 mm	11.9 GHz	14.1 GHz	18.0 GHz	16.8°
WR42	5.7 mm	3.9 mm	17.6 GHz	20.9 GHz	26.7 GHz	16.9°
WR28	3.8 mm	2.6 mm	26.4 GHz	31.4 GHz	40.1 GHz	17.0°

Table 4.1: Optimum line lengths for waveguide TRL calibration kits

constant at the crossover frequency from the long line standard to the short one is β_2 . The ratio of the line lengths can be calculated from (4.6)-(4.9).

$$\frac{L_1 - L_0}{L_2 - L_0} = \frac{\frac{\pi}{2} + \theta}{\frac{\pi}{2} - \theta} = \sqrt{\frac{\beta_3}{\beta_1}} \quad (4.10)$$

This can be used to calculate the deviation angle.

$$\theta = \frac{\pi \sqrt{\frac{\beta_3}{\beta_1}} - 1}{2 \sqrt{\frac{\beta_3}{\beta_1}} + 1} \quad (4.11)$$

Using this angle in the starting conditions (4.6) and (4.9) yields the lengths for the line standards.

$$L_1 = \frac{\frac{\pi}{2} - \theta}{\beta_1} + L_0 \quad (4.12)$$

$$L_2 = \frac{\frac{\pi}{2} + \theta}{\beta_3} + L_0 \quad (4.13)$$

The crossover frequency is given by (4.7) and (4.8).

$$\beta_2 = \frac{\frac{\pi}{2} + \theta}{L_1 - L_0} = \frac{\frac{\pi}{2} - \theta}{L_2 - L_0} \quad (4.14)$$

As the frequency range is scaled accordingly to the permittivity the optimum lengths are independent of the fill permittivity. The crossover frequency for the transition from the long line standard to the short one as well as the band limits are given for air filled waveguide and $L_0 = 0$ in table 4.1. These frequencies must be scaled with the square root of the permittivity. The optimum calibration kits described here can also be used for air filled standard waveguide and will give the best possible accuracy as they represent the optimum design for a fixed number of line standards. The design procedure can also be used for coaxial calibration kits. For very broadband calibration kits more than two lines might be required.

4.2 Experimental Results

4.2.1 Noise Sensitivity

One of the undesired properties of inverse problems is the noise sensitivity. Small deviations in the measured data can lead to huge deviations in the calculated object.

The desired behavior is to avoid noise amplification, instability and divergence. A stable algorithm should yield a noisy image with comparable signal to noise ratio as in the input data and must not diverge. The regularization and the corresponding iterative scheme must therefore be examined regarding their noise behavior. This is done on the example of a step function shown as true permittivity profile. The step in the real part is from $\varepsilon'_r = 4$ to $\varepsilon'_r = 6$. The step in the imaginary part is from $\varepsilon''_r = 0$ to $\varepsilon''_r = 0.5$. The object is reconstructed using simulated noiseless data, data corrupted by white additive uniformly distributed noise giving a signal to noise ratio of 40 dB and 20 dB in the worst case. A signal to noise ratio of only 20 dB exceeds the noise level to be expected in a properly calibrated scattering parameter measurement by far. The results plotted over the number of iteration steps are given in figure 4.4. The iteration starts at the back of the figures with the result of the determination of the average permittivity. The final result is the reconstructed profile for the maximum number of 15 coefficients.

For the case of noiseless input data the solution found is the best possible for the number of coefficients and is equal to the result one obtains by expanding the object into a cosine series directly. For the reconstruction affected by noise the convergence to the searched solution is retained. Oscillations are introduced on the object because higher order expansion coefficients are determined incorrectly because of the noisy input data. This convergence type is called semi-convergence [64]. Due to the frequency separation effect only the higher order coefficients are affected. The effect of noise is stronger on the imaginary part of the permittivity than it is on the real part. The absolute contrast in the dielectric loss is much smaller. Its contribution to the reflection is small compared to the contrast in the real part. Therefore it is distorted much stronger from the noise in the input data. The insertion loss of the MUT is influenced stronger by the loss. However, it is difficult to localize the loss as only the integrated loss through the whole object is influencing the measurements.

The remarkable result of this study is that the noise introduced on the scattering data does not lead to stability problems or to physically unacceptable solutions. The noise does not even affect the accuracy of the lower order expansion coefficients much. In figure 4.4 the results are virtually the same up to the 10th iteration. Only the higher order expansion coefficients are affected by the noise. This is in agreement with information theory as noise does always limit the achievable resolution of the system. Figure 4.5 shows the errors introduced on the expansion coefficients depending on the input data noise level.

The error of the calculated expansion coefficients is increasing with rising order of the coefficient. The errors for the noiseless case and the 40 dB SNR case are negligible. The error increases drastically for the 20 dB SNR case. This emphasizes that good measuring accuracy is the key to low distortion images. The setup developed in the previous section provides the possibility for accurate measurements. No problems when reconstructing images from actual measuring data are therefore expected. However the algorithm is still semi-convergent on noisy input data. It will always give the best possible result for a certain quality of the input data. Noise amplification will only take place if it is attempted to increase the resolution over the

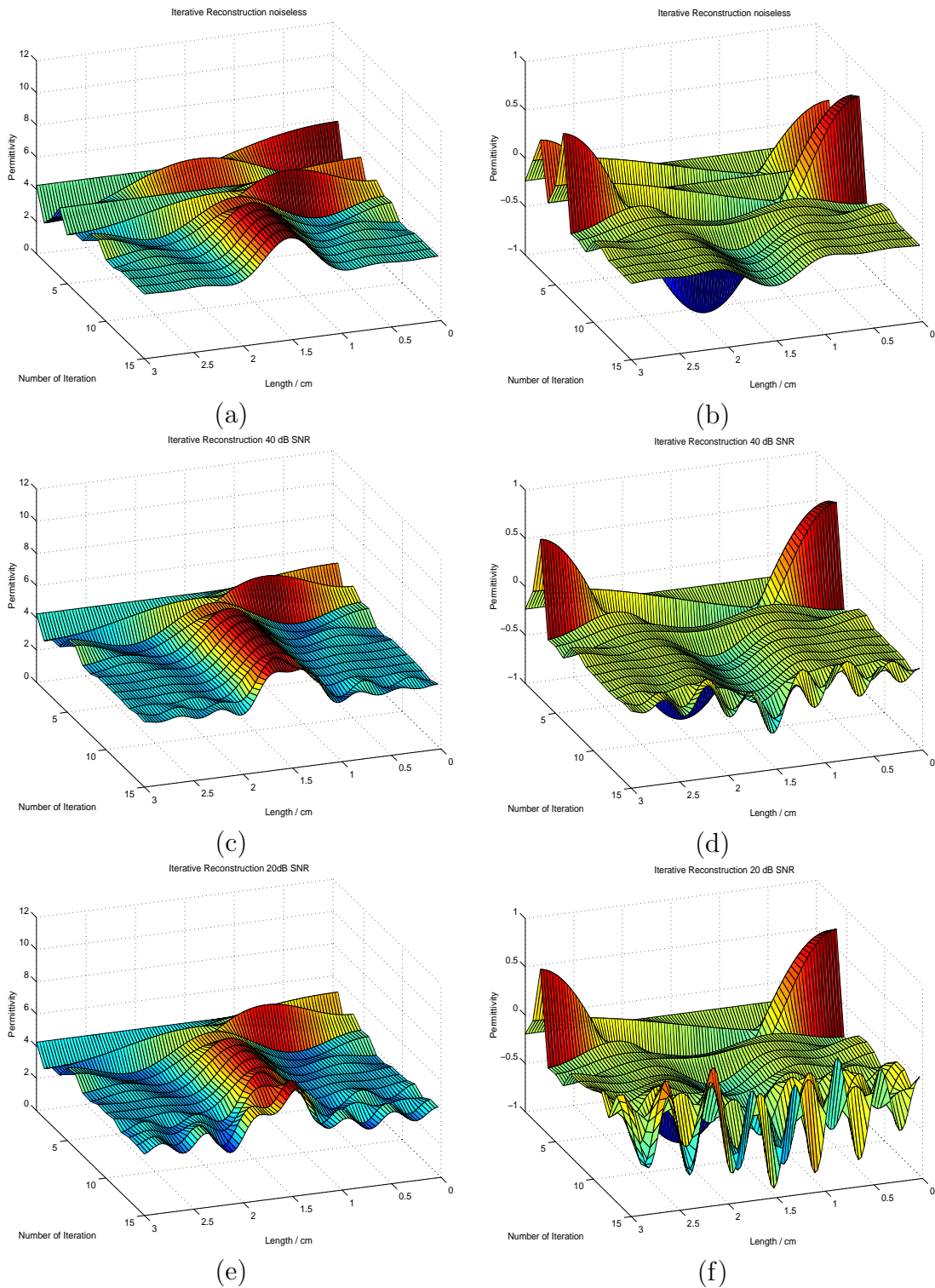


Figure 4.4: Effect of the input data SNR on the reconstructed objects: Real (a) and imaginary (b) part of reconstructed permittivity using noiseless data, real (c) and imaginary (d) part of reconstructed permittivity using data with 40 dB SNR, real (e) and imaginary (f) part of reconstructed permittivity using data with 20 dB SNR.

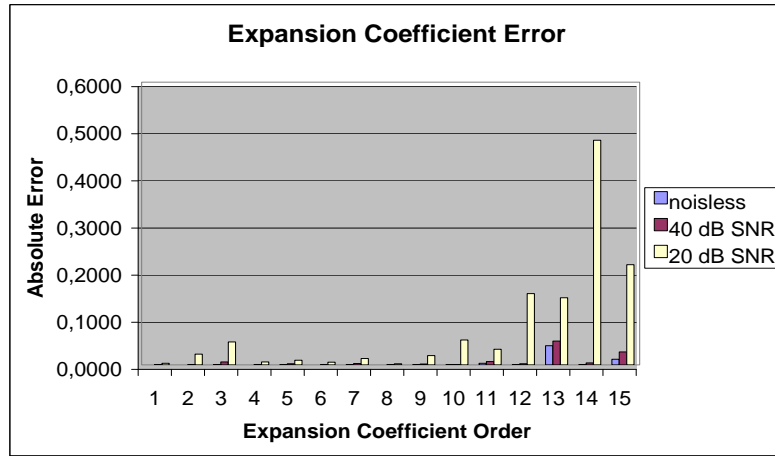


Figure 4.5: Effect of input data noise level on calculated expansion coefficients

limit given by the measuring accuracy. Compared to iterative regularization schemes depending on regularization parameters the method does not require to repeat the whole imaging process. The iteration steps introducing the noise amplification may simply be removed a-posteriori.

The effect of noise in an expansion into an orthogonal set can be limited by weighting the coefficients depending on their expected accuracy [74]. From the fact that the higher order coefficients are more likely to be affected by noise than are the lower order ones, the higher order coefficients are windowed by a suitable window function. The functions

$$w1 = \begin{cases} 1 & n = 0 \dots \frac{N}{2} \\ \cos\left(\frac{2n-N}{N} \cdot \frac{\pi}{2}\right) & n = \frac{N}{2} \dots N \end{cases} \quad (4.15)$$

and

$$w2 = \begin{cases} 1 & n = 0 \dots \frac{N}{2} \\ \cos^2\left(\frac{2n-N}{N} \cdot \frac{\pi}{2}\right) & n = \frac{N}{2} \dots N \end{cases} \quad (4.16)$$

were tested. Figure 4.6 compares the RMS permittivity errors for the case of the reconstruction of the step object from the 20 dB SNR data set. The results for different numbers of expansion coefficients and using weighting functions according to equations (4.15) and (4.16) are compared. From the results obtained for different numbers of expansion coefficients ranging from 10 to 15 the result using 10 coefficients only is most accurate. The higher order coefficients are affected strongly by noise and are distorting the reconstructed profile by causing oscillations. The results obtained using the weighting functions on the result obtained after 15 iterations show that the \cos^2 -function gives best results in terms of the RMS error in the imaged permittivity. The weighting functions are plotted in Figure 4.7.

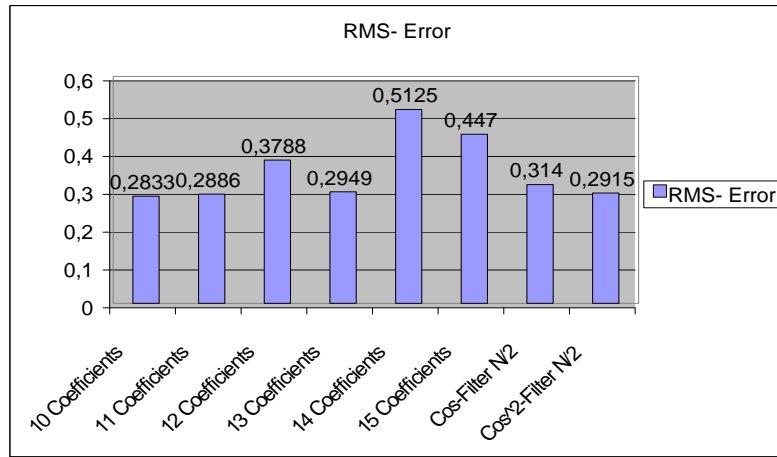


Figure 4.6: RMS permittivity error for different numbers of expansion coefficients and weighting functions

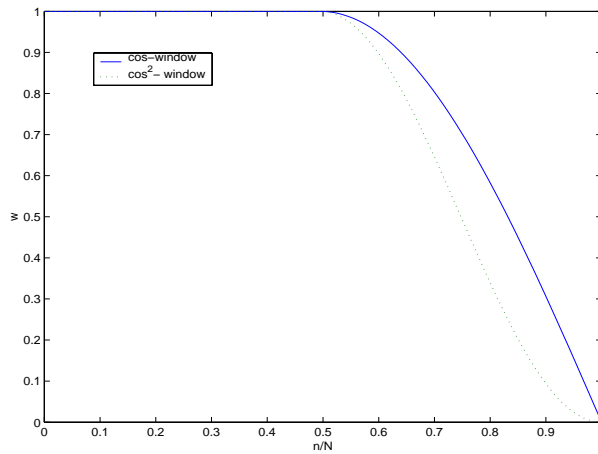


Figure 4.7: Weighting functions for expansion coefficients

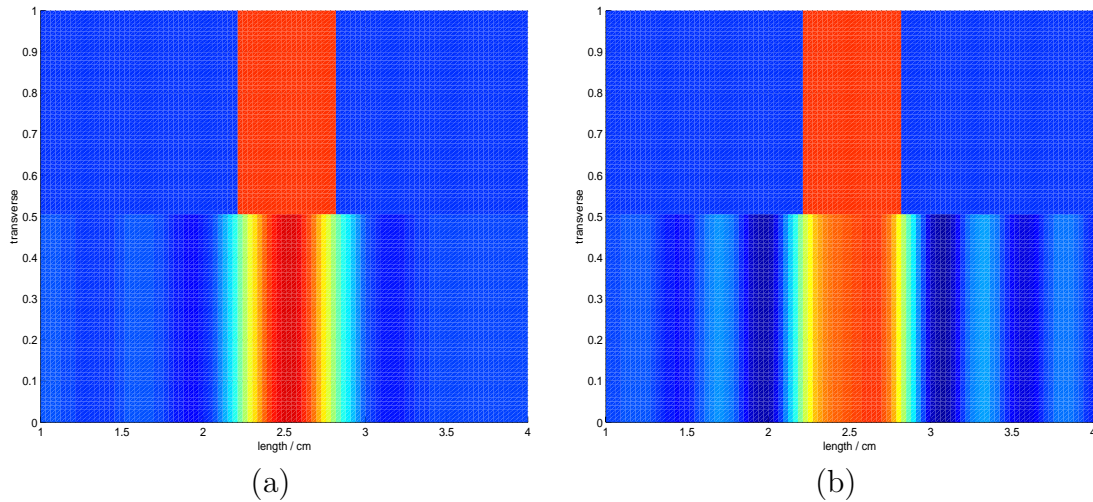


Figure 4.8: Reconstruction results for 10 expansion coefficients (a) and 13 expansion coefficients (b)(right). The actual object is shown in the upper half for comparison.

Figure 4.8 emphasizes that it is difficult to judge an image by its RMS error compared to the actual object. The results of the previous example are plotted in two dimensions. The upper half of both images shows the actual object for comparison. Although the 10 expansion coefficients profile gives the lowest RMS error it appears to have lower resolution to the human viewer. Also the actual size of the object cannot be extracted as accurately as from the image obtained from 13 coefficients. As a consequence image processing and filtering should not be included in the standard image acquisition procedure. Image processing and enhancement techniques can be applied later to the raw image data when a specific task is to be fulfilled by the imaging system. The performance can then be measured effectively on task performance [75].

4.2.2 Feasibility of Tumor detection

One of the applications microwave imaging is most promising for is tumor detection in mass screening [59], [60], [10], [58], [12] and [11]. Here the X-ray based methods work unreliable because of the low soft tissue contrast. The reason for the high potential of microwave based detection is the high dielectric contrast encountered in this application. This high contrast is also the reason why methods obtained using weak scattering assumptions fail. To show the applicability of the suggested method in this field simulations of human tissue were carried out. As an example a tumor in fat tissue has been considered. According to [10] the permittivities in the measurement frequency range are approximately $\epsilon_r = 9 - j4$ for the fat tissue and $\epsilon_r = 50 - j45$ for the tumor region. The permittivity is assumed to be frequency independent and is replaced by its mean value in the measurement band. To the best of the authors knowledge, such a permittivity distribution is not accessible for quantitative reconstruction with any known microwave imaging method. The

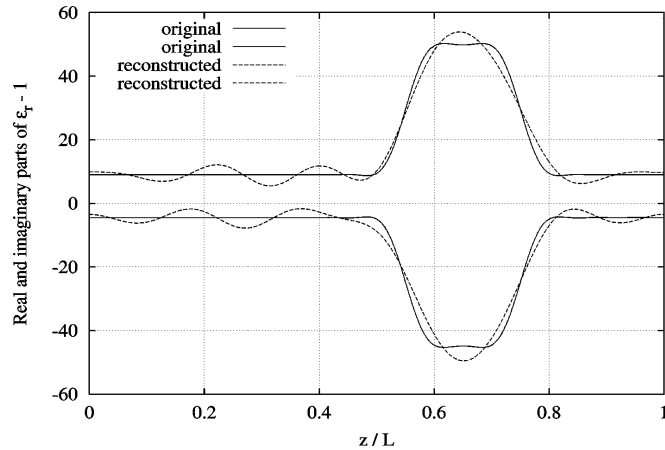


Figure 4.9: Images (real and imaginary part of the permittivity) of a tumor phantom embedded in fat tissue

result obtained using the successively relaxed smoothness constrained is given in figure 4.9. From the simulated noiseless measuring data 16 expansion coefficients were calculated. The result is a bandlimited image of the original profile. This shows that the method can quantitatively image objects showing a dielectric contrast $c = (\varepsilon_{max} - \varepsilon_{min})/\varepsilon_{min}$ of more than 450% in the real and 1000% in the imaginary part of the permittivity. Microwave imaging applications in the medical field using the proposed algorithm appear to be feasible according to this experiment.

4.2.3 Measuring Results

The measurements were carried out on a Agilent 8722D VNA. This instrument is not capable of a full TRL calibration. Because it does not use a fourth receiver a TRL* calibration [2] is used instead. The error model assumes symmetry of some elements of the error boxes. These symmetry assumptions are not exactly fulfilled by the physical set-up. This leads to increased measuring errors especially when measuring highly reflective devices but is a good test for the robustness of the imaging algorithm. All measurements are carried out in WR-90 waveguide using standard and dielectrically loaded waveguide to coax transitions and TRL calibration kits. The first object reconstructed consists of two layers. The first is acrylic with a permittivity of $\varepsilon_r = 2.54$ and the second layer is just air. Because the average permittivity is low it can be imaged using standard waveguide to coaxial transitions and a full two-port error correction using the through open short match (TOSM) method. This gives very accurate scattering parameter measurements indistinguishable from simulation data. The reconstruction was carried out successfully using 7 and 10 expansion coefficients. The attempt to calculate more than 10 expansion coefficients from the measuring frequency band leads to instability. Using equation (3.23) the maximum number of expansion coefficients that can be calculated from the frequency range can be estimated. The measuring frequency band is from

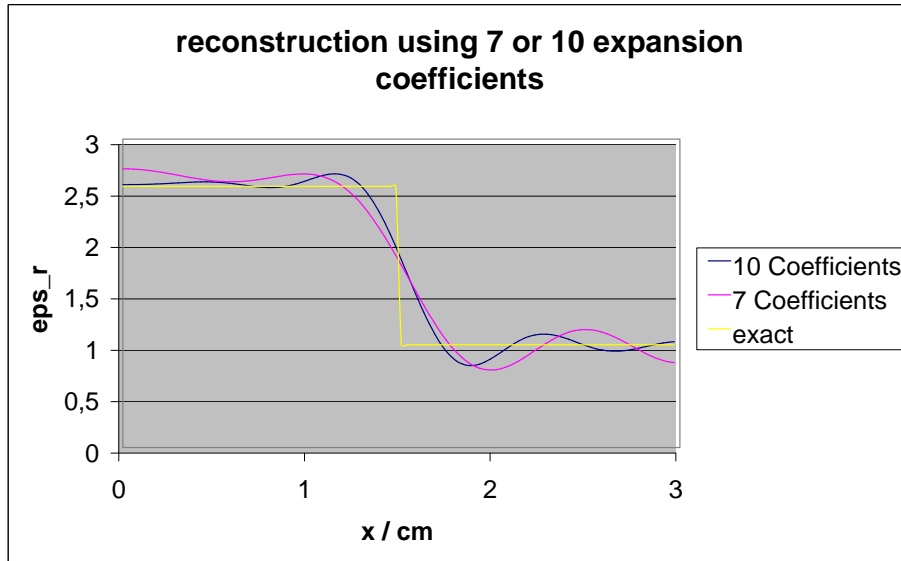


Figure 4.10: Reconstruction of acrylic / air object

7.5 GHz to 13 GHz. The average effective permittivity in the object is according to (4.4) $\bar{\varepsilon}'_r = 1.66$. The maximum propagation constant in the measuring frequency range is $\beta_{max} = \sqrt{\bar{\varepsilon}'_r k_{0max}^2 - k_c^2}$. Using this in (3.23) yields the maximum number of coefficients

$$N_{max} = \frac{2\beta_{max}c}{\pi} \quad (4.17)$$

where c is the length of the object section. For the acrylic / air object this gives a number of 6 expansion coefficients from the measuring frequency range. The value of 10 found by evaluating the measurements using different settings exceeds the number anticipated from (4.17) by far. This is expected as for calculating an optimization parameter is not necessary that the frequency of maximum effect is within the measuring frequency band. It is sufficient if the optimization parameter has an effect that is measurable. The effect of each parameter on the frequency domain measuring data has the sinc-function shape depicted in figure 3.5. The range of measurable effect is extending quite far over the frequency range around the point of maximum effect. The number of coefficients that can be reconstructed obtained from (4.17) is an estimate that is rather pessimistic and should frequently be exceeded for high accuracy measurements.

The next object imaged consisted of three layers. To show the applicability of the imaging system to biological tissues fat tissue of a pig is used. The permittivities of the layers used to compose the inhomogeneous object were determined using measurements of homogenous samples of the materials. These measurements were

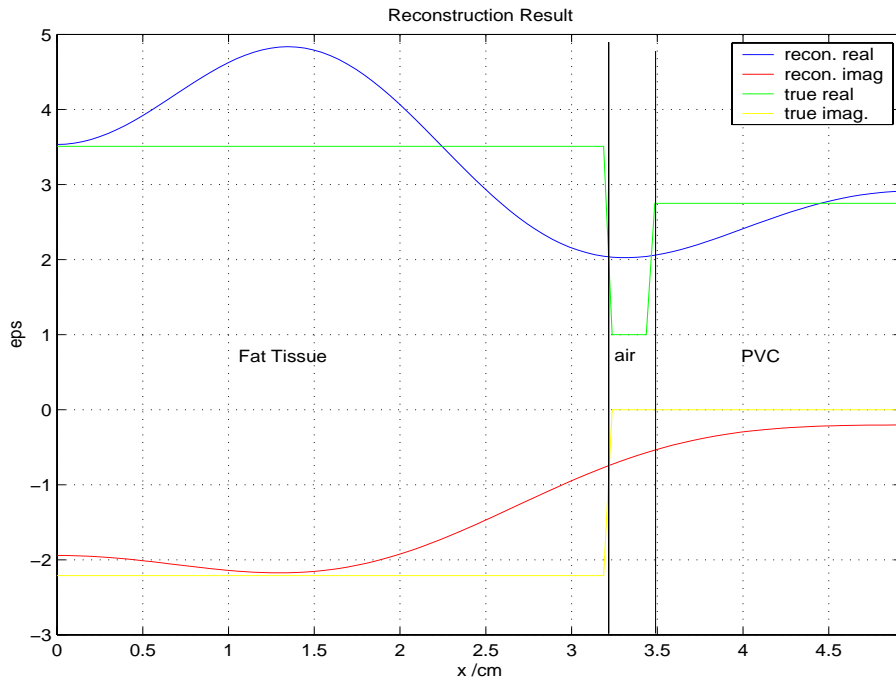


Figure 4.11: Reconstruction of an fat / air / PVC object

evaluated using a high-precision dielectric measurement software developed for that purpose [76]. The values are given as true profile in the plot for comparison. The measurement of the three layer object was carried out using adaptors filled with low loss dielectric of permittivity $\varepsilon_r = 3.82$. The measuring frequency range is from 3.5 GHz to 7 GHz. The resolution achieved is that expected from (4.17) for this example. The reason for this is the lower measuring accuracy of these measurements. Due to the TRL* calibration the measurements are noisy as shown in figure 4.12.

However, this is to our knowledge the first quantitative measurement of an inhomogeneous object consisting of biological tissue and showing such high loss and contrast. The dielectric contrast is as high as 350%. The real and imaginary part are imaged simultaneously which gives in fact two images of the object. Due to the limited resolution the air gap cannot be reconstructed accurately, but it is possible to distinguish between the lossy fat tissue and the low loss air and PVC regions. The overshoot in the real part is due to Gibbs phenomenon at the large step caused by the air gap. The reconstructed real part shows that the air gap has been detected but cannot be imaged using the given measuring accuracy and bandwidth. This emphasizes again the need for accurate broadband measurements. The measuring accuracy limitations are completely due to the VNA. Replacing it by a four receiver instrument capable of full TRL calibration the resolution can be improved as verified precisely for the acrylic / air object.

The results obtained in the simulation and measuring examples show that the algorithm developed in chapter 3 is superior to the methods observed in the state of the art in many aspects. The range of dielectric contrasts and losses allowable

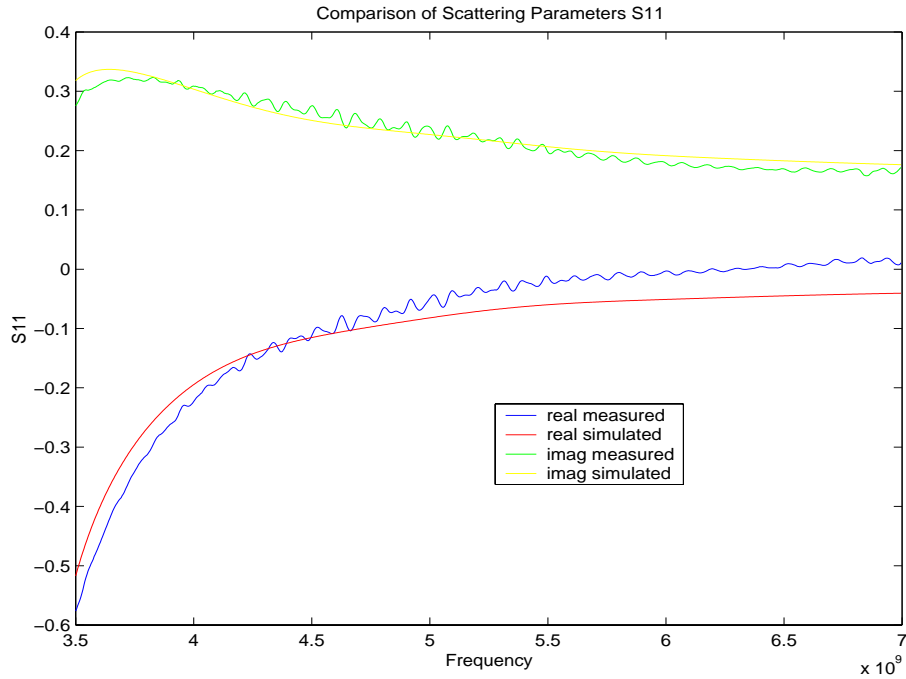


Figure 4.12: Comparison of simulated and measured reflection of the three layer object in figure 4.11: The noise on the measured plots is due to the simplified TRL* error model.

is much higher. This allows quantitative imaging of high contrast and lossy inhomogeneous objects such as biological tissues. The noise sensitivity is good. The stability of the algorithm is excellent. The amount of a priori knowledge required is very little as only a rough guess for the average permittivity in the object is needed. This initial guess can deviate up to a factor of 4 from the actual value without threatening convergence. This has been tested by starting the iterative imaging process with several initial guesses and testing for convergence. The algorithm is computationally more expensive than the profile inversions outlined in section 2.1. Because the direct problem solution can be obtained by one-dimensional integration the iterative algorithm is still very efficient. The results for the one-dimensional profile inversion show that the imaging algorithm introduced here gives considerable advantages over established methods. The concepts are therefore now applied to fully three-dimensional microwave imaging.

Chapter 5

Three-Dimensional Microwave Resonator Tomography

5.1 Microwave Resonator Tomography System

5.1.1 System Concept

The application of the space harmonics representation of the object with resulting regularization and iterative scheme has been proven very successful for the one-dimensional profile inversion. The concepts are applied to full three-dimensional imaging now. The spectral expansion uses the length of the profile section in the one-dimensional case in order to define the spatial frequencies used for the expansion. The natural extension of this concept is to place the object in a volume with known dimensions. This leads to the novel concept of microwave resonator tomography. The object is placed in a microwave cavity. The space occupied by the object is imaged for its distribution of material parameters. The use of a cavity gives several advantages. The properties of the cavity without object are known exactly. Changes in the behavior can be traced back to the object. The measuring accuracy is expected to be much better than in free space schemes. The cavity can be described by scattering parameters at its ports. These scattering parameters of the waveguide ports can be measured accurately using a VNA calibrated in the same waveguide type. This allows convenient high-accuracy measurements.

In order to obtain sufficient information to uniquely image the object the cavity is equipped with several ports. This gives the possibility for a local scanning effect by measuring the reflection at the ports in the off-resonance state. The reflection and transmission parameters, the resonance frequencies and the quality of the resonances contain information about the distribution of the material parameters throughout the entire object.

The solution of the direct problem was easily carried out for the one-dimensional profile reconstruction. For the three-dimensional case no such straightforward algorithms exist. While the main iterative algorithm may remain unchanged compared to the one-dimensional case the solution of the direct problem requires advanced techniques. The full-wave analysis of three-dimensional structures can be done by

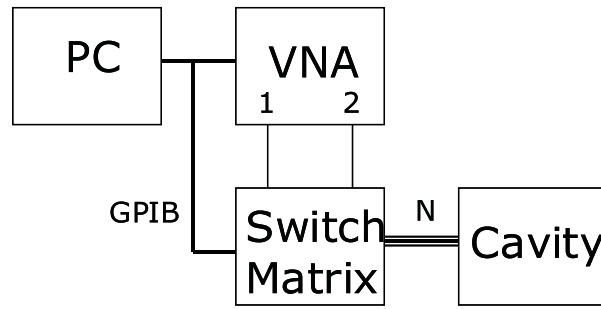


Figure 5.1: Microwave Resonator Tomography System

frequency domain analysis or the finite difference time domain method (FDTD) [69], [77], [78]. For wideband scattering parameter calculations the FDTD method is favorable because it is capable to yield the scattering parameters over the whole frequency band in just one calculation. Although FDTD is the most suitable and efficient method it still requires a considerable amount of computing power.

The cavity is equipped with a number of ports that is in the range from 6-12 for the first experimental prototypes. This would make measuring the scattering matrix an extensive task. A multi-port scattering parameter measuring system is required for fast data acquisition. A schematic of the measuring system used for the Microwave Resonator Tomography is shown in figure 5.1. The PC controls the system via the GPIB bus. The GPIB bus is used for this task as it is available in all VNA's. The switch matrix connects the ports of the multi-port resonator to the ports of the VNA. It is also connected to the GPIB bus via an interface unit. The scattering parameters of the resonator loaded with the object are measured by the VNA and transferred to the PC for the imaging process. The components of this system are described in detail below.

5.1.2 Resonator Design

The cavities designed for testing the imaging system all use a rectangular geometry. This allows ease of manufacture and good geometrical approximation by the usually rectangular FDTD mesh. For imaging of three-dimensional structures test cavities with 6 to 12 ports and measures of 6 to 10 cm are used. For imaging two-dimensional objects in form of slices flat cavities with similar sizes in the transverse plane but only 5 mm high are used. The flat cavities for the imaging of slices have the advantage that testing the capabilities of the resonator imaging system is numerically not as expensive as the three-dimensional ones.

There are three possible ways to couple microwave power from coaxial feed lines into the cavity. The first and most simple is probe coupling where the inner conductor of a coaxial feed line acts as a small antenna. The second is loop coupling where the inner conductor of a coaxial line is connected to a wall of the cavity and the coupling is done by the magnetic field. The third possibility is aperture coupling. Because this is most difficult to use and would also need additional coaxial

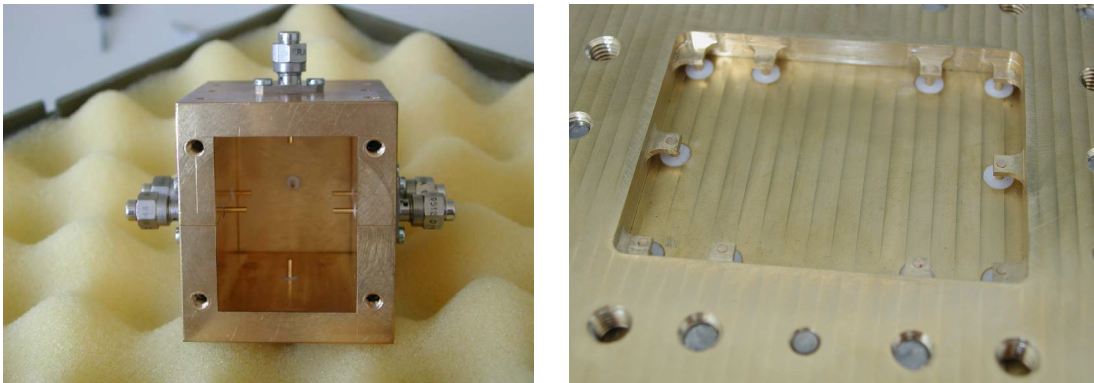


Figure 5.2: Probe-coupled 3D imaging resonator and loop-coupled 2D imaging resonator prototypes

to waveguide transitions as the feeding from the VNA is coaxial this seems not to be a beneficial solution and is therefore not further investigated. The cavities for three-dimensional imaging are probe coupled. It is difficult to use probe coupling in a flat structure when the coupling can only be done at the circumference. The resonators used for two-dimensional imaging are therefore loop-coupled. This leads to more complex coupling structures but works equally well in practice.

Once the coupling type is fixed the number and position of ports must be selected. The ports should be distributed evenly over the surface of the investigation volume. This will ensure that the resolution of the system is not strongly varying as a function of position within the cavity. The number of ports has been determined using simulation. A number of 6 to 12 ports has been found sufficient for the examples tested. When imaging objects having a high contrast and very complex structure the maximum number of ports is used. For simple objects it is not necessary to use the entire scattering matrix. The unused ports can be terminated with their characteristic impedance in that case. Termination using matched loads is preferred here because of the practical implementation of the measuring system as outlined later in section 5.1.4. Using another termination than a match would cause difficulties obtaining a well-defined termination during the measurement process because this is not done at the cavity ports directly but vi an automated switch system. Two of the resonators designed accordingly to the above considerations are shown in figure 5.2.

The resonator is operating loaded with the object over a wide frequency band typically ranging over several GHz. At a large number of frequency points a substantial part of the power will already be reflected at the coupling structure and is not going to penetrate the object itself. This occurs at all off-resonance frequencies for a high quality factor resonator. This can be beneficial because it provides the possibility of locally scanning the object as shown in figure 5.3(a). However, not much information is gained about the entire object. Using a high quality factor cavity the field distribution is concentrated locally in the vicinity of the excited port. This may lead to an image matching the material parameters close to the ports very well but is distorted in the regions close to the walls that are not directly adjacent

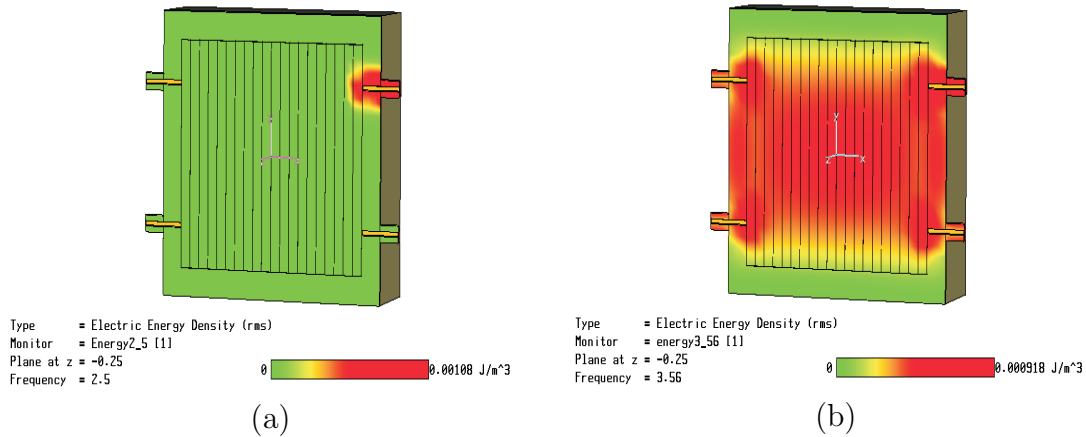


Figure 5.3: Distribution of field energy off-resonance (a) and at resonance (b)

to a port. In these regions virtually no field is present in the off-resonance mode. In addition in all high quality resonators the field is weak even in the resonance state as these regions are close to perfectly conducting walls as the top and bottom sections in figure 5.3(b).

Although the quality factor of the cavities is not very high because of the large number of coupling ports the off-resonance behavior of the cavity can be optimized by adjusting the boundary conditions at the resonator walls accordingly. The resonator walls should not be perfectly conducting as this will lead to fields essentially zero close to the walls. This results in a very uneven distribution of power with very low field energy close to the walls. As this leads to poor sensitivity for the permittivity in that region the imaged permittivity will show large errors in such regions. This can be avoided by coating the walls with a dielectric absorber. The electric fields will increase quickly from the zero at the metallic resonator wall to the inner side. Because of the loss the electric field will rise through the absorber. Obviously the best field at the object volume would be obtained by a very thick, very high dielectric constant wall coating. In that case the field at some frequencies would be in form of modes that do not have any field in the object volume but only in the wall coating. As measurements under that condition will not give any information about the object this must be avoided. Therefore a medium dielectric constant, lossy material is preferred. Losses are beneficial as the decay of the field through the layer will allow the field to assume stronger values in the regions close to the walls. Such a material will damp the resonances but gives better measuring results off-resonance. This is shown in figure 5.4. Without absorber wall coating the incident signal is fully reflected at off-resonance frequency points. With the lossy dielectric the quality factor of the resonances of the cavity is lowered so that at most frequencies the signal penetrates the cavity. In the frequency range below 4 GHz in this example no signal can be coupled into the cavity. This frequency range would not be used for imaging purposes.

The beneficial effect of a lossy wall coating is also shown by the plots in figure 5.5.

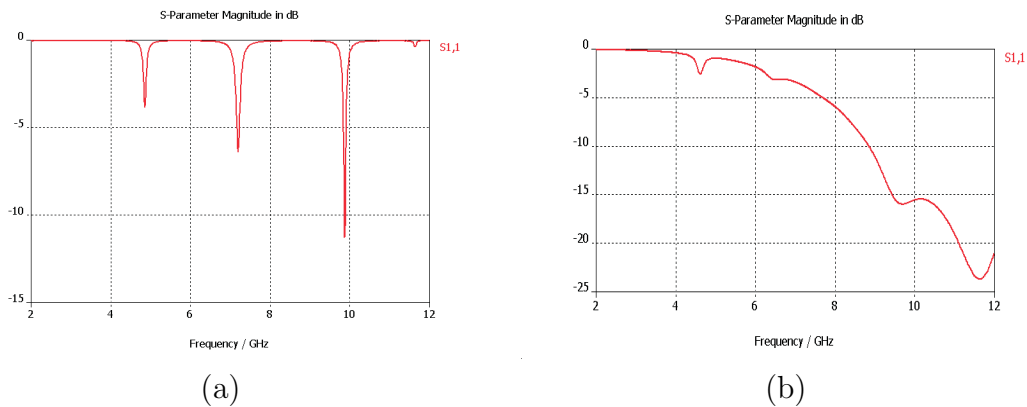


Figure 5.4: S_{11} of a cavity with no wall coating (a) and with walls coated with a lossy dielectric (b)

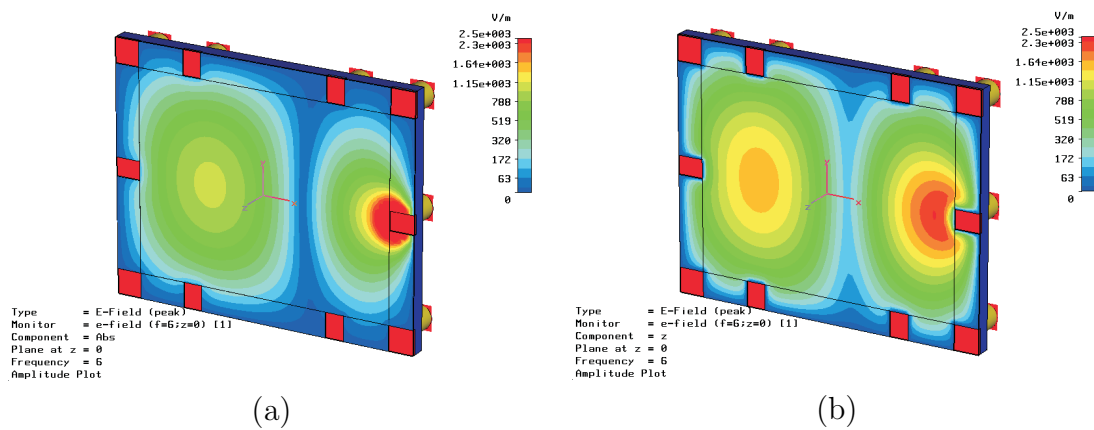


Figure 5.5: Magnitude of the electric field distribution in a cavity with no wall coating (a) and with walls coated with a lossy dielectric (b)

These present the distribution of the electric field magnitude inside the cavity. It is the same cavity as in figure 5.4 where the field has been calculated at a frequency of 6 GHz which is clearly off-resonance. Without wall coating the field is concentrated around the coupling point only. The measurements of the transmission to the other ports do not contain any information about the object. In the case with wall coating the field in the cavity is stronger and more evenly distributed throughout the cavity. Here both reflection and transmission measurements do contribute useful information to the imaging process. The excited port is radiating into the cavity similar to a free space measurement. That combination of resonator measurements and absorber chamber like measurements combines the advantages of both.

5.1.3 Absorber Materials for Resonator Wall Coating

Material Development

From the previous considerations follows that the inner walls of the cavity should be coated with an absorbing material. The permittivity of the coating must not be too large as this will lead to modes which have fields not leaving the space close to the walls. Measurements in the range of the resonance frequency of those modes will not be sensitive to the object placed in the resonator.

Commercially available absorber materials having a low to medium permittivity come in the form of absorber foams. These foams have several serious drawbacks. They are not closed cell structures so they will be very sensitive to humidity and liquids generally. The coarse cell structure of absorber foams causes inhomogeneity. While this is negligible for frequencies where the wavelength is much bigger than the cell size the inhomogeneities are influencing the scattering parameter measurements at frequencies above 10 GHz. This makes it impossible to characterize the foam exactly. As the absorbing wall coating will be part of the measuring setup it will be necessary to characterize it exactly by a complex permittivity. As this is impossible for an inhomogeneous material which also shows a great mechanical sensitivity due to its compressibility other materials must be found. A frequency dependence of the material is allowable but it should be easy to model. Available rubber based materials which have the desired mechanical properties [79] show very high permittivity $\epsilon_r > 20$ and also show strong deviations in their losses with varying frequency. These complex frequency dependence cannot be modelled by any of the common dispersion models [80].

As there are no suitable materials commercially available, it is necessary to develop a suitable material. As basis a silicone rubber casting compound was chosen. This has the advantage of high flexibility, it is weatherproof and non-sticking. It is available in a low viscosity form and can easily be casted into place. The electrical properties are also very suitable. The permittivity was measured to be nearly frequency independent in the range from 7-13 GHz at a value of $\epsilon_r = 3.02 - j0.05$. Since this loss is insufficient it must be increased by a lossy filler material. A modification of carbon is well-suited for this purpose. Carbon is used in two modifications for introducing losses in compounds. The most frequently used one is carbon black which is available in numerous different qualities each showing different properties. The carbon blacks most suitable for introducing losses in polymer substrates are highly structured conductivity rubber blacks. They were originally developed to introduce a small conductivity in compounds and rubber in order to avoid electrostatic discharge problems. These carbon blacks have highly structured particles consisting of pure carbon and having sizes of approximately 50 nm. For the purpose of introducing losses into the silicone rubber the Printex XE 2 carbon black is elected as it proved to be very well suited for similar tasks in epoxy resins [81]. The problem with rubber blacks can be that the conductivity rises very quickly from low loss states to a conductive state [82], where both are not useable for absorbing microwave power. This property of carbon blacks in epoxy resins makes epoxy resins unsuitable for the purpose of designing an absorber for the resonator wall coating.

The second available carbon modification graphite has also been examined for its behavior as a filler in silicone rubber compounds. Compared to carbon blacks graphite has a much higher permittivity (usually 12 to 15) and also higher conductivity. The structure of graphite is regular and graphite available for technical purposes has a particle size larger than $1\mu m$. The different structures lead to a completely different behavior in the compound with the silicone rubber. Graphite materials with up to 40% graphite have been tested. For the carbon black the maximum mass percentage was only 2%. The reasons for this are the low specific mass of the carbon black, so that only two percent mass result in a large volume of carbon filler. The second is the strong impact of the carbon black on the viscosity. With a content larger than 2% it is not possible to conveniently cast the absorber with the desired accuracy and material homogeneity.

For the evaluation of the electrical properties samples of all materials have been measured in a WR-90 waveguide using the transmission/reflection technique [76]. The results are given in figure 5.6. The mean values in the frequency band are given in the graphs. This shows the excellent properties of the high conductivity carbon black for introducing losses. While the real part of the relative permittivity rises approximately linear with the mass added, the losses rise very quickly. This effect occurs at and above the percolation threshold, where the carbon black particles form a weakly conductive network throughout the material. For the graphite this effect does not even occur at a content of 40% and both real and imaginary part of the permittivity depend almost linearly on the content. The material consisting of silicone rubber with 2% Printex XE2 carbon black is chosen for the resonator tomography as its properties $\varepsilon_r = 5.2 - j0.95$ at a frequency of 10 GHz are very well-suited for this application.

Material Modelling

For the use of the material it is crucial that it can be modelled easily by the FDTD solver. The selected silicone rubber with 2% carbon black shows almost frequency independent loss (figure 5.7). For modelling such a behavior the first order Debye model is most suitable. It models the frequency dependent complex permittivity by

$$\varepsilon(\omega) = \varepsilon_\infty + \frac{\varepsilon_s - \varepsilon_\infty}{1 + j\omega\tau}, \quad (5.1)$$

where ε_s is the static relative dielectric constant ε_∞ is infinite relative dielectric constant, and τ is the relaxation time constant. The maximum loss occurs at the relaxation frequency $\omega_r = \frac{1}{\tau}$. Around this frequency the loss is least frequency dependent. The relaxation constant is therefore chosen to be the center frequency ω_c of the band in which the constant loss material is to be modelled.

$$\tau = \frac{1}{\omega_c} \quad (5.2)$$

Separating real and imaginary parts of (5.1) yields

$$\varepsilon' = \varepsilon_\infty + \frac{\varepsilon_s - \varepsilon_\infty}{1 + \omega^2\tau^2} \quad (5.3)$$

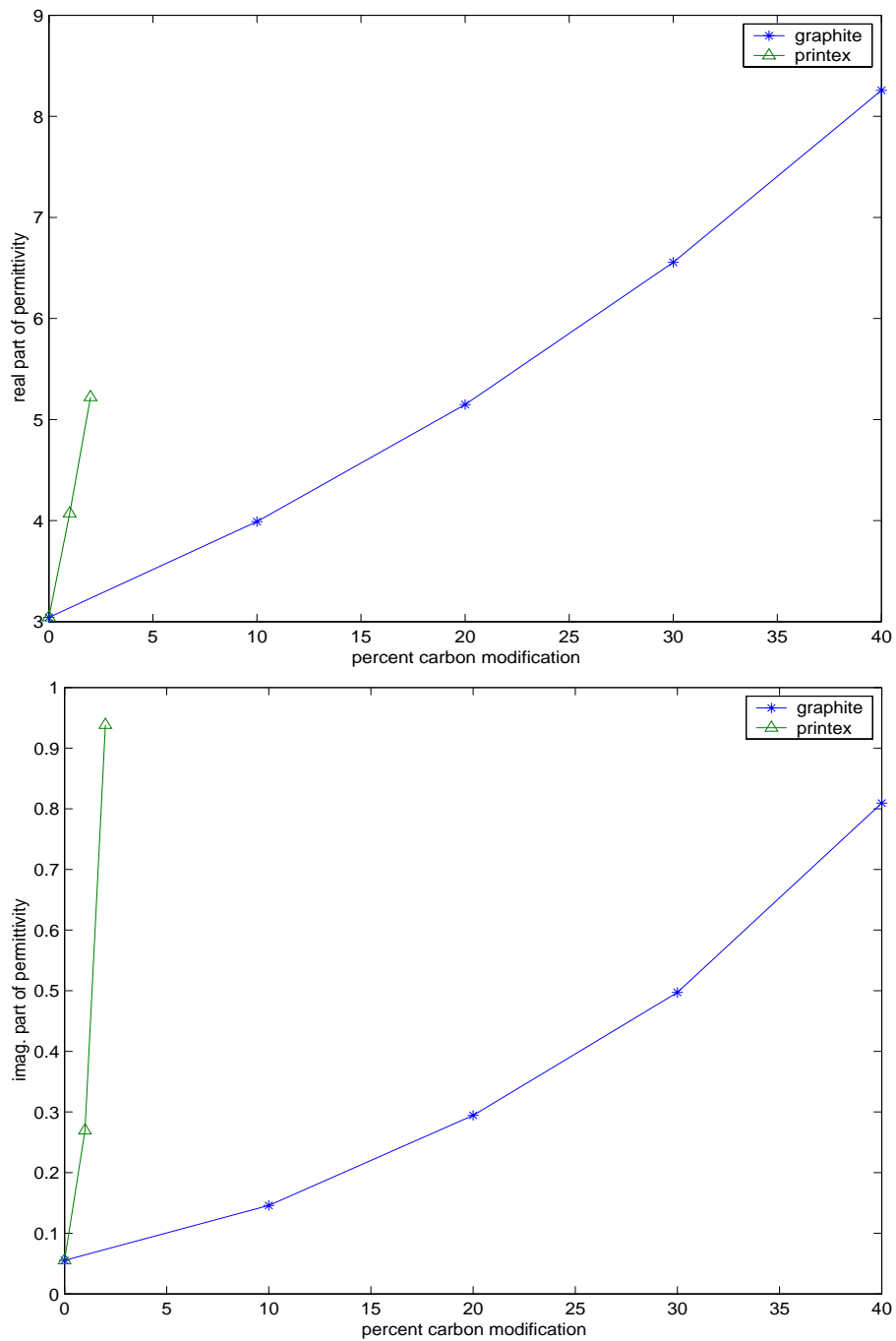


Figure 5.6: Measured real and imaginary part of permittivity as function of added percentage of carbon modification.

and

$$\varepsilon'' = \frac{\omega\tau(\varepsilon_s - \varepsilon_\infty)}{1 + \omega^2\tau^2}. \quad (5.4)$$

Equations (5.3) and (5.4) can be used to determine the two remaining model parameters from the desired real and imaginary parts of the dielectric constant at the center frequency.

$$\varepsilon_s = \varepsilon'(\omega_c) + \varepsilon''(\omega_c) \quad (5.5)$$

$$\varepsilon_\infty = \varepsilon'(\omega_c) - \varepsilon''(\omega_c). \quad (5.6)$$

Figure 5.7 shows the application of the model to the silicone absorber. The fit is very good for the loss and acceptable for the real part. The Debye model shows a stronger decline of the real part due to the large loss of the material which causes a large difference of static and infinite dielectric constant as expected from equations (5.5) and (5.6). This must be accepted as the 1st order Debye model is the only model which is usable for the modelling of frequency independent losses and implemented in available FDTD solvers at the moment. However, more exact modelling of arbitrary frequency dependent material would be desirable.

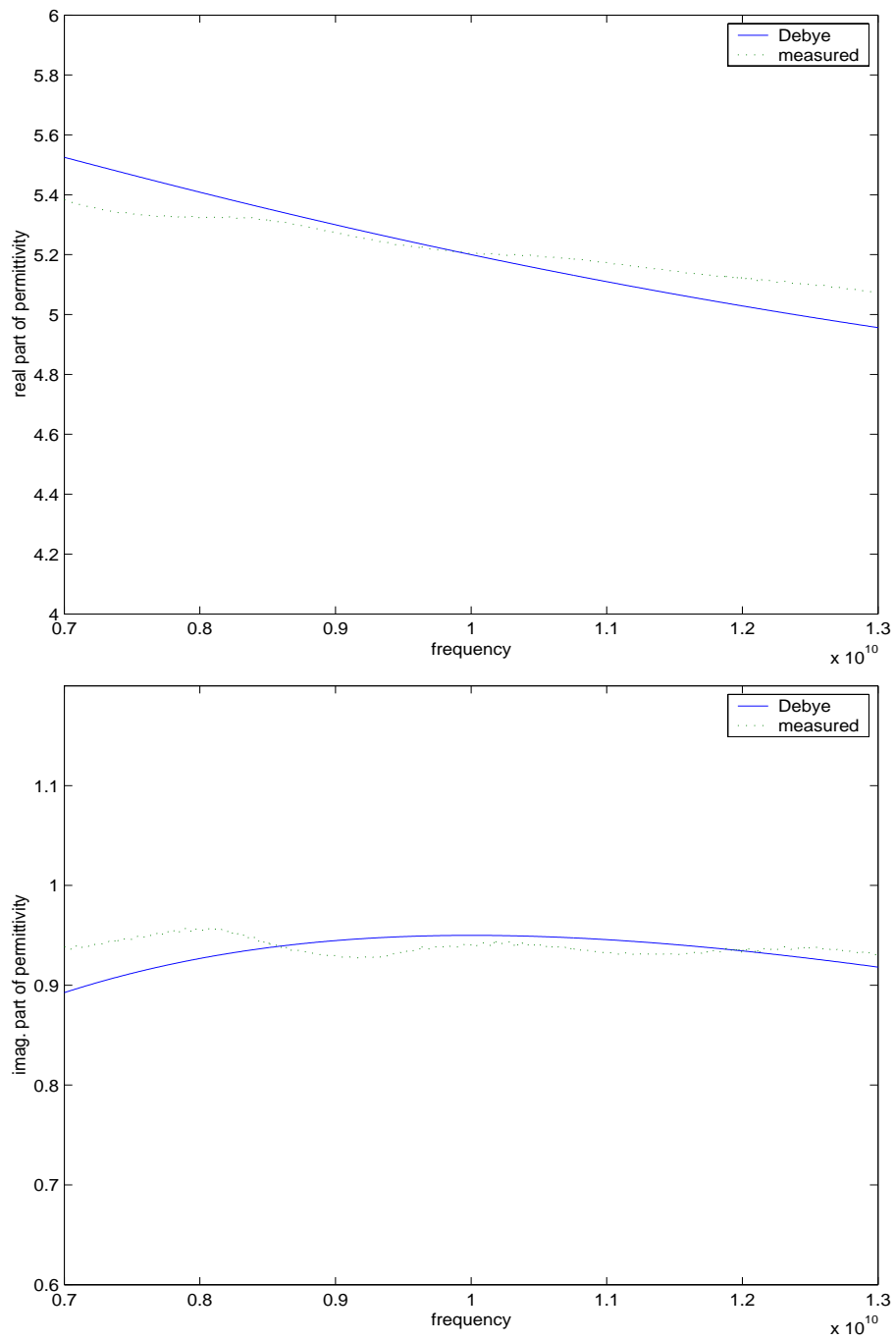


Figure 5.7: Comparison of measured real and imaginary part of permittivity and 1st order Debye model.

5.1.4 Automated Multi-Port S-Parameter Measurement System

System Design

The resonators used for microwave resonator imaging are devices having a number of ports which makes measuring the device using a conventional two-port network analyzer an extensive work. A multi-port device is defined as a device having a number of ports N , where $N > 2$. The standard measuring procedure for such a device would be to connect two of the ports of the device under test (DUT) to the VNA test ports and terminate the remaining $N-2$ ones by connecting them to well-matched terminations. This procedure is very time consuming and can lead to errors because of the high operator involvement. Thus the task of measuring the scattering matrix of the multi-port cavity must therefore be automated.

Two basic approaches to the design of such an automated multi-port scattering parameter measuring system are possible. The first is to extend the VNA by adding additional test ports and additional receivers. This will give the most accurate and fastest system. As the test set including the receivers contributes a substantial part to the cost of a VNA this approach will lead to an expensive system especially when a large number of ports is to be measured. Therefore this VNA extension is currently only applicable to 3-port and 4-port VNA's.

The second approach is the multiplexing of the VNA test ports to the N ports of the device under test. This solution will ultimately decrease measuring accuracy as additional error sources are introduced to the system. Furthermore the speed of the system will be reduced since parts of the measuring sequence that can be done simultaneously with a multi-receiver VNA must be carried out sequentially. In addition the control of the system becomes more complex. Despite these drawbacks this solution allows for a large number of ports at an acceptable cost.

The switching system can be designed as a full crossbar system capable of switching each port of the DUT to both of the VNA test ports or to a termination. Reduced systems requiring fewer switches can also be used if one is interested in measuring certain scattering parameters only. Reduced systems are preferred in production environments where the proper operation of a multi-port device can be assured by measuring a few of its scattering parameters only. However, for the microwave imaging system a full crossbar switching system is used, which gives the flexibility of being able to measure the entire scattering matrix. A standard VNA is capable of measuring only two ports at a time. Therefore a switching matrix connecting the selected ports to the VNA and terminating the remaining with the characteristic line impedance is needed. The schematic of this matrix is shown in figure 5.8.

The ports of the DUT are connected to single-pole three-throw (SP3T) switches. These connect the port to one of the second stage switches or to a matched termination. This design allows immediate connection of the port of the DUT to a termination and avoids accumulation of return loss of several switches and junctions. The second stage consists of SPNT switches where N is the number of ports of the DUT. The switching matrix is designed to be reconfigurable. All interconnec-

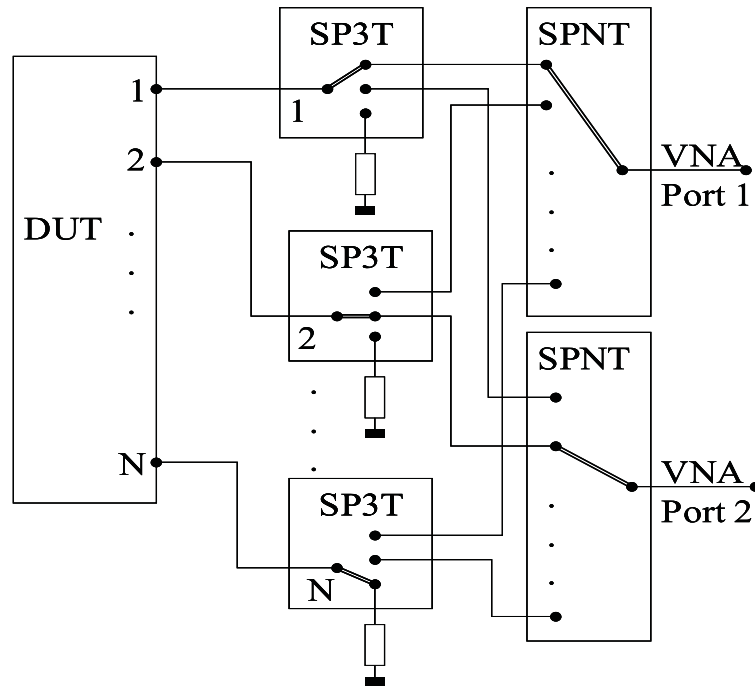


Figure 5.8: Switch matrix layout

tions are made externally using semi-rigid coaxial lines and SMA connectors. The use of semi-rigid line assures sufficient phase stability of the system.

In all states the signal only has to pass two switches which assures low insertion loss and also low reflection of the whole switching system. A standard two-port calibration with reference planes directly at the ports of the DUT is used when measuring. All errors in the paths connecting the device under test to the VNA ports are corrected. These errors include imperfect amplitude flatness of the switching system and phase distortion. Crosstalk between the channels is at an unmeasurable level for the designed system and is usually not corrected. If stronger crosstalk occurs the error introduced can be removed by a two-port calibration including isolation terms.

Mechanical switches are used instead of semiconductor ones for the system because of their superior electrical properties. The switching time of about 10 ms is acceptable for this application. The performance of the switches must be verified to ensure good operation of the system. A good ratio between on- and off-state isolation is important in order to yield accurate measurements and a low return loss of the switches must be achieved to minimize errors due to the mismatch seen by the DUT at the ports not connected to the VNA.

The performance of a typical switch is presented in figure 5.9. The transmission of the switches is close to a perfect switch with transmission better than -0.15 dB for the whole switching system bandwidth from DC to 18 GHz. The measured off-state isolation is the same order of magnitude as the noise floor of the VNA. The input match of the switch is better than -27 dB up to 14 GHz with degradation above.

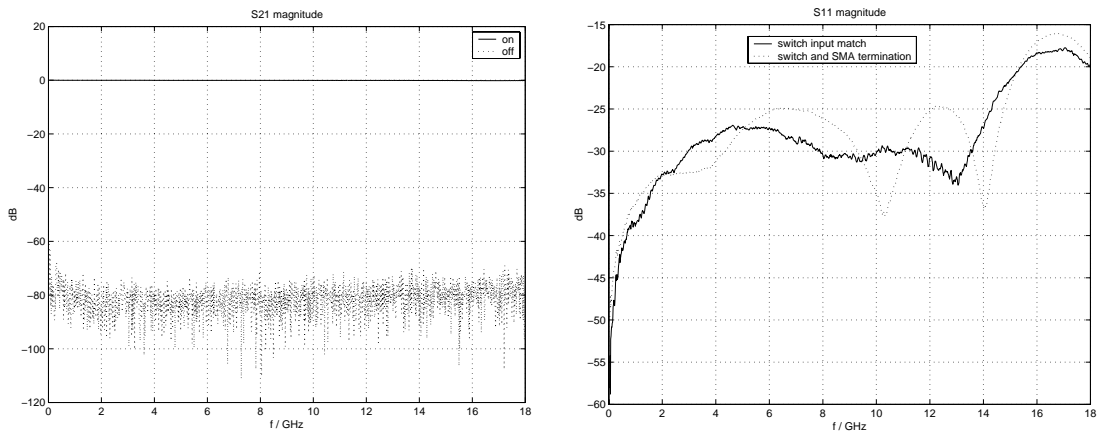


Figure 5.9: On- and off-state transmission of a switch (left), input match of a switch and accumulated input match of a switch with SMA termination at output (right)

The input match of the switch terminated with a standard $50\ \Omega$ SMA termination is slightly worse due to the contribution of the necessarily imperfect load to the overall reflection.

Correction for Imperfect Terminations

The remaining mismatch at the ports which are terminated by matched loads is not corrected by the two-port calibration. This causes errors in the measurement which can be minimized by using switches with low VSWR rating and good quality matches. Although the return losses of the switch itself and the used terminations are quite good as shown in figure 5.9, the resulting reflection seen by the device under test when connected as in actual measurements is much larger because of several additional connections. The actual input match seen by the DUT at three ports of the multi-port measuring system is depicted in figure 5.10. These could still be neglected for highly reflective lossy devices but may cause errors when measuring well-matched and low-loss devices.

For the system shown in figure 5.8 a correction method is used to remove errors caused by the imperfect terminations. It is based on the idea of scattering matrix reference impedance transformation given in [83], [84] and [85]. Although these transformations do not preserve the well-known unitary and symmetry properties of the scattering matrix of a lossless reciprocal device, the concept of reference impedance transformation has turned out to be very useful. It is therefore applied together with a novel transformation.

In each measurement a 2×2 scattering matrix is obtained where the measured parameters are normalized to the system impedance of the measuring system (usually $50\ \Omega$) while the remaining $N-2$ ports are normalized to the impedances seen at the reference planes looking into the measuring system. In order to form the full $N \times N$ scattering matrix with consistent port impedances, the measured scattering parameters are normalized to the impedance of the imperfect terminations. These transformed scattering parameters are exactly the same as the elements of the full

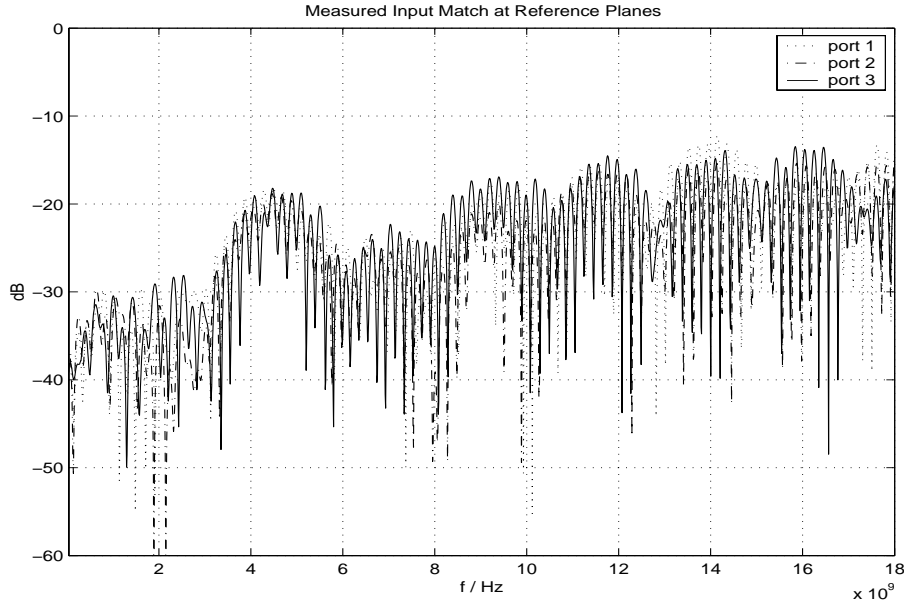


Figure 5.10: Input match as seen by the DUT

$N \times N$ matrix as all $N-2$ ports are perfectly matched now because the port reference impedances are now the impedances of the imperfect terminations. The port reference impedances must be known for the normalization and can be obtained by measuring the reflection seen by the DUT as in figure 5.10.

The procedure for transforming a set of scattering parameters to a new set of known port impedances can be developed from generalized scattering parameter description [6]. The voltages and currents at the terminals of a N -port device can be defined by

$$\underline{U} = [Z]^{1/2}(\underline{A} + \underline{B}) = [\bar{Z}]^{1/2}(\bar{\underline{A}} + \bar{\underline{B}}) = [Z]^{1/2}([I] + [S])\underline{A} \quad (5.7)$$

$$\underline{I} = [Z]^{-1/2}(\underline{A} - \underline{B}) = [\bar{Z}]^{-1/2}(\bar{\underline{A}} - \bar{\underline{B}}) = [Z]^{1/2}([I] - [S])\underline{A}. \quad (5.8)$$

Here $[Z]$ and $[\bar{Z}]$ are the diagonal matrices containing the old and new port reference impedances, \underline{A} and \underline{B} are the incident and reflected wave amplitudes for the old reference impedances, $\bar{\underline{A}}$ and $\bar{\underline{B}}$ are the incident and reflected wave amplitudes for the new reference impedances, $[I]$ is the $N \times N$ identity matrix and $[S]$ is the scattering matrix for the old set of reference impedances. The reflected waves in the old reference impedance system are eliminated using the measured scattering matrix. Equations (5.7) and (5.8) can be used to express the incident wave

$$\underline{A} = ([I] + [S])^{-1}[Z]^{-1/2}[\bar{Z}]^{1/2}(\bar{\underline{A}} + \bar{\underline{B}}) \quad (5.9)$$

$$\underline{A} = ([I] - [S])^{-1}[Z]^{1/2}[\bar{Z}]^{-1/2}(\bar{\underline{A}} - \bar{\underline{B}}) \quad (5.10)$$

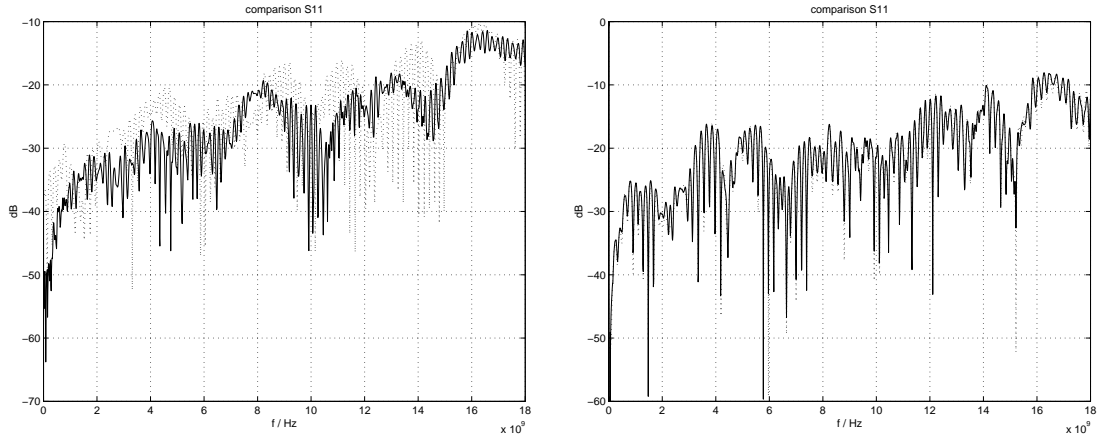


Figure 5.11: S_{11} of a directional coupler measured with port combinations 1-2 and 1-3 before (left) and after (right) reference impedance transformation

Using the equality of (5.9) and (5.10) to eliminate the incident waves in the old reference impedance system and reorganizing terms yields

$$\begin{aligned} \underline{\bar{B}} = & \left(([I] + [S])^{-1} [Z]^{-1/2} [\bar{Z}]^{1/2} + ([I] - [S])^{-1} [Z]^{1/2} [\bar{Z}]^{-1/2} \right)^{-1} \\ & \left(-([I] + [S])^{-1} [Z]^{-1/2} [\bar{Z}]^{1/2} + ([I] - [S])^{-1} [Z]^{1/2} [\bar{Z}]^{-1/2} \right) \underline{\bar{A}}. \end{aligned} \quad (5.11)$$

This gives the looked for scattering matrix with the new set of port reference impedances $[\bar{Z}]$.

After transforming the measured 2x2 scattering matrices to the mismatch reference impedances the full NxN matrix may be formed. At this point a consistency check can be applied to the diagonal elements of the full NxN scattering matrix. These elements are measured in N-1 two-port measurements. Prior to the application of equation (5.11) each of the N-1 measurements will give a different result due to the different terminations at each port. After the transformation the diagonal elements are the same from N-1 two-port measurements indicating that the full NxN matrix may be formed consistently from the transformed measurement results. This is shown on measurements of the input match of a directional coupler in figure 5.11. The measurements show differences in the measured reflection coefficient S_{11} for measurements with different port combinations due to the different termination at the remaining ports of the coupler in each measurement. These differences are removed by the application of the reference impedance transformation as expected.

Equation (5.11) is again applied to the full NxN scattering matrix to calculate the DUT scattering matrix normalized to 50Ω port impedances. The role of $[\bar{Z}]$ and $[Z]$ is interchanged at this step. This procedure allows for full error correction of the scattering parameter measuring system. The error in the signal paths of the two ports currently measured are corrected by the two-port error correction of the VNA while errors caused by the mismatch at the remaining N-2 ports are corrected by the reference impedance transformation procedure.

Because the mismatch seen by the DUT at the N-2 terminated ports can be removed by the above procedure the question arises whether it is necessary to use high

quality switches and terminations. The reason for using well-matched terminations is the accuracy of the reference impedance transformation (5.11). The condition number of the first term which is to be inverted is rising quickly when the port reference impedances assume values close to short or open. The numerical accuracy of the correction procedure which applies the reference impedance transformation twice will therefore decline for this case. The highest accuracy is achieved when the port impedances are close to each other and close to 50Ω as the term $[Z]^{-1/2}[\bar{Z}]^{1/2}$ will approach the identity matrix and will give optimum condition of the system of equations to solve.

Calibration of the Multi-Port System

The multi-port measuring procedure described above requires $N(N - 1)/2$ 2-port measurements. This also requires that $N(N - 1)/2$ port combinations are calibrated using a standard 2-port calibration. Because of its wideband capability and few mechanical work involved the Through Reflect Match (TRM) calibration method is preferred. Each two-port calibration requires 4 measurements of one-port standards and one measurement of the two-port through standard which needs two mechanical connections. Therefore a total of $6N(N - 1)/2$ mechanical connections is needed to calibrate the whole system. This would lead to a high amount of mechanical work involved as for a 4-port measurement 36 connection must be made in the calibration process. However, a large number of the one-port measurements is redundant as the one-port standard measurements are the same regardless of the second port in the calibration. Therefore use of the built-in calibration procedures of the VNA is not recommended. The raw receiver data should be transferred to a PC and the whole error correction carried out externally. The algorithms in [86] are used for this purpose. The saved receiver readings of the measurements of the one-port calibration standards can then be used for $N - 1$ two-port calibrations. The trough measurements require $2N(N - 1)/2$ connections while the one-port standard measurements account for $2N$ mechanical connections. The total number of connections is reduced to $N(N - 1) + 2N = N(N + 1)$. For a 4-port measurement the number of connections is reduced to 20 which is a substantial reduction. This approach allows for quick and convenient calibration of the multi-port scattering parameter measuring system.

There are optimized multi-port calibration methods capable of correcting for the mismatch errors [87] but are available for 4-port measurements only. The generalization of this algorithm for an arbitrary number of ports leads to optimum calibration methods requiring a minimum number of standard two-port calibrations as presented in [88].

Experimental Verification of the Multi-Port System

Measurements of a 6 dB directional coupler have been carried out to show the validity of the proposed reference impedance transformation and to verify the performance of the multi-port test set. One of the ports of the coupler is equipped with a fix matched load by the manufacturer. The measurements for the coupling and insertion

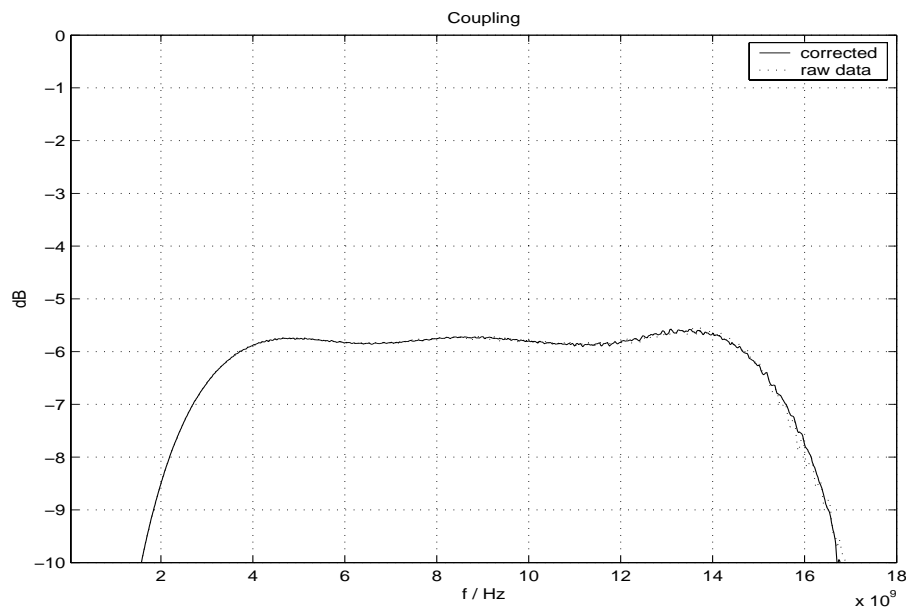


Figure 5.12: Measured coupling of a 6 dB coupler before and after correction for imperfect terminations

loss are virtually the same before and after the correction due to the good properties of the switching test set as shown in figures 5.12 and 5.13.

The isolation measurement is more sensitive to the mismatch at the through arm of the coupler and shows considerable improvement when the correction for the imperfect termination is carried out (figure 5.14). To compare the performance of the multi-port system with the present standard multi-port measuring method which is the mechanical connection of a load to the unmeasured ports, the coupler has been measured using a conventional two-port calibration and several loads. The results in figure 5.15 show that the isolation measured using the switching test set is the same as the one measured with a high precision calibration standard load. The measurement using a standard SMA termination is degraded by the imperfect match of the load. This proves the excellent accuracy of the system which is the same as if high precision calibration standards were connected to all unmeasured ports.

There is somewhat more noise compared to the calibration standard measurement because the wiring of the multi-port system could not be done using phase stable cables only for economic reasons. The system is not only more convenient to use it does also enhance the accuracy of the measurement as in standard measurement environments one would hardly use high precision calibration standards to terminate all ports. The system design aiming for almost perfect behavior of the switching matrix and removing the small remaining errors by additional correction methods has led to a high precision multi-port VNA system. In its current set-up 6 ports can be measured. The system firmware and error correction software is capable of using up to 18 ports. To the author's best knowledge this is the first fully

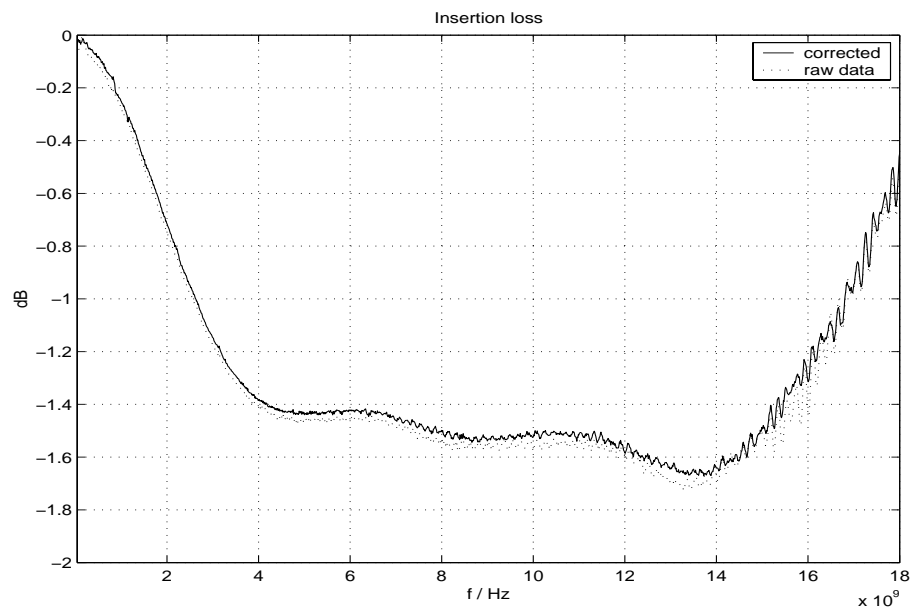


Figure 5.13: Measured insertion loss of a 6 dB coupler before and after correction for imperfect terminations

error corrected multi-port VNA system featuring such a high number of ports.

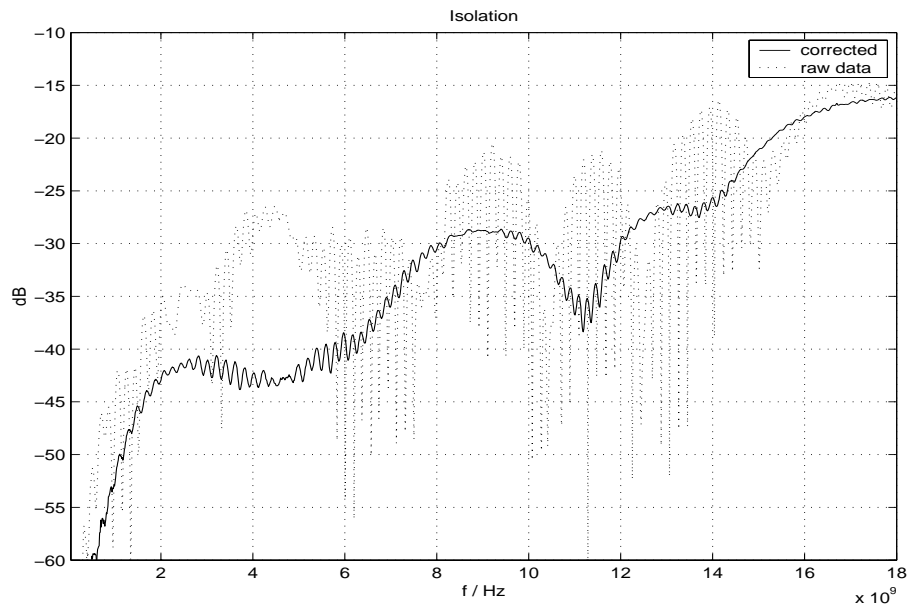


Figure 5.14: Measured isolation of a 6 dB coupler before and after correction for imperfect terminations

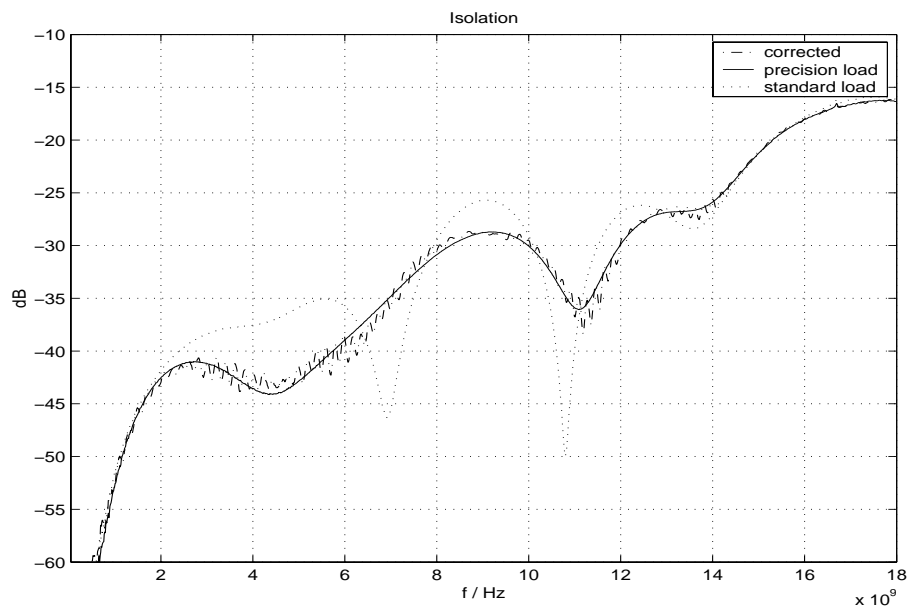


Figure 5.15: Isolation of a coupler measured with the multi-port test set, a high precision load and a standard SMA load

5.1.5 Software Architecture

Because the direct problem solution of finding the scattering parameters for a three-dimensional structure is a difficult task itself, commercial software is used for this purpose. The FDTD software CST Microwave Studio is selected because of its superior speed compared to other, non-commercial software. This software package must be integrated into the iterative process which is implemented in MATLAB. As the FDTD package is available for the Windows operating system only, a suitable technology for the interaction of applications of different vendors must be used. The ActiveX technology [89], [90] supplies the features needed. It allows software components to communicate via a standardized interface and using their functions. Because this happens at runtime it is more flexible than the former Dynamic Link Library approach.

The microwave imaging software operates as shown in figure 5.16. The error corrected scattering parameters from the multi-port measuring system are passed to the imaging algorithm via a file interface. The widely used industrial standard Touchstone file format available on all commercial VNA's is used for that purpose. The iterative algorithm as developed in chapter 3 is implemented in a MATLAB program. This main program controls the settings of the direct problem solver and updates the current object model. This is done via the ActiveX interfaces supplied by both Microwave Studio and MATLAB. The MATLAB program acts as a client and accesses the full functionality of the FDTD software via its standardized ActiveX interface. The function calls are confirmed so that synchronization between the software components is assured.

The Visual Basic macro interpreter integrated in Microwave Studio can indirectly be accessed via the Microwave Studio application object interface. The macro language is used to automate repeatedly occurring modelling tasks like material layer definitions and creation of modelling objects. The results of the FDTD solver are not passed via the ActiveX interface. This is again done via files which are ASCII files in a Microwave Studio specific format. Using this architecture a system for iterative three-dimensional imaging can be integrated with very little programming work. The software layout is basically a system for nonlinear optimization of three-dimensional structures. Here the material parameters of the volume enclosed by the resonator are optimized to match the measurements. The same software design can also be used to optimize arbitrary microwave components. This is achieved by effectively using the functionality of verified software components which was one of the motivations for the development of the ActiveX technology.

The computing time required for the calculation of one column of the scattering matrix is about 100 s for the prototypes described in section 5.1.2. 40 seconds of this total time are used for the verification of the model. This clearly is redundant as the FDTD model of the cavity is not changed in between the calculation runs. There are efficient parallelization schemes for FDTD algorithms. In [78] savings of up to 95 % were achieved using a cluster of 24 PC's. The parallelization could be used in a similar way for microwave imaging resonators. This can reduce the time required for a high resolution image from 1 day to approximately 1 hour on a 2 GHz

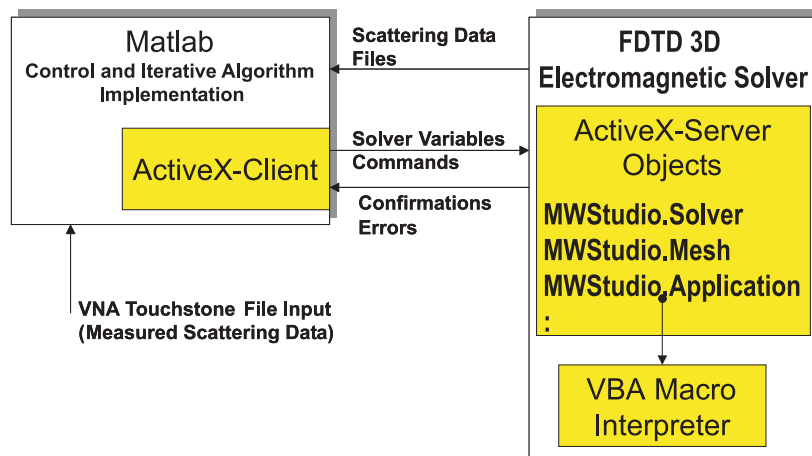


Figure 5.16: Software architecture of the microwave resonator tomography imaging system

PC. First attempts to develop FDTD software incorporating the special features needed for microwave imaging were made using the Maya FDTD code [91] and code developed especially for the simulation of resonators [92]. Although only absolutely necessary features are integrated both codes are currently not sufficiently advanced and are considerably slower compared to commercial packages.

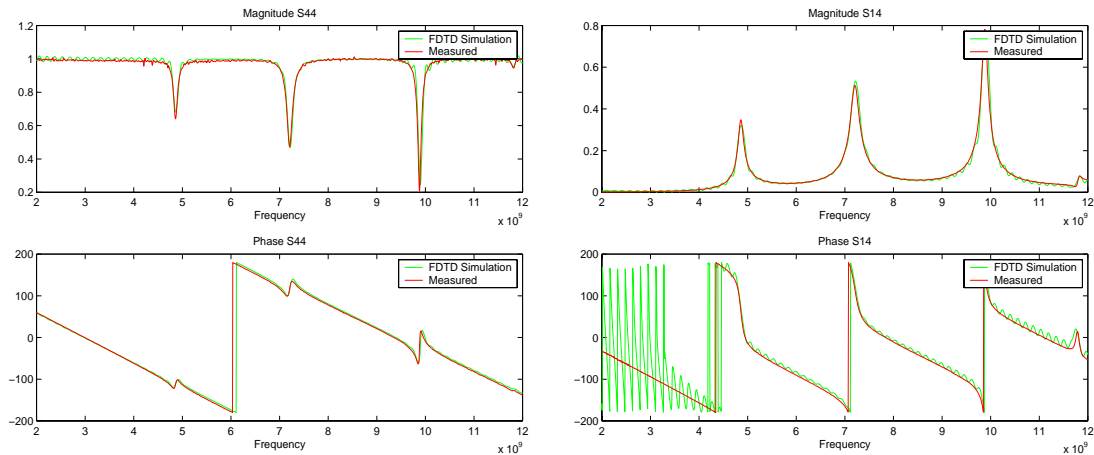


Figure 5.17: Comparison of measured and calculated reflection at port 4 and transmission between ports 1 and 4 of the unloaded cavity

5.2 Imaging System Operation

5.2.1 System Calibration

This section covers some aspects of the operation of the microwave resonator imaging system described in the previous sections. Because of the system complexity and the numerous possible error sources the measuring set-up and the FDTD model must be verified. Measurements and simulations of the empty cavity are used for that purpose. This is equivalent to an additional step of system calibration. The properties of the manufactured cavity are verified by comparison of the measurements of the empty resonator with an high accuracy simulation. Possible errors in the cavity or in the rest of the system can easily be identified by comparing measurements, simulation and by using the symmetry properties of the cavity. In addition the cavity is a reciprocal device, a fact that can also be used to check the validity of the measured scattering parameters. For the iterative process a very accurate parameter setting would result in unacceptable time consumption. A trade-off between time and accuracy must be found here. The FDTD parameters which can be adjusted and have the greatest influence on time consumption are the number of mesh cells and the steady state limit. The geometry of the structure is approximated more accurately when the number of mesh cells is increased. The steady state limit determines the level of power at which the RF energy in the calculation volume is considered to be completely decayed.

The calculated and measured scattering parameters should match very well when these parameters are adjusted for high accuracy. An RMS error of better than 20 dB between measured and calculated scattering parameters is considered to be sufficient. Figure 5.17 shows the resulting scattering parameters after a system calibration. The mesh density is set to 15 lines per wavelength and a steady state limit is -30 dB in this example. The oscillation of the transmission phase from 2 GHz to 4 GHz is due to the very low transmission magnitude below the first resonance.

5.2.2 Avoiding Undesired Constraints

While the non-negativity constraint for the dielectric contrast function $c = \varepsilon_r - 1$ is often used in iterative regularization schemes as an additional penalty function [50], it is undesired for the regularization using the spectral object expansion. The image of the object will exhibit Gibbs phenomenon at sharp steps when expanded into a limited number of cosine terms. When this step is at an air interface the relative permittivity will assume values smaller than unity at the air side. This cannot be avoided when the expansion coefficients are calculated sequentially starting with lower order. For the one-dimensional profile reconstruction it can be shown that the convergence is better if permittivities smaller than in vacuum are accepted as long as the residual function is decreased.

However, the case of a relative permittivity smaller than one (e.g. in plasma) is not provided in most of the computer codes. To overcome this undesired constraint a scaling factor is introduced. The material parameters are all multiplied by this factor F .

$$\tilde{\varepsilon} = F\varepsilon \quad (5.12)$$

$$\tilde{\mu} = F\mu \quad (5.13)$$

$$\tilde{\sigma} = F\sigma \quad (5.14)$$

It is now required that all properties of the scaled system used to describe it from outside are equal to the ones of the original system. The intrinsic impedance is invariant to the scaling factor.

$$\tilde{Z}_0 = \sqrt{\frac{\tilde{\mu}}{\tilde{\varepsilon}}} = \sqrt{\frac{\mu F}{\varepsilon F}} = Z_0 \quad (5.15)$$

while the wave velocity is by a factor of F lower.

$$\tilde{c} = \frac{1}{\sqrt{\tilde{\mu}\tilde{\varepsilon}}} = \frac{c}{F} \quad (5.16)$$

The wavenumber of a plane wave in the scaled system is

$$\tilde{k}_0 = \frac{2\pi f}{\tilde{c}} = Fk_0 \quad (5.17)$$

In order to preserve the phases φ for all signals transmitted through or reflected from the scaled system the dimensions s must be scaled down by F .

$$\tilde{s} = \frac{s}{F} \quad (5.18)$$

$$\tilde{\varphi} = \tilde{k}_0\tilde{s} = \varphi \quad (5.19)$$

Permittivity and permeability values up to $1/F$ can be used in the direct problem solution when this scaling is applied. The resonator model will be scaled down by a factor of $1/F$ and all material parameters are multiplied by F as they are passed from the imaging algorithm to the FDTD solver. Numerical testing of this approach shows that the scattering parameters calculated using scaled models are virtually equal to the ones obtained for the original model.

5.2.3 Initial Guess

The determination of a suitable initial guess is a critical part of the solution of a nonlinear problem as it will decide whether the sequence of iterates will converge or not. In the microwave resonator tomography a good initial guess can directly be calculated from the scattering matrix measurements. The method is based on evaluating low-frequency information. The input reflection of the cavity loaded with the object is measured at one of the ports. The first resonance frequency f_1 is determined from this measurement. In the rectangular cavity with the measures a , b and c along the x , y and z axis respectively and $a > b > c$, the lowest resonance is the TE_{110} mode at which

$$\bar{\varepsilon}_r k_0^2 \approx \left(\frac{\pi}{a}\right)^2 + \left(\frac{\pi}{b}\right)^2. \quad (5.20)$$

The looked for initial guess is the zeroth order expansion coefficient d_{000} in (3.20) which is equal to the average permittivity $\bar{\varepsilon}_r$ in (5.20). This can be used to directly calculate the initial guess from the measured resonance frequency.

$$d_{000} = \bar{\varepsilon}_r \approx \left(\frac{1}{a^2} + \frac{1}{b^2}\right) \frac{c_0^2}{4f_1^2} \quad (5.21)$$

This works very well in practice giving the average permittivity always better than $\pm 10\%$ and typically $\pm 3\%$. From an initial guess so close to the actual value the iterative scheme using successively relaxed smoothness constrained converges reliably in all observed cases.

5.2.4 Imaging Process

The imaging process uses the iteration method which has been presented in detail in chapter 3. It starts with the initial guess for the average permittivity calculated as above. The number of expansion coefficients that can be determined is calculated using the same concept as in the one-dimensional case, see (3.23). This number is estimated using the condition that the frequency of maximum effect \hat{f}_{nml} should be within the measuring frequency interval. For the expansion coefficient d_{nml} this frequency is given by

$$\hat{f}_{nml} = \frac{c_0}{4\sqrt{\bar{\varepsilon}_r}} \sqrt{\left(\frac{n}{a}\right)^2 + \left(\frac{m}{b}\right)^2 + \left(\frac{l}{c}\right)^2}. \quad (5.22)$$

The condition for the inclusion into the imaging process is simply

$$\hat{f}_{nml} \leq f_{max}. \quad (5.23)$$

The number of parameters in the iterative optimization is now given by the average permittivity and the measuring frequency range. The measuring frequency range is divided into a fixed number of equally sized intervals in order to use the hybrid Jacobian approximation effectively. Each expansion coefficient is assigned to a certain

frequency interval using equation (5.22). Then the iterative algorithm is entered. The average permittivity is further improved in the first iteration. The smoothness constraint is relaxed and a further expansion coefficient is calculated in the next iteration step. The frequency range used for the matching of the direct problem solution and the measurements is increased also after a number of iterations. At this point the Jacobian is reset by a full finite differences approximation. This continues until the full measurement frequency range is used and the imaging process has reached its maximum resolution. The pseudo code for the imaging algorithm is given in the following:

- read measurements
- find lowest resonance frequency of object loaded resonator
- calculate initial guess according to equation (5.21)
- estimate number of expansion coefficients determinable N_{max} using condition (5.23)
- divide measuring frequency range into intervals
- assign each coefficient to one of the frequency intervals
- for $n = 1$ to N_{max}
 - calculate next iterate using algorithms presented in chapter 3, solve direct problem using FDTD
 - if $n = N_{max}$ break
 - increase number of expansion coefficients
 - if coefficient n is assigned to next frequency interval increase frequency range and calculate full FD- Jacobian
- display results

This algorithm is tested on several simulation and measuring examples in the next section.

5.3 Experimental Results

5.3.1 Sensitivity Distribution within the Cavity

Some properties as the noise sensitivity and the effect of weighting of the expansion coefficients were evaluated for the one-dimensional case already. Other properties are special to microwave resonator imaging. This applies to the distribution of the sensitivity of the measured scattering parameters for material changes as a function of position within the cavity. The quality of the image depends on the sensitivity of the scattering parameters of the loaded cavity to changes of dielectric constant and loss. The aim is to achieve an evenly distributed sensitivity. This can be obtained by evenly distributing the coupling ports of the cavity over its surface.

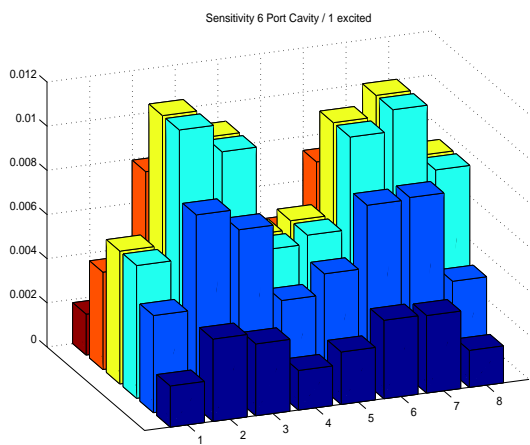
As the electric field strength of all cavity modes decreases towards the nearly perfectly conducting resonator walls the sensitivity is expected to be lower at the walls. Very low field strengths are expected in the corners of the cavity. This is confirmed by the sensitivity of scattering parameters for material changes of the 6 port cavity shown in figure 5.18(a) which is basically the electric field distribution of the TE_{210} mode. The sensitivity shown is the mean value over the frequency range from 2.5 GHz to 9.5 GHz where only the port at the right hand side has been excited. When this resonator is used for imaging the results obtained are distorted towards the corners of the cavity. Trying to achieve a more homogenous distribution by exciting all ports leads to slight improvements of the sensitivity along the walls. The TE_{210} mode still dominates and leads to low sensitivity especially in the corners as shown in figure 5.18(b).

By redesigning the cavity and placing four additional ports in the corners the sensitivity can be much improved as shown in figure 5.18(c). This design also shows better imaging performance compared to the 6 port design. Errors of the imaged permittivity in the corners occurred in almost every case while the 10 port cavity does not show that undesired behavior and gives correct results for the whole cavity volume. A similar result can be achieved using the absorbing wall coating. The sensitivity distribution is slightly improved compared to the previous case but not clearly superior as can be seen by comparison of figures 5.18(c) and (d). However, the resonator using absorbing wall coating performs much better for all imaging examples evaluated.

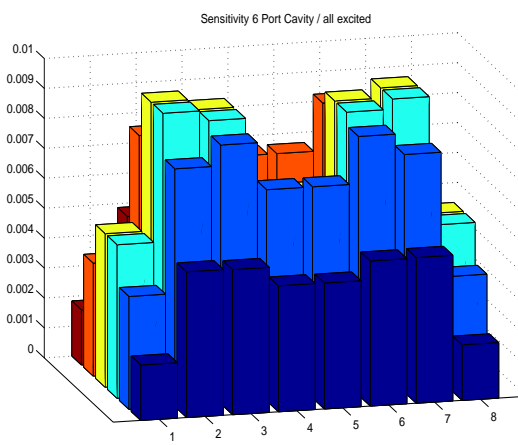
5.3.2 Effect of measuring Frequency Range

The effect of the measuring frequency range is to be checked again for the three-dimensional case. It is expected that the measuring frequency range determines the resolution achievable for a fixed measuring accuracy. This is assessed on simulations of a reference object consisting of two rectangular blocks depicted in figure 5.19(a). The background material is teflon with $\epsilon_r = 2.04$, which is assumed to be lossless and the object consists of two blocks of silicone rubber with $\epsilon_r = 3.02 - j0.05$. The blocks are only $10 \text{ mm} \times 6 \text{ mm}$ in size.

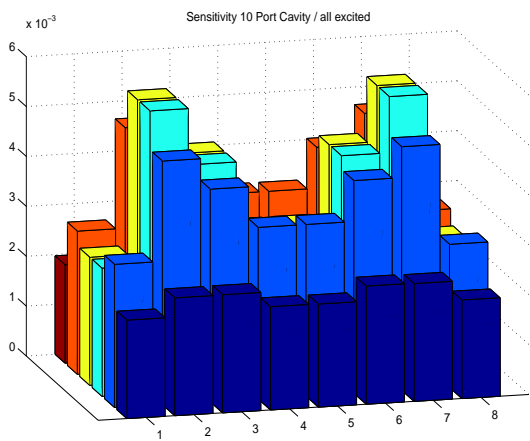
The result obtained using a frequency range from 2.5 GHz to 9.5 GHz is shown



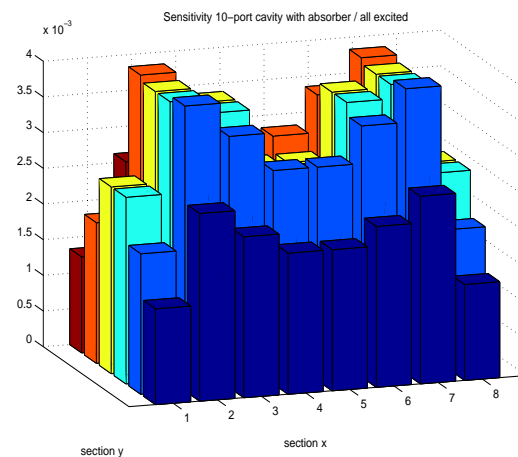
(a)



(b)



(c)



(d)

Figure 5.18: Sensitivity distribution in an imaging resonator: (a) 6-port cavity with 1 port excited, (b) 6-port cavity with all ports excited, (c) 10-port cavity with all ports excited, (d) 10-port cavity with absorber wall coating and all ports excited

in figure 5.19(c). The two blocks are clearly detected and can also be separated. The resolution of the system is obviously in the mm-range. This is surprising as the shortest wavelength is about 3 cm and it would not be possible to achieve such a high resolution using any free-space set-up. The use of resonators allows much better resolution because of the near field measurements. Also the shift of resonances by the permittivity and the lowering of the quality factor are not bound to the condition that the obstacle must be at least a certain fraction of wavelength in size.

When increasing the measuring frequency the resolution can be further improved as can be seen from figure 5.19(d). While the shape of the blocks was not clearly reconstructed in the 9.5 GHz example the rectangular shape of the two blocks can be imaged by adding further 3 GHz of bandwidth. The information contained in this band is fully exploited as the scattering parameters at the last iteration match the ones of the actual object almost perfectly as shown in figure 5.19(b). As the residual function is almost zero already any attempt to further increase resolution by adding more parameters to the optimization must fail. The images obtained for the dielectric loss are not as good as the ones for the real part which is mainly due to the low loss contrast.

The same windowing functions as in the one-dimensional case are applied to two and three-dimensional objects too. The error is again reduced best by applying the \cos^2 -filter as shown in figure 5.20. The images obtained after filtering again lack resolution despite their lower RMS error. The effect of the measuring frequency band is much stronger than the improvements that can be achieved by expansion coefficient weighting.

5.3.3 Effect of cavity wall coating

The importance of selecting a suitable material for the resonator wall coating is evident from the following reconstruction example. The same reference object in 5.19(a) is reconstructed. The result in figure 5.19(d) was obtained using the material described in section 5.1.3. The object is now imaged using different materials for the wall coating. Attempting to image the object with air surrounding the object fails. The result reconstructed using a 4 mm thick teflon material layer matched to the object background which also consists of teflon is given in figure 5.21(a). The image is severely distorted. The result can be somewhat improved using an unmatched lossy layer as in figure 5.21(b) but is still inferior to the result obtained using the the absorber proposed in section 5.1.3 as is obvious from comparison of figures 5.21(b) and 5.19(d).

5.3.4 FDTD model accuracy

Table 5.1 is showing the effect of the number of discrete materials in the FDTD model. Comparison of columns 2 and 4 reveals that the error in the image is decreased with more materials. Clearly, a separate material having the parameters given by the current object expansion for each mesh cell would be the optimum for the iterative algorithm. An increase of the number of materials above approxi-

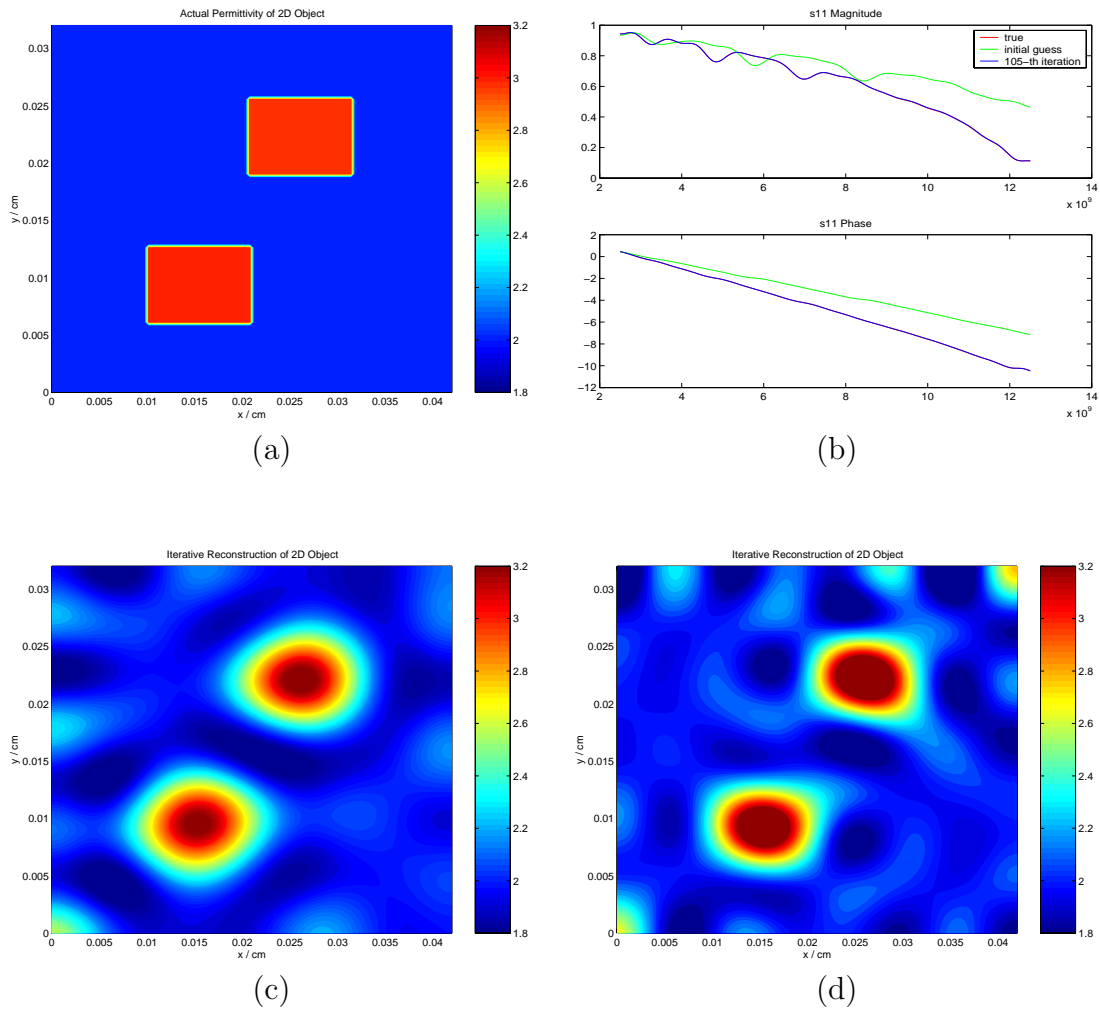


Figure 5.19: Effect of measurement frequency range on 3D tomography: (a) actual permittivity, (b) comparison of scattering parameters, (c) imaged permittivity for 2.5 GHz to 9.5 GHz measuring frequency range, (d) imaged permittivity for 2.5 GHz to 12.5 GHz measuring frequency range

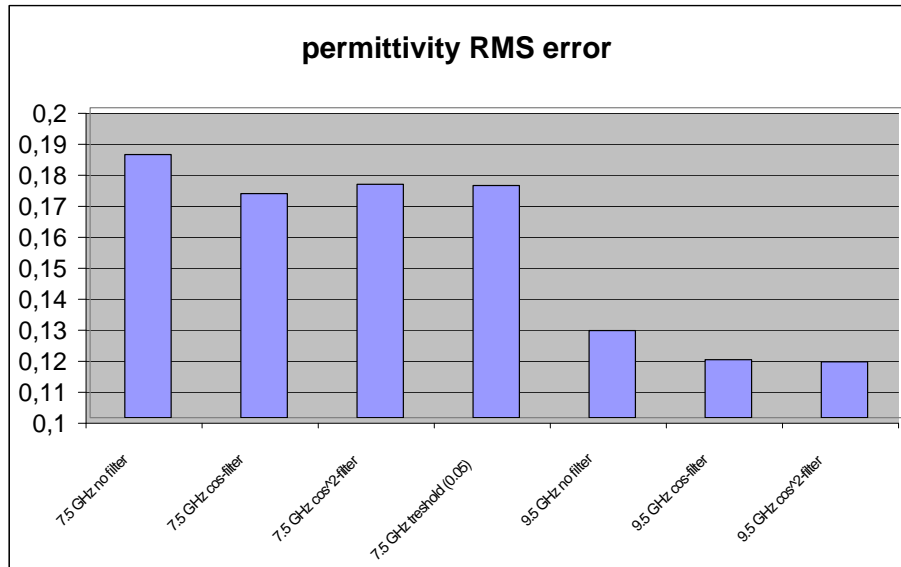


Figure 5.20: Permittivity error for different measuring frequency ranges and coefficient weighting filters

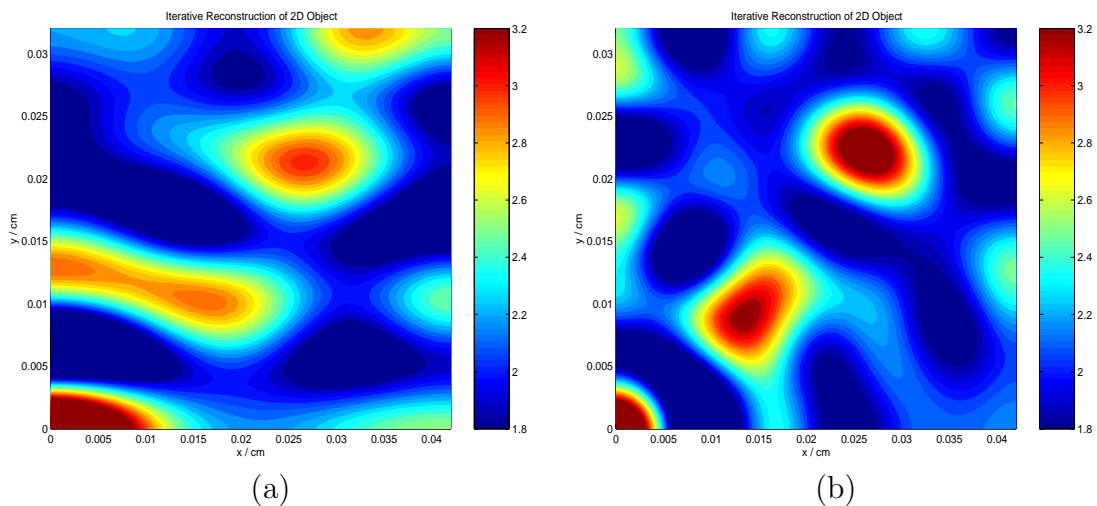


Figure 5.21: Effect of the material used for wall coating: (a) matching layer, (b) lossy unmatched layer

experiment	1	2	3	4
f/GHz	2.5-9.5	2.5-9.5	2.5-7.5	2.5-9.5
iterations	1	2	2	2
blocks	8 x 6 x 1	8 x 6 x 1	10 x 8 x 1	10 x 8 x 1
residual S-parameter	0.006688	0.003466	0.001953	0.001920
RMS error ε	0.2567	0.1883	0.2562	0.1674
relative error ε	10 %	7.5 %	10 %	6.7 %

Table 5.1: Effect of several parameters on imaging accuracy

mately 100 leads to a very complex model of the cavity and very large overhead in the computational process.

The number of iterations in table 5.1 gives the repetition of iteration steps with the same number of parameters in the optimization. Due to the quick convergence of the Gauss-Newton algorithm an number of 2 is sufficient. A higher number of iterations is not improving results measurably but increases time consumption. As already pointed out above increasing the frequency range for measuring scattering parameters leads to improved resolution and image accuracy as indicated by comparison of columns 3 and 4.

5.3.5 Error functions

The error function of the algorithm is the residual error between measured scattering parameters and simulated ones of the current object iterate. Each iteration step using the successive relaxation iteration scheme is essentially a one-dimensional non-linear optimization problem. This is because the expansion coefficients determined previously are already very close to the actual value and are only altered by small values in the subsequent iteration steps.

To evaluate the convergence behavior of the algorithm the error functions are evaluated as a function of one expansion coefficient. The average permittivity is a crucial parameter as it is the starting point for the whole iterative process. It is optimized in the first iteration steps using low-frequency measuring data. The initial guess produced by (5.21) is always closer than 10% to the actual value. As seen from figure 5.22(a) convergence is always assured from a value in that range. The dip of the error function at a permittivity value of $\varepsilon_r = 7.6$ is caused by shifting the second resonance of the cavity to the fundamental one.

The convergence range for the expansion coefficients d_{100} in figures 5.22(b) and d_{220} in 5.22(b) is again sufficiently large. It remains large when an higher order coefficient is calculated while the ones determined previously are still erroneous as in figure 5.22(d). Only the minimum is shifted. As all expansion coefficients currently included are improved in the subsequent iteration steps stable convergence is expected for this case also. These very well-behaved error functions are the reason for the good convergence in all cases.

To observe the convergence behavior of the iterative algorithm the residual error

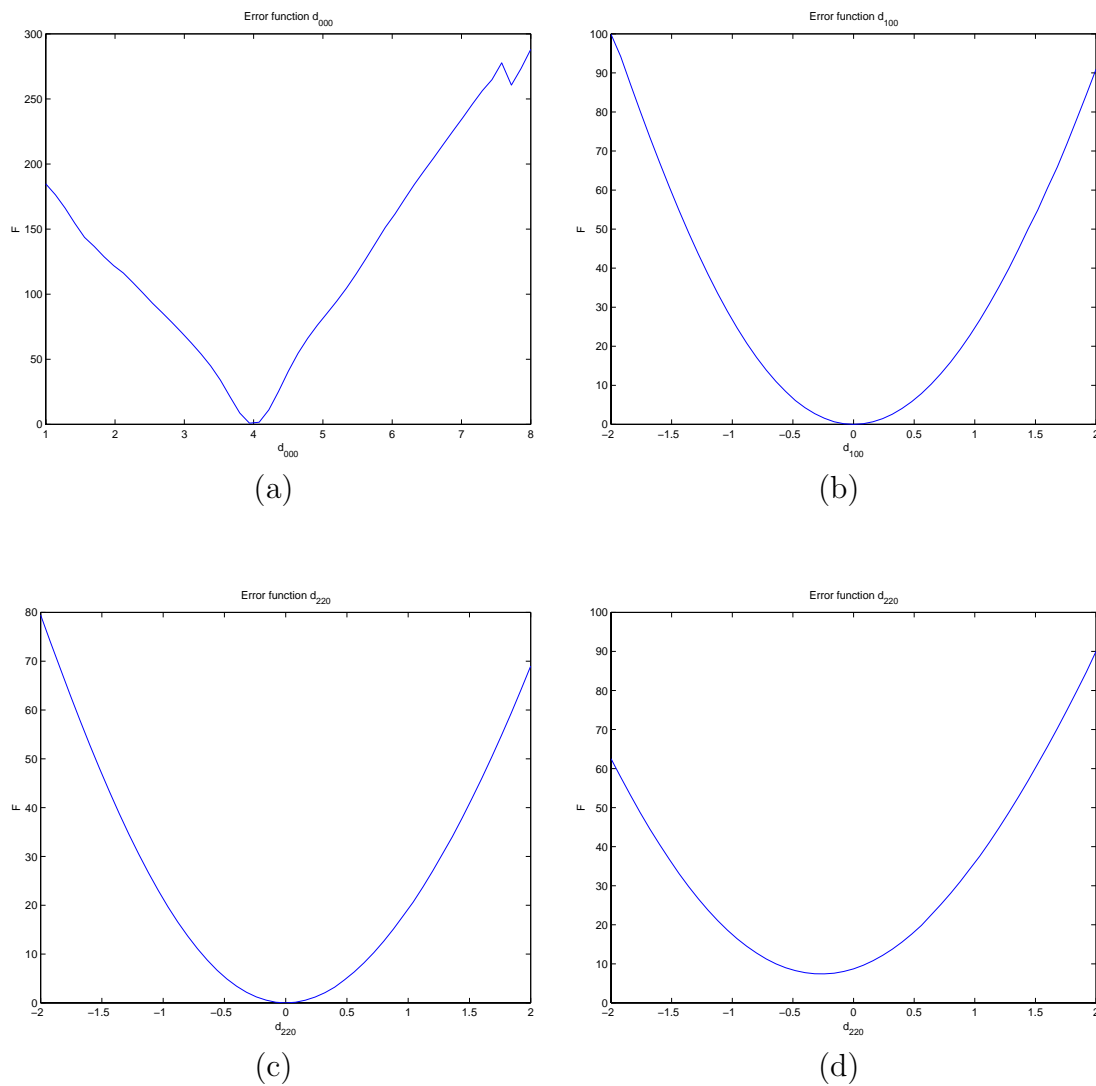


Figure 5.22: Error functions of the nonlinear least squares problem as a function of: (a) average permittivity d_{000} , (b) expansion coefficient d_{100} , (c) expansion coefficient d_{220} , (d) expansion coefficient d_{220} with error in average permittivity

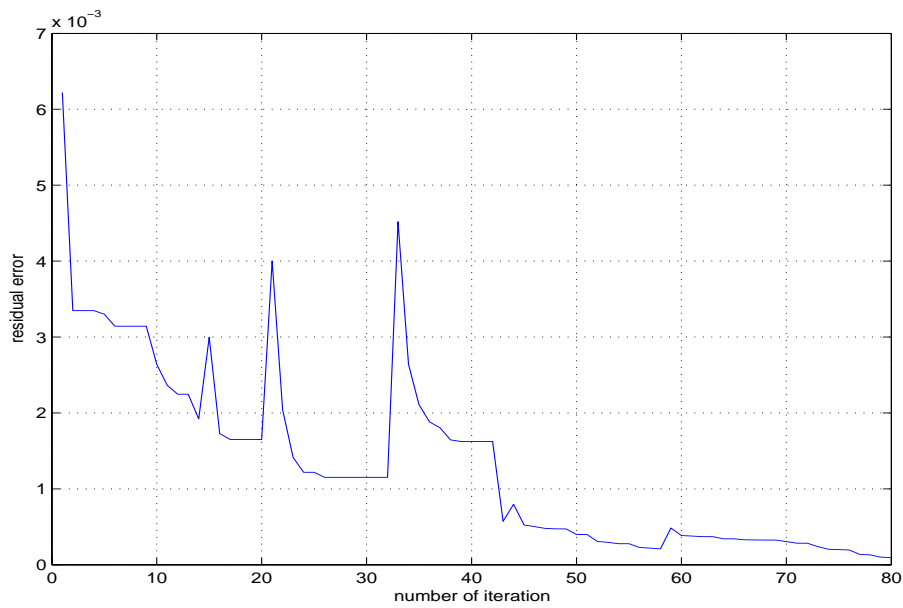


Figure 5.23: Residual error as a function of iteration for the imaging process of the object in figure 5.19

per frequency point average over all scattering parameters is plotted as a function of iteration steps. The algorithm converges fast and stable. The step increases of the residual error occur whenever the frequency interval included in the optimization is increased. The last frequency interval increases do not cause a considerable increase of the residual error function which means that the scattering parameters can be matched very well for the entire measuring frequency range with the current object. This indicates that the maximum resolution of the imaging process has been achieved and that it is not possible to extract more information about details of the object from the measuring data.

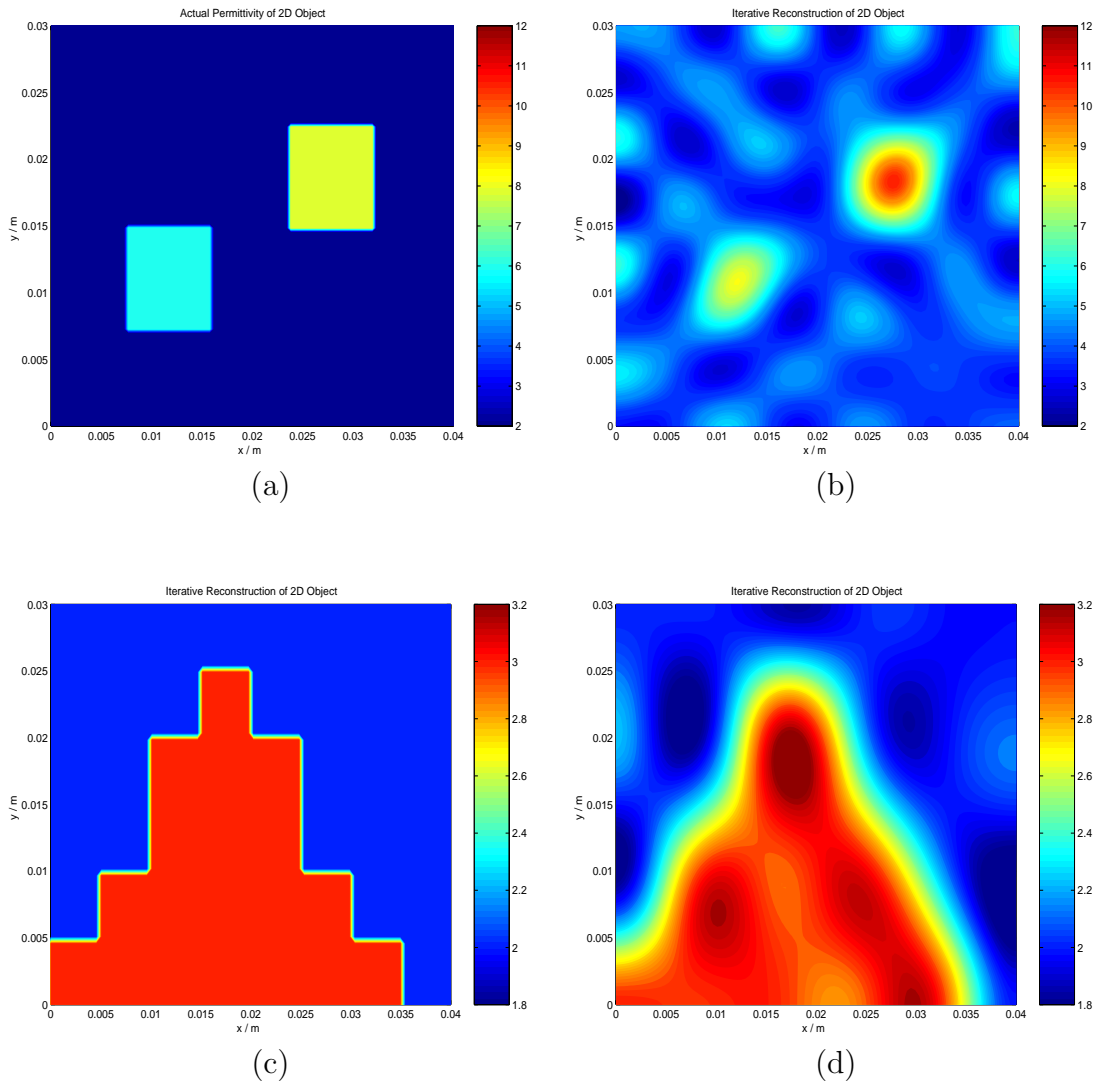


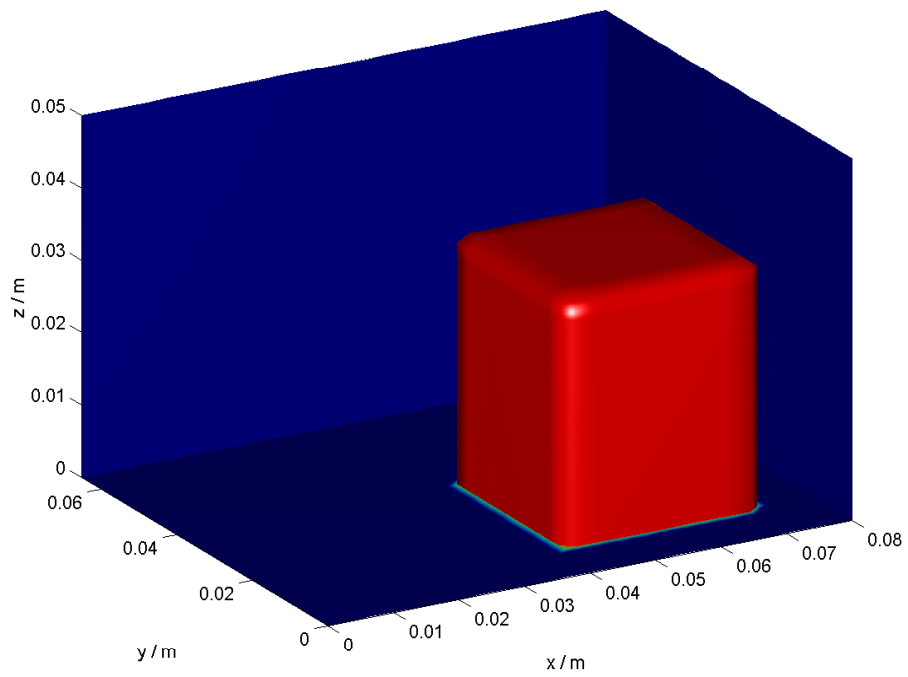
Figure 5.24: Imaging results: (a) two blocks with $\varepsilon_r = 6 - j0.02$ and $\varepsilon_r = 8 - j0.02$ in PTFE background, (b) image of the two block object, (c) staircase profile $\varepsilon_r = 2$ and $\varepsilon_r = 3 - j0.02$, (d) image of the staircase object

5.3.6 Imaging results

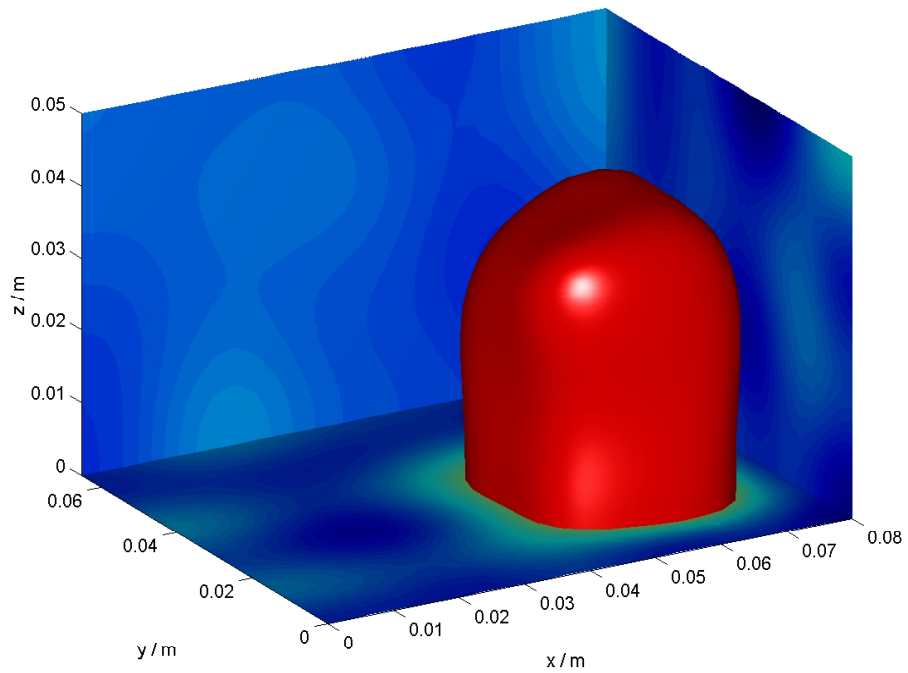
Several objects having different dielectric contrast and geometrical shapes were imaged to validate general applicability of the algorithm. The algorithm is capable of reliably imaging all test objects. The results given here were obtained using absolutely no a-priori knowledge and algorithm adjustments. The measurements or simulation data for the true object are sufficient to calculate the algorithm parameters as outlined in section 5.2.

The images in the previous examples are cross sectional ones of three-dimensional objects having an only two-dimensional permittivity distribution. The imaging process is two-dimensional as the permittivity is assumed to be homogenous in the third dimension. A fully three-dimensional imaging example is given in the following. A

block of silicone rubber is embedded in a PTFE background. The iso-surface value for the plots is 2.5 which is half distance between background and object.



(a)



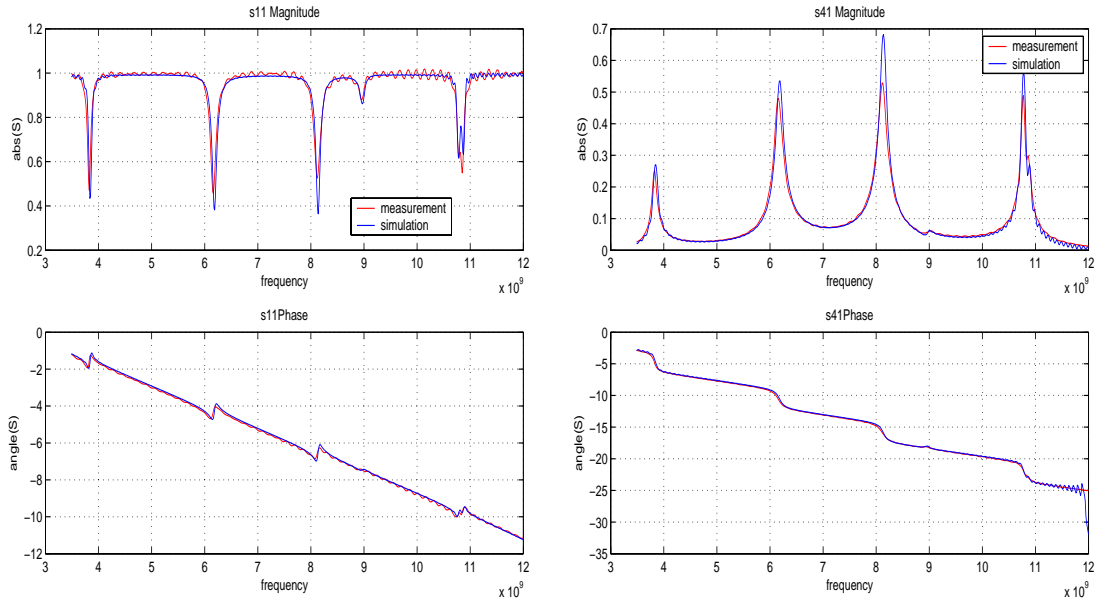
(b)

Figure 5.25: 3D Imaging: (a) true permittivity for a silicone rubber block in PTFE background, (b) image of the object

5.3.7 Measuring Results

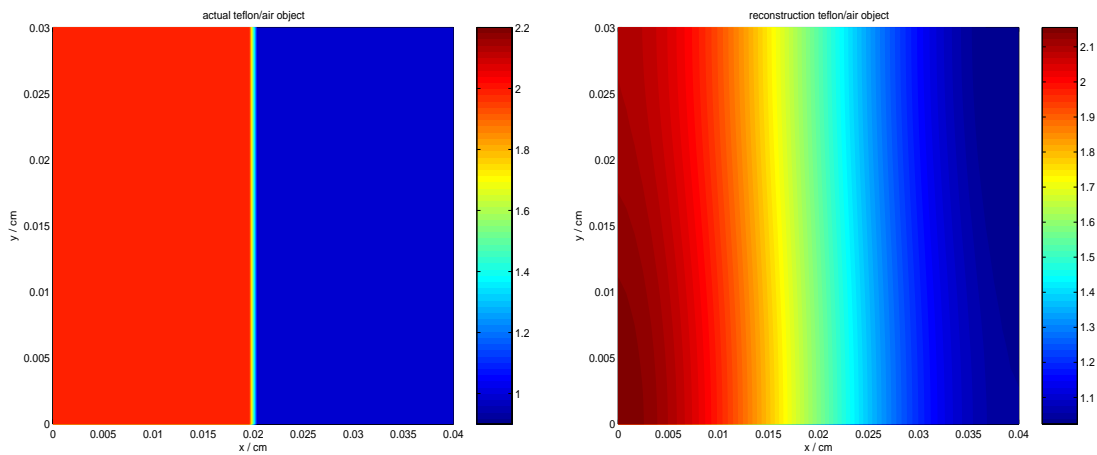
The microwave resonator imaging system is tested on a reference object consisting of an air section and a teflon block. The permittivity is a function of one dimension only for this object. This fact was not incorporated into the imaging as a-priori knowledge. The imaging of the object was therefore a three-dimensional reconstruction. The measuring data obtained with the multi-port VNA is shown in figure 5.26 (a) and (b). It is compared to a high accuracy simulation. Both transmission and reflection measurements show declining accuracy in the high frequency range. This is caused by the phase instability of the cables as discussed in section 5.1.4. Non-repeatability due to switch wear was identified as an additional error source. While the switches are still within specification their repeatability drops. The worn switches do not give the same scattering parameters when switched backed to the same state. As repeatability is required for error correction this errors cannot be removed by calibration.

The cross-sections in the xy-plane of the actual object and its image are given in figure 5.26(c) and (d). The air to teflon transition is blurred due to the band limiting. This measurement was carried out without absorbing layer or matching layer because this is the most critical case as discussed in section 5.3.3. The noise in the measuring data causes substantial deviations of the measuring data from simulation as shown in figures 5.26(a) and (b). Despite the noise the images obtained from both data sets are virtually identical. The RMS error in the imaged permittivity is only 15% for both the reconstruction from measuring and from simulated data. It can be improved by using absorbing resonator wall coating. The fact that the system gives equal results for noisy measuring and simulation data proves its excellent robustness. As this is a high-contrast object the quantitative information gained is far better than what is possible using any of the methods discussed in the state of the art. From these measurements it can be concluded that the application of microwave resonator imaging for three-dimensional imaging in real world applications is feasible.



(a)

(b)



(c)

(d)

Figure 5.26: Imaging from measuring data: (a) comparison of measured and simulated S_{11} , (b) comparison of measured and simulated S_{41} , (c) cross section of actual teflon / air object , (d) cross sectional image of the object

Chapter 6

Summary and Conclusion

The microwave imaging method presented in this work has several aspects that make it favorable over other microwave imaging methods. This has been achieved by adopting entirely new approaches in every aspect of the imaging system. It uses an expansion of the object into an orthogonal set of functions. This is the basis for a very efficient iterative regularization. In addition, a subset in the measuring data can be connected to each object parameter. The successively relaxed smoothness constraint starting from an initial guess that is derived from low frequency data gives global convergence to the desired solution. The iterative algorithm developed to implement this regularization is efficient because a suitable Jacobian approximation method was developed.

The one-dimensional measuring setup uses waveguide sections loaded with the object to image for collecting highly accurate vectorial measurements. Dielectrically loaded waveguide to coaxial transitions enable the collection of necessary low frequency information. The three-dimensional measuring setup using resonators instead of a free-space setup allows for convenient high-accuracy measurements. The use of a FDTD solver enables accurate solution of the direct problem where the only limitation is the trade-off between accuracy and time consumption.

The algorithm is verified by imaging examples using both simulated and measuring data. The weak scattering limitation of other microwave imaging methods is avoided and quantitative results are obtained. The results show that the proposed method is capable of accurately reconstructing high contrast and lossy objects that cannot be imaged by any other microwave imaging method.

Several novel devices were developed to practically implement and test the proposed imaging system. These include dielectrically loaded waveguide to coaxial transitions and optimized TRL calibration kits for the one-dimensional inverse profile problem. In order to conveniently carry out the measurements using the multi-port resonators used for three-dimensional imaging an automated multi-port VNA was developed. Algorithms for the calibration and error correction of this instrument were also developed. Special microwave absorber materials exhibiting a low real part of the permittivity and high dielectric loss were developed. These side products of this work may well be very useful for many other purposes in the field of microwave engineering.

The foundations for the application of microwave imaging to one-dimensional and three-dimensional problems are given in this work. Further improvement is needed in the speed of the direct problem solution. As there is strong demand for the solution of other large electromagnetic problems a lot of research is devoted to this topic presently. Using parallelization in the direct problem solution could reduce the time required for the image reconstruction considerably. When these issues are solved real world applications in the field of medical imaging, environmental imaging and nondestructive material testing can be targeted.

Appendix A

Proof of the Tikhonov Reconstruction Formula

The basic expression for the regularized solution of an inverse problem is

$$f_\alpha^* = V \text{diag}(w_\alpha(s^2) s_i^{-1}) U^T g^* \quad (\text{A.1})$$

as outlined in section 3.1. The weights applied to the singular values for Tikhonov regularization are given by

$$w_\alpha(s^2) = \frac{s^2}{s^2 + \alpha}. \quad (\text{A.2})$$

This yields the final regularized solution using Tikhonov regularization.

$$f_\alpha^* = V \text{diag} \left(\frac{s_i}{s_i^2 + \alpha} \right) U^T g^* \quad (\text{A.3})$$

As this requires the computationally expensive calculation of the SVD an alternative reconstruction equation (3.16) was introduced in section 3.1.

$$f_\alpha^* = (A^T A + \alpha I)^{-1} A^T g^* \quad (\text{A.4})$$

This has the considerable advantage of being able to find the solution from the operator A and its transpose only. The equivalence of A.3 and A.4 can be shown using the SVD of A which is given by

$$A = U S V^T. \quad (\text{A.5})$$

The transpose of the matrix product is

$$A^T = V S^T U^T. \quad (\text{A.6})$$

The left and right singular vectors are orthonormal which is a property of the SVD [62].

$$U^T U = I \quad (\text{A.7})$$

$$V^T V = I \quad (\text{A.8})$$

From this follows that the transpose matrices of U and V are identical to the inverses.

$$U^T = U^{-1} \quad (\text{A.9})$$

$$V^T = V^{-1} \quad (\text{A.10})$$

Replacing the mapping operator A in (A.4) using its SVD yields

$$f_\alpha^* = (VS^T U^T U S V^T + \alpha I)^{-1} V S^T U^T. \quad (\text{A.11})$$

Using (A.7) and $S^T S = S^2$ this can be written as

$$f_\alpha^* = [V (S^2 V^T + V^{-1} \alpha)]^{-1} V S^T U^T. \quad (\text{A.12})$$

This can be further simplified using (A.10).

$$f_\alpha^* = (S^2 V^T + V^T \alpha)^{-1} S^T U^T. \quad (\text{A.13})$$

$$f_\alpha^* = [(S^2 + \alpha I) V^T]^{-1} S^T U^T \quad (\text{A.14})$$

$$f_\alpha^* = V (S^2 + \alpha I)^{-1} S^T U^T \quad (\text{A.15})$$

Combining the inner terms to one matrix yields

$$f_\alpha^* = V \text{diag} \left(\frac{s_i}{s_i^2 + \alpha} \right) U^T, \quad (\text{A.16})$$

which is just (A.3).

Appendix B

Calculation of the Gradient, Jacobian and Hessian for Nonlinear Least-Squares

In the nonlinear least-squares problem one tries to find the minimizer x_* of the cost function

$$f(x) = \frac{1}{2}F^T(x)F(x) = \frac{1}{2} \sum_{i=1}^m (f_i(x))^2. \quad (\text{B.1})$$

For the algorithm discussed in section 3.2 the gradient $\nabla f(x)$ is required frequently. It is given by

$$\nabla f(x) = \left[\frac{\partial f(x)}{\partial x_1} \cdots \frac{\partial f(x)}{\partial x_n} \right]^T \quad (\text{B.2})$$

Another basic matrix in multivariable calculus is the Jacobian J . Its elements are by definition

$$J(x)_{ij} = \frac{\partial f_i(x)}{\partial x_j}. \quad (\text{B.3})$$

The gradient of a nonlinear least-squares problem at the point x can be calculated using

$$\nabla f(x) = \nabla \left(\frac{1}{2}F^T(x)F(x) \right) = \nabla \left(\frac{1}{2} \sum_{i=1}^m (f_i(x))^2 \right) \quad (\text{B.4})$$

$$= \sum_{i=1}^m \nabla f_i(x) f_i(x) \quad (\text{B.5})$$

From (B.2) and (B.3) it can be seen that the rows of the Jacobian are equal to the gradient of the function f_i . Applying this to B.5 gives a useful expression for obtaining the gradient from the Jacobian and the residual function itself.

$$\nabla f(x) = J^T(x)F(x) \quad (\text{B.6})$$

This is employed in step-acceptance algorithms where the gradient of the corresponding minimization problem is needed to decide whether to accept or reject a step in the Gauss-Newton Algorithm as in section 3.2.3.

A similar expression can be derived for the Hessian. The elements of the Hessian are given by

$$\nabla^2 f(x)_{ij} = \frac{\partial^2 f(x)}{\partial x_i \partial x_j}. \quad (\text{B.7})$$

Using (B.1) this yields

$$\begin{aligned} \nabla^2 f(x) &= \nabla^2 \left(\frac{1}{2} F^T(x) F(x) \right) = \nabla^2 \sum_{i=1}^m \frac{1}{2} f_i(x)^2 \\ &= \sum_{i=1}^m \nabla (\nabla f_i(x)) = \sum_{i=1}^m \nabla f_i(x) \nabla f_i^T(x) + \nabla^2 f_i(x) f_i(x) \end{aligned} \quad (\text{B.8})$$

This gives the final expression for the Hessian of a nonlinear least-squares problem.

$$\nabla^2 f(x) = J(x)^T J(x) + S(x), \quad (\text{B.9})$$

where $S(x)$ is given by

$$S(x) = \sum_{i=1}^m f_i(x) \nabla^2 f_i(x). \quad (\text{B.10})$$

Appendix C

Derivatives of a Series Expansion

The basis for the regularization introduced in section 3.1 is the object representation by the expansion into a set of orthogonal functions. To compare this with the standard smoothness constraint (3.5) the derivatives of the expansion are required. For the one-dimensional case using cosine-function the object expansion reads

$$f(z) = \sum_{n=0}^{\infty} d_n \cos(k_n z), \quad (\text{C.1})$$

where the spatial frequency $k_n = n\pi/c$ is introduced. The first derivative of the function $f(z)$ is expanded into a set of sine-functions.

$$\frac{df(z)}{dz} = \sum_{j=1}^{\infty} a_j \sin(k_j z) \quad (\text{C.2})$$

with $k_j = j\pi/c$. The expansion coefficients a_n are given by

$$N_j a_j = \int_{z=0}^c \sin(k_j z) \frac{df(z)}{dz} dz. \quad (\text{C.3})$$

The norm of the j th function is denoted by N_j .

$$N_j = \int_{z=0}^c \sin^2(k_j z) dz = \frac{c}{2} \quad (\text{C.4})$$

The expansion coefficients a_j can be calculated using partial integration.

$$\frac{c}{2} a_j = \left[\sin(k_j z) f(z) \right]_{z=0}^c - \int_{z=0}^c k_j \cos(k_j z) f(z) dz \quad (\text{C.5})$$

The first term vanishes and using (C.1) in (C.5) yields

$$\frac{c}{2} a_j = -k_j \int_{z=0}^c \cos(k_j z) \sum_{n=0}^{\infty} d_n \cos(k_n z) dz \quad (\text{C.6})$$

Because of the orthogonality property all terms of the sum except the one with $n = j$ are zero which gives the looked for expansion terms of the first derivative.

$$a_j = -\frac{2}{c}k_j \int_{z=0}^c d_j \cos^2(k_j z) dz = -k_j d_j \quad (\text{C.7})$$

The first derivative is obtained by replacing a_j in (C.2).

$$\frac{df(z)}{dz} = -\sum_{j=1}^{\infty} k_j d_j \sin(k_j z) \quad (\text{C.8})$$

This result is identical to the one that would be obtained by differentiating (C.1) term by term.

The second derivative of the object function is expanded into cosine terms.

$$\frac{d^2 f(z)}{dz^2} = \sum_{l=0}^{\infty} b_l \cos(k_l z) \quad (\text{C.9})$$

The coefficients b_l are now given by

$$N_l b_l = \int_{z=0}^c \cos(k_l z) \frac{d^2 f(z)}{dz^2} dz, \quad (\text{C.10})$$

where N_l is the norm of the l th function. The norm can be calculated using

$$N_l = \int_{z=0}^c \cos^2(k_l z) dz = \begin{cases} \frac{c}{2} & \text{for } l \neq 0 \\ c & \text{for } l = 0 \end{cases}$$

Partial integration of (C.10) yields

$$N_l b_l = \left[\cos(k_l z) \frac{df(z)}{dz} \right]_{z=0}^c + \int_{z=0}^c k_l \sin(k_l z) \frac{df(z)}{dz} dz. \quad (\text{C.11})$$

Using the expression for the first derivative obtained above together with the orthogonality property gives

$$\begin{aligned} N_l b_l &= \left[\cos(k_l z) \frac{df(z)}{dz} \right]_{z=0}^c - k_l^2 \frac{c}{2} d_l \\ &= (-1)^l \frac{df(z)}{dz} \Big|_{z=c} - \frac{df(z)}{dz} \Big|_{z=0} - k_l^2 \frac{c}{2} d_l \end{aligned} \quad (\text{C.12})$$

The final expressions for the expansion coefficients of the second derivative are then

$$b_l = \frac{2}{c} \left[(-1)^l \frac{df(z)}{dz} \Big|_{z=c} - \frac{df(z)}{dz} \Big|_{z=0} \right] - k_l^2 d_l \quad \text{for } l \neq 0 \quad (\text{C.13})$$

$$b_0 = \frac{1}{c} \left[\frac{df(z)}{dz} \Big|_{z=c} - \frac{df(z)}{dz} \Big|_{z=0} \right] \quad (\text{C.14})$$

The first terms on the right hand side of (C.13) and (C.14) are needed in order to avoid impulse functions at the borders of the expansion interval. These would otherwise occur because the first derivative is expanded into sine terms that necessarily have zeros at $z = 0$ and $z = c$. All nonzero values of the first derivative at the borders of the interval will cause a very large slope of the first derivative and consequently an impulse in the second derivative. However, these terms are determined only by the slope of the function at the borders of the interval. The second term in (C.13) is the only one caused by the variation of the function itself. The magnitude of the second derivative within the object is therefore rising quadratically with the number of spatial frequencies used for the object representation.

$$\begin{aligned} \frac{d^2 f(z)}{dz^2} &= \frac{1}{c} \left[\left. \frac{df(z)}{dz} \right|_{z=c} - \left. \frac{df(z)}{dz} \right|_{z=0} \right] \\ &+ \sum_{l=1}^{\infty} \left(\frac{2}{c} \left[(-1)^l \left. \frac{df(z)}{dz} \right|_{z=c} - \left. \frac{df(z)}{dz} \right|_{z=0} \right] - k_l^2 d_l \right) \cos(k_l z) \end{aligned} \quad (\text{C.15})$$

Bibliography

- [1] L. Yujiri, M. Shoucri, and P. Moffa, "Passive millimeter-wave imaging," *IEEE Microwave Magazin*, vol. 4, pp. 39–50, September 2003.
- [2] Agilent Technologies, "HP 8722D VNA users guide," 1996.
- [3] Agilent Technologies, "Agilent 54753A/54754A TDR plug-in modules users guide," 2000.
- [4] D. L. Colton and R. Kress, *Inverse Electromagnetic and Acoustic Scattering Theory*. Springer, 1998.
- [5] R. S. Elliot, *Electromagnetics: History, Theory and Applications*. IEEE Press, 1993.
- [6] R. E. Collin, *Foundations for Microwave Engineering*. McGraw-Hill, second ed., 1992.
- [7] R. C. Tupynamba, *Analyse und Entwurf von passiven Hochfrequenzschaltungen mit Hilfe der FDTD-Methode*. Dissertation, TU Hamburg-Harburg, 1997.
- [8] L. E. Larsen and J. H. Jacobi, "Microwave scattering parameter imagery of an isolated canine kidney," *Med. Phys.*, vol. 6, pp. 394–403, 1979.
- [9] J. C. Bolomey, A. Izadnegahdar, L. Jofre, C. Pichot, G. Perronet, and M. Soalaimani, "Microwave diffraction tomography for biomedical applications," *IEEE Trans. MTT*, vol. 30, pp. 1998–2000, November 1982.
- [10] S. C. Hagness, A. T. Taflove, and J. E. Bridges, "Two-dimensional FDTD analysis of a pulsed microwave confocal system for breast cancer detection: Fixed-focus and antenna-array sensors," *IEEE Trans. Biomed. Eng.*, vol. 45, pp. 1470–1479, December 1998.
- [11] R. A. Krueger, "Thermoacoustic CT," *IEEE-MTT-Symposium*, June 2000. Boston.
- [12] Y. Huo, R. Bansal, and Q. Zhu, "Breast tumor characterization via complex natural resonances," *IEEE MTT-S Symp. Dig.*, pp. 387–390, June 2003.

- [13] M. Krueger, A. Pesavento, H. Ermert, K. Hiltawsy, L. Heuser, H. Rosenthal, and A. Jensen, "A new system for quantitative ultrasonic breast imaging of acoustic and elastic parameters," *Acoustical Imaging*, vol. 24, pp. 253–259, 2000.
- [14] A. E. El-Rouby, F. T. Ulaby, and A. Y. Nashashibi, "MMW scattering by rough lossy dielectric cylinders and tree trunks," *IEEE Trans. Geosc. Rem. Sens.*, vol. 40, pp. 871–879, April 2002.
- [15] S. Hadjiloucas, L. S. Karatzas, and J. W. Bowen, "Measurements of leaf water content using terahertz radiation," *IEEE Trans. MTT*, vol. 47, pp. 142–149, February 1999.
- [16] H. H. Barret, "Fundamentals of the radon transform," *NATO ASI Series*, vol. F39, pp. 105–125, 1988.
- [17] J. Hadamard, *Lectures on Cauchy's Problem in Linear Partial Differential Equations*. Yale University Press, 1923.
- [18] M. Bertero and P. Boccacci, *Inverse Problems in Imaging*. IOP Publishing, 1998.
- [19] L. v. Wolfersdorf, *Inverse und schlecht gestellte Probleme*. Akademie Verlag, 1994.
- [20] K. I. Hopcraft and P. Smith, *An Introduction to Electromagnetic Inverse Scattering*. Kluwer Academic Publishers, 1992.
- [21] T. Meyer and A. S. Omar, "Efficient isolation of the nonlinearity in reconstruction problems," *55th ARFTG Conference*, June 2000. Boston.
- [22] K. I. Hopcraft and P. R. Smith, "Geometrical properties of backscattered radiation and their relation to inverse scattering," *J. Opt. Soc. Amer. A*, vol. 6, pp. 508–516, April 1989.
- [23] W. Tabbara, "Reconstruction of permittivity profiles from a spectral analysis of the reflection coefficient," *IEEE Trans. AP*, vol. 27, pp. 241–244, March 1979.
- [24] J.-C. Bolomey, D. Lesselier, C. Pichot, and W. Tabarra, "Spectral and time domain approaches to some inverse scattering problems," *IEEE Trans. AP*, vol. 29, pp. 206–212, March 1981.
- [25] T. J. Cui and C. H. Liang, "Inverse scattering method for one-dimensional inhomogeneous lossy medium by using a microwave networking technique," *IEEE Trans. MTT*, vol. 43, pp. 1773–1781, August 1995.
- [26] T. J. Cui and C. H. Liang, "Reconstruction of the permittivity profile of an inhomogeneous medium using an equivalent network method," *IEEE Trans. AP*, vol. 41, pp. 1719–1726, December 1993.

- [27] D. B. Ge and L.-J. Chen, "A direct profile inversion for weakly conducting layered medium," *IEEE Trans. AP*, vol. 39, pp. 907–909, July 1991.
- [28] H. D. Ladouceur and A. K. Jordan, "Renormalization of an inverse scattering theory for inhomogeneous dielectrics," *J. Opt. Soc. Am. A*, vol. 2, pp. 1916–1921, November 1985.
- [29] D. L. Yaggard and Y. Kim, "Accurate one-dimensional inverse scattering using a nonlinear renormalization technique," *J. Opt. Soc. Amer.*, vol. A-2, pp. 1922–1930, 1985.
- [30] M. J. Akhtar and A. S. Omar, "Reconstructing permittivity profiles using integral transforms and improved renormalization techniques," *IEEE Trans. MTT*, vol. 48, pp. 1385–1393, 2000.
- [31] M. J. Akhtar and A. S. Omar, "Reconstruction of permittivity profiles in cylindrical objects illuminated by higher order modes," in *Proc. IEEE MTT-S Symp.*, pp. 1085–1088, 2000.
- [32] V. A. Mikhnev and P. Vainkainen, "Two-step inverse scattering method for one-dimensional permittivity profiles," *IEEE Trans. AP*, vol. 48, pp. 293–298, February 2000.
- [33] C. Pichot, J. Jofre, G. Peronnet, A. Izadnegahdar, and J.-C. Bolomey, "An angular spectrum method for inhomogeneous bodies reconstruction in microwave domain," *IEEE AP-S Symp. Dig.*, pp. 664–667, May 1982.
- [34] C.-N. Chen and D. I. Hoult, *Biomedical Magnetic Resonance Technology*. Institute of Physics Publishing, 1995.
- [35] A. C. Kak and M. Slaney, *Principles of Computerized Tomographic Imaging*. IEEE Press, 1988.
- [36] M. Slaney, A. C. Kak, and L. E. Larsen, "Limitations of imaging with first first-order diffraction tomography," *IEEE Trans. MTT*, vol. 39, pp. 860–874, Aug. 1984.
- [37] D. E. Livesay and K.-M. Chen, "Electromagnetic fields induced inside arbitrarily shaped biological bodies," *IEEE Trans. MTT*, vol. 22, pp. 1273–1280, December 1974.
- [38] F. J. Paolini, "The effects of attenuation on the born reconstruction procedure for microwave diffraction tomography," *IEEE Trans. MTT*, vol. 34, pp. 366–368, March 1986.
- [39] E. Salerno, "Microwave tomography of lossy objects from monostatic measurements," *IEEE Trans. MTT*, vol. 47, pp. 986–994, July 1999.

- [40] A. Broquetas, J. Romeu, J. M. Rius, A. R. Elias-Fuste, A. Cardama, and L. Jofre, "Cylindrical geometry: A further step in active microwave tomography," *IEEE Trans. MTT*, vol. 39, pp. 836–844, May 1991.
- [41] S. Y. Semenov et al., "Three-dimensional microwave tomography: Experimental prototype of the system and vector born reconstruction method," *IEEE Trans. Biomed. Eng.*, vol. 46, pp. 937–945, August 1999.
- [42] J. M. Rius, C. Pichot, L. Jofre, J. C. Bolomey, N. Joachimowicz, A. Broquetas, and M. Ferrando, "Planar and cylindrical active microwave temperature imaging: Numerical simulations," *IEEE Trans. Biomed. Eng.*, vol. 11, pp. 457–469, December 1992.
- [43] N. Joachimowicz, J. J. Mallorqui, J.-C. Bolomey, and A. Broquetas, "Convergence and stability assessment of newton-kantorovich reconstruction algorithms for microwave tomography," *IEEE Trans. Med. Imag.*, vol. 17, pp. 562–570, August 1998.
- [44] A. Franchois, A. Joisel, C. Pichot, and J.-C. Bolomey, "Quantitative microwave imaging with a 2.45-GHz planar microwave camera," *IEEE Trans. Med. Imag.*, vol. 17, pp. 550–561, August 1998.
- [45] K. Belkebir, R. E. Kleinmann, and C. Pichot, "Microwave imaging - location and shape reconstruction from multifrequency scattering data," *IEEE Trans. MTT*, vol. 45, pp. 469–476, April 1997.
- [46] A. Franchois and C. Pichot, "Microwave imaging-complex permittivity reconstruction with a levenberg-marquardt method," *IEEE Trans. AP*, vol. 45, pp. 203–215, February 1997.
- [47] W. C. Chew and Y. M. Wang, "Reconstruction of two-dimensional permittivity distribution using the distorted born iterative method," *IEEE Trans. Med. Imaging*, vol. 9, pp. 218–225, 1990.
- [48] Y. M. Wang and W. C. Chew, "An iterative solution of the two-dimensional electromagnetic inverse scattering problem," *Int. Journ. of Imaging Systems and Technology*, vol. 1, pp. 100–108, 1989.
- [49] L. Garnero, A. Franchois, J.-P. Hugonin, and N. Joachimowicz, "Microwave imaging - complex permittivity reconstruction by simulated annealing," *IEEE Trans. MTT*, vol. 39, pp. 1801–1807, November 1991.
- [50] A. Baussard and D. Premel, "Inverse scattering with experimental microwave data using the weak membrane model and a positivity constraint," *Proc. IEEE AP-S Symposium*, vol. 1, pp. 288–291, 2002.
- [51] A. Blake and A. Zissermann, *Visual Reconstruction*. MIT Press, 1987.

- [52] R. V. McGahan, "Special session on image reconstruction using real data," *IEEE AP Magazin*, vol. 38, pp. 39–59, June 1996.
- [53] J. B. Morris, R. V. McGahan, J. L. Schmitz, R. M. Wing, D. A. Pommet, and M. A. Fiddy, "Imaging of strongly-scattering targets from real data," *IEEE AP Magazin*, vol. 39, pp. 22–26, April 1997.
- [54] R. D. Murch and D. G. H. Tan, "Reconstructing objects from the ipswich data set," *IEEE AP Magazin*, vol. 39, pp. 26–29, April 1997.
- [55] V. P. Yakubov and M. L. Masharuev, "Method of double focussing for microwave tomography," *Microwave and Opt. Techn. Letters*, vol. 13, no. 4, pp. 187–189, 1996.
- [56] M. Bertero, M. Miyakawa, P. Boccacci, F. Conte, K. Orikasa, and M. Furutani, "Image restoration in chirp-pulse microwave CT (CP-MCT)," *IEEE Trans. Biomed. Eng.*, vol. 47, pp. 690–698, May 2000.
- [57] M. Fritzsche, *Anwendung von Verfahren der Mustererkennung zur Detektion von Landminen mit Georadaren*, vol. 30 of *Forschungsberichte aus dem Institut für Höchsthfrequenztechnik und Elektronik Universität Karlsruhe*. Institut für Höchsthfrequenztechnik und Elektronik Universität Karlsruhe, June 2001.
- [58] S. C. Hagness, A. T. Taflove, and J. E. Bridges, "Two-dimensional FDTD analysis of a pulsed microwave confocal system for breast cancer detection: Design of an antenna-array element," *IEEE Trans. Ant. Propag.*, vol. 47, pp. 783–791, May 1999.
- [59] E. C. Fear and M. A. Stuchly, "Microwave breast cancer detection," *IEEE MTT-S Symposium Dig.*, June 2000. Boston.
- [60] E. C. Fear, J. Sill, and M. A. Stuchly, "Experimental feasibility of breast tumor detection and localization," *IEEE MTT-S Digest*, pp. 383–386, 2003.
- [61] T. J. Akai, *Applied Numerical Methods for Engineers*. Wiley, 1994.
- [62] D. Poole, *Linear Algebra*. Brooks/Cole, 2003.
- [63] C. R. Vogel, *Computational Methods for Inverse Problems*. SIAM, 2002.
- [64] J. E. Dennis and R. B. Schnabel, *Numerical Methods for Unconstrained Optimization and Nonlinear Equations*. Society for Industrial and Applied Mathematics, 1996.
- [65] C. T. Kelley, *Iterative Methods for Optimization*. Society for Industrial and Applied Mathematics, 1999.
- [66] P. M. Pardalos and J. B. Rosen, *Constrained Global Optimization: Algorithms and Applications*. Springer, 1987.

- [67] The Math Works Inc., “Matlab optimization toolbox reference,” 2001.
- [68] R. Mittra, S. Chakravarty, and J. Yeo, “Application of micro-genetic algorithm (MGA) to a class of electromagnetic analysis and synthesis problems,” *Proc. IEEE AP-S Symposium*, vol. 1, pp. 306–309, 2002.
- [69] CST GmbH, “CST Microwave Studio Version 4.1 Manual,” 2002.
- [70] C. G. Broyden, “A class of methods for solving nonlinear simultaneous equations,” *Math. Comp.*, vol. 19, pp. 577–593, 1965.
- [71] Hewlett Packard, “HP 85050C 7mm precision calibration kit operating and service manual,” 1996.
- [72] Cuming Microwave Corporation, “C-Stock AK datasheet.”
- [73] B. Schiek, *Grundlagen der Hochfrequenzmesstechnik*. Springer, 1999.
- [74] K. Kark, “Konvergenz und Wichtung von Orthogonalreihen bei Beugungsproblemen,” *Frequenz*, vol. 52, no. 1-2, pp. 14–20, 1998.
- [75] K. M. Hanson, “Method of evaluating image-recovery algorithms based on task performance,” *J. Opt. Soc. Am. A*, vol. 7, pp. 1294–1304, July 1990.
- [76] A. Jöstingmeier, T. Meyer, and A. S. Omar, “Material measurements of absorbers with magnetic losses,” *IEEE AP-S / URSI Symp. Digest*, June 2003.
- [77] K. S. Yee, “Numerical solution of initial boundary value problems involving maxwell’s equations in isotropic media,” *IEEE Trans. AP*, vol. 14, pp. 302–307, May 1966.
- [78] Y. Qian and T. Itoh, *FDTD Analysis and Design of Microwave Circuits and Antennas: Software and Applications*. Realyze Inc., 1999.
- [79] Cuming Microwave Corporation, “C-RAM FLX datasheet.”
- [80] A. R. von Hippel, *Dielectrics and Waves*. Artech House, 1995.
- [81] R. Schüler, *Entwicklung polymerer Verbundwerkstoffe mit elektrischer Leitfähigkeit*. Dissertation, TU Hamburg-Harburg, 1994.
- [82] M.-K. Schwarz, W. Bauhofer, and K. Schulte, “Alternating electric field induced agglomeration of carbon black filled resins,” *Polymer*, vol. 43, pp. 3079–3082, 2002.
- [83] J. C. Tippet and R. A. Speciale, “A rigorous technique for measuring the scattering matrix of a multiport device with a 2-port network analyzer,” *IEEE Trans. MTT*, vol. 30, pp. 661–666, May 1982.

- [84] H. Dropkin, "Comments on "a rigorous technique for measuring the scattering matrix of a multiport device with a 2-port network analyzer"," *IEEE Trans. MTT*, vol. 31, pp. 79–80, January 1983.
- [85] E. van Lil, "Comments on "a rigorous technique for measuring the scattering matrix of a multiport device with a 2-port network analyzer"," *IEEE Trans. MTT*, vol. 33, pp. 286–287, March 1985.
- [86] H.-J. Eul and B. Schiek, "A generalized theory and new calibration procedures for network analyzer self-calibration," *IEEE Trans. MTT*, vol. 39, pp. 724–731, April 1991.
- [87] D. F. Williams and D. K. Walker, "In-line multiport calibration algorithm," *51st ARFTG Conference Digest*, pp. 88–90, 1998.
- [88] T. Meyer, A. Jöstingmeier, N. G. Spiliotis, and A. Omar, "Multiport scattering parameter measuring system," *62nd ARFTG Microwave Measurements Conference Digest*, pp. 269–273, December 2003.
- [89] W. Ernst and J. J. Kotter, *ActiveX*. Markt & Technik, 1996.
- [90] D. Chappell, *ActiveX und OLE verstehen*. Microsoft Press, 1996.
- [91] T. Lingel, *Anwendung der Methode der Finiten Differenzen im Zeitbereich zur Optimierung passiver Wellenleiterdiskontinuitäten*. PhD thesis, TU Ilmenau, Verlag ISLE, 1999.
- [92] F. Löbner, "Entwicklung einer FDTD-Routine zur breitbandigen Berechnung der Streuparameter von in der Mikrowellen-Tomographie eingesetzten Resonatoren," Master's thesis, O.-v.-Guericke Universität Magdeburg, IESK, 2003.

Lebenslauf

Name: Tobias Meyer
Geburtsdatum: 6.10.1972
Geburtsort: Lauchhammer
Familienstand: verheiratet, 2 Kinder

Schulausbildung

9 / 79 bis 7 / 85 Polytechnische Oberschule W. Wander Magdeburg
9 / 85 bis 7 / 92 Sportgymnasium Magdeburg
Abschluß: Allgemeine Hochschulreife

Studium

9 / 92 bis 7 / 94 O.-v.-Guericke Universität Magdeburg
Studiengang Elektrotechnik
Abschluß: Vordiplom
9 / 94 bis 7 / 95 University of Wales
Studium Elektrotechnik, Betriebswirtschaft und Englisch
9 / 95 bis 2 / 99 O.-v.-Guericke Universität Magdeburg
Studienrichtung: Nachrichtentechnik
Abschluß: Dipl.- Ing. Elektrotechnik
Prädikat: mit Auszeichnung

Berufspraxis

3 / 99 bis jetzt Wissenschaftlicher Mitarbeiter
Lehrstuhl für Hochfrequenz- und Kommunikationstechnik
O.-v.-Guericke Universität Magdeburg